

MEASURING AND PREDICTING SEALANT ADHESION

by

Nick E. Shephard

Dissertation submitted to the Faculty of the

Virginia Polytechnic Institute and State University

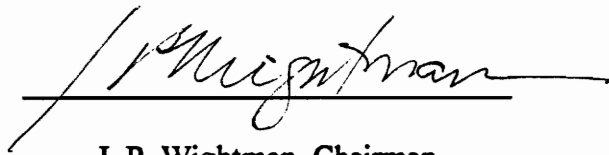
in partial fulfillment of the requirements for the degree of:

DOCTOR OF PHILOSOPHY

in

Materials Engineering Science

APPROVED:



J. P. Wightman, Chairman



D. A. Dillard



H. W. Gibson



T. C. Ward



G. L. Wilkes

April 1995

Blacksburg, Virginia

Key words: Silicone, Shift Factor, Humidity, Aluminum, Steel, Glass

C.2

LD
5655
V856
1995
S547
C.2

MEASURING AND PREDICTING SEALANT ADHESION

by

Nick E. Shephard

Committee Chairman: Dr. James P. Wightman

Materials Engineering Science

(ABSTRACT)

Current sealant test methods do not lend themselves well to the measurement and prediction of sealant performance. The objective of this work was to demonstrate that measurement of sealant material properties as a function of temperature and relative humidity for a specific sealant and substrate can be used to predict the long term performance of sealant joints independent of the joint geometry.

The material properties of a silicone sealant were characterized as a function of temperature, relative humidity and test rate. The fracture energy of the silicone sealant bonded to glass, aluminum or stainless steel was measured with the 180° peel, the 45° peel and the pure shear butt joint test methods. Scanning electron microscopy, electron spectroscopy for chemical analysis and atomic force microscopy were used to analyze the failure surfaces.

The failure mode for silicone sealant on aluminum changes from near the aluminum oxide layer to cohesive in the sealant when the relative humidity is less than 35%. The temperature shift factor was not related to the WLF theory but worked well

with an Arrhenius theory. The activation energy for the fracture process was 31.2 kcal/mol.

Crack growth data for an expansion joint was calculated for the weather conditions in Miami, Florida and Wittman, Arizona using the climate data obtained for the year 1994. For both climates, the nearly all the crack growth occurred during the winter months. The predicted annual crack growth data for Miami was 0.7 mm and the predicted annual crack growth for Wittman was 3.7 mm.

The fracture energy of the silicone/stainless steel joint is proportional to the amount of PDMS left on the surface. Carbonaceous contamination is not displaced by the sealant. Contamination inhibits primary bonding (ionic or covalent) and results in a lower fracture energy. Roughness increases the fracture energy; and this effect is more pronounced when the surfaces are cleaner. Water lowers the fracture energy especially for the dirtier surfaces. Roughness reduces the effect of the water damage but doesn't eliminate it.

To my family.....

Acknowledgments

I would like to express my gratitude to the following organizations and individuals without whom I could never have completed this research:

Dr. J.P. Wightman, chairman of my committee, for his support, encouragement, wit and guidance. It has been my great pleasure and good fortune to have him as my chairman and friend.

Dr. D. A. Dillard, Dr. H. W. Gibson, Dr. T. C. Ward and Dr. G. L. Wilkes for comprising the rest of my graduate committee. Their advice has been invaluable. I would like to especially thank Dr. Dillard for letting me use his lab and equipment as if it were my own.

Dr. Marc Mantel for his collaboration on the stainless steel study and for correcting my misguided priorities towards research and the enjoyment of life.

Dr. Y. I. Rabinovich for his expertise with the atomic force microscope.

Mr. Frank Cromer for his surface analysis training and expertise.

The Dow Corning Corporation and all my friends and colleges there for financial support, lab equipment and research expertise.

The Center for Adhesive and Sealant Science at Virginia Polytechnic Institute for research funding and many opportunities to present my research at professional meetings.

Ms. Katy Hatfield, Ms. Kim Linkous, Ms. Virginia Keller and Ms. Linda Haney for all their help in the Center for Adhesive and Sealant Science Office.

My research group colleagues, Dr. Mojee Babai-Cline, Dr. Joanie Chin, Ms. Holly Grammer, Dr. Francis Webster, Ms. Hong Zhuang and Mr. Shigeo Mori.

I would also like to thank the research groups of Dr. D. A. Dillard and Dr. T. C. Ward for their helpful advice and friendship. I especially want to thank Hari Parvatareddy for his loyal friendship, philosophical discussions and moral support.

Finally, I would like to thank Ms. Kiersten Urban for making my last year at VPI the best year of my life. I give all my love to you, Kiersten, for your thoughtfulness, support and laughter.

TABLE OF CONTENTS

	<u>Page</u>
I. Introduction	1
1.1 Description of Problem and Thesis Statement	1
1.2 References	3
II. Literature Review	4
2.1 Applications of Sealant Compounds	4
2.2 Silicone Sealant Chemistry and Properties	8
2.2.1 Chemistry of Polydimethylsiloxane	8
2.2.2 End-linking Reaction for Sealant Cure	11
2.2.3 Reinforcing Filler	11
2.3 Theories of Adhesion	13
2.3.1 Mechanical Interlocking	13
2.3.2 Diffusion Theory	14
2.3.3 Electronic Theory	14
2.3.4 Adsorption Theory	14
2.4 The Method of Reduced Variables	15
2.5 Fracture Theory	16
2.5.1 Fracture Energy for the Peel Test	18
2.5.2 Fracture Energy for the Butt Joint in Tension	20
2.6 Current Sealant Test Specifications and Recent Trends	22
2.6.1 ASTM, Military and Federal Test Specifications	22
2.6.1.1 Physical Properties of Cured Sealant	24
2.6.1.2 Adhesion	25
2.6.1.3 Durability	25
2.6.2 Resent Trends in Sealant Testing	27
2.7 References	29

III.	Experimental	34
3.1	Materials	34
3.1.1	Sealant Compounding	35
3.1.2	Substrates	37
3.1.2.1	Aluminum	37
3.1.2.2	Glass	37
3.1.2.3	Stainless Steel	37
3.2	Surface Preparation	38
3.2.1	Aluminum	38
3.2.2	Glass	40
3.2.3	Stainless Steel	40
3.3	Characterization of Sealant Properties	41
3.3.1	Sol and Gel Fraction	41
3.3.2	Modulus	43
3.3.2.1	Equilibrium Uniaxial Tension	43
3.3.2.2	Equilibrium Pure Shear Butt Joint	44
3.3.2.2	Strain Rate of 0.33 1/s	48
3.4	Characterization of Surface Properties	48
3.4.1	Scanning Electron Microscopy	48
3.4.2	Electron Spectroscopy for Chemical Analysis	
50		
3.4.3	Atomic Force Microscopy	54
3.5	Construction and Testing of Sealant Joints	54
3.5.1	180° Peel Configuration	54
3.5.2	45° Peel Configuration	57
3.5.3	Water Immersion, Temperature and Relative Humidity Control for the 45° Peel Test.	61
3.5.4	Pure Shear Tensile Butt Joint	64
3.6	References	67

IV.	Results and Discussion:	
	Effect of Peeling Thickness, Sealant Modulus and Peel Rate on 180° Peel Adhesion of Silicone Sealant to Glass and Aluminum	68
4.1	Sealant Characterization	68
4.1.1	Sol and Gel Fraction	69
4.1.2	Modulus	72
4.1.2.1	Equilibrium conditions	72
4.1.2.2	Test speed of 0.33 1/s	77
4.2	Peel Adhesion	83
4.2.1	Glass Substrate	86
4.2.2	Aluminum Substrate	91
4.2.3	Failure Mode Changes	92
4.3	Summary	96
4.4	References	97
V.	Results and Discussion:	
	45° Peel Adhesion of Silicone Sealant to Aluminum and Glass under Wet and Dry conditions	99
5.1	Sealant Characterization	100
5.2	Initial Surface Analysis by ESCA	100
5.3	Fracture Energy Measurement	102
5.3.1	Fracture Energy of Sealant on Glass	102
5.3.2	Fracture Energy of Sealant on Aluminum	104
5.4	Fracture Surface Analysis by ESCA	105
5.4.1	Analysis of Glass Fracture Surface	105
5.4.2	Analysis of Aluminum Fracture Surface	107
5.5	Model of Fracture Surface	109
5.6	Summary	111
5.7	References	112

VI.	Results and Discussion:	
	Effect of Surface Contamination and Roughness on	
	45° Peel Adhesion of Silicone Sealant to Stainless Steel	
	under Dry and Wet Conditions	113
6.1	Sealant Characterization	114
6.1.1.	Stainless Steel Surface	114
6.1.1.1	ESCA	114
6.1.1.2	AFM Images	114
6.1.2	Silicone Surface	119
6.1.2.1	ESCA	119
6.1.2.2	AFM Images	119
6.2	Adhesive Strength	122
6.3	Analysis of Fracture Surfaces	125
6.3.1	Stainless Steel Surface	128
6.3.1.1	ESCA Analysis	128
6.3.1.2	AFM Images	128
6.3.2	ESCA of Silicone Surface	131
6.3.3	Contamination	134
6.3.4	Roughness	136
6.3.5	Water immersion	138
6.4	Model of Failure Surface	138
6.5	Summary	143
6.6	References	143
VII.	Results and Discussion:	
	45° Peel Adhesion Doubly Shifted Master Curves for Silicone	
	Sealant Adhesion to Aluminum by varying Temperature and	
	Relative Humidity	145
7.1	Sealant Modulus in Uniaxial Tension	145
7.1.1	Equilibrium conditions	145
7.2	Aluminum Surface Analysis	149

7.2.1	Scanning Electron Microscopy	149
7.2.2	ESCA	149
7.3	Fracture Energy Measurement	149
7.4	Fracture Surface Analysis by SEM	153
7.5	Fracture Surface Analysis by ESCA	153
7.6	Master Curve Plot	153
7.7	Shift Factor Plot	157
7.8	Crack Growth Rate Equation	161
7.9	Summary	163
7.10	References	163
VIII.	Results and Discussion:	
	Application of Shifting Variables to the Silicone Sealant Butt Joint	164
8.1	Equilibrium Stress vs. Displacement	164
8.2	Fracture Energy vs. Crack Speed Measurement	168
8.3	Comparison to Peel Fracture Data	168
8.4	Summary	173
8.5	References	174
IX.	Results and Discussion:	
	Crack Growth Predictions based on Master Curves and Climate Data	175
9.1	Simulated Joint Conditions	175
9.2	Crack Growth Calculations	177
9.2.1	Miami, Florida, 1994	178
9.2.2	Wittman, Arizona, 1994	181

9.3	Summary	186
9.4	References	187
X.	Overall Summary	188
Vita		192

LIST OF FIGURES

Figure 2.1	Typical expansion joint design. Adapted from Ref. 4.	6
Figure 2.2	Typical structural glazing application. Adapted from Ref. 4.	7
Figure 2.3	The direct process for production of silicone polymer. Adapted from Refs. 13 and 14.	10
Figure 2.4	Outline of cure reaction for silicone sealants. Adapted from Ref. 18 and 19.	12
Figure 2.5	An example of the method of reduced variables. Adapted from Ref. 37.	17
Figure 2.6	Generalized fracture energy vs. crack speed on log-log scale. Adapted from Ref. 50.	19
Figure 2.7	Various configurations of the sealant butt joint. a.) thick adhesive layer, b.) thin adhesive layer, c.) thin adhesive layer with small depth. Adopted from Ref. 55 and 56.	21
Figure 2.8	Tensile adhesion test specimen used for ASTM C-719. Sealant dimensions are 12.7 mm x 12.7 mm x 50.8 mm.	26
Figure 3.1	Calibration curve for cathetometer.	45
Figure 3.2	Apparatus for measuring stress vs. strain at equilibrium conditions and constant temperature.	46
Figure 3.3	Pure shear butt joint sample geometry.	47
Figure 3.4	Side view of pure shear butt joint test frame and insulated box.	49
Figure 3.5	180° peel test sample geometry for a peeling width of 0.0127 m.	56
Figure 3.6	45° peel specimen geometry.	58
Figure 3.7	Creep frame and transducer for the 45° peel test.	59
Figure 3.8	Crack length vs. time for a representative 45° peel specimen.	60

Figure 3.9	45° peel specimen mounted in an insulated box.	62
Figure 3.10	Control system for maintaining constant temperature and relative humidity for temperatures above ambient.	63
Figure 3.11	Circuit for measuring relative humidity. Output is linear 0 to 20 mV.	65
Figure 3.12	Control system for maintaining constant temperature and relative humidity for temperatures below ambient.	66.
Figure 4.1	Volume fraction and gel fraction for sealants using hexane solvent.	71
Figure 4.2	Stress vs. strain for equilibrium condition.	73
Figure 4.3	Energy to break vs. gel fraction under equilibrium.	76
Figure 4.4	Stress vs. strain for Gaussian chain elastomer model at equilibrium.	78
Figure 4.5	Modulus vs. gel fraction under equilibrium conditions.	79
Figure 4.6	Stress vs. strain at 0.33 s^{-1} strain rate.	80
Figure 4.7	Energy to break for equilibrium and 0.33 s^{-1} strain rate vs. gel fraction.	82
Figure 4.8	Stress vs. strain for Gaussian chain elastomer model at strain rate of 0.33 s^{-1} .	84
Figure 4.9	Modulus for Gaussian chain elastomer model and Young's modulus vs. gel fraction under equilibrium conditions and for strain rate of 0.33 s^{-1} .	85
Figure 4.10	Log of fracture energy vs. log of strain rate for sealant adhesion to glass.	88
Figure 4.11	Correspondence of n with gel fraction for glass fracture data. 95% confidence limits are included.	90

Figure 4.12	Log of fracture energy vs. log of strain rate for sealant adhesion to aluminum. Circles indicate cohesive failure. Otherwise mixed mode or adhesive failure occurred.	93
Figure 4.12	Region of cohesive failure for glass and aluminum. Void areas represent adhesive failure.	95
Figure 5.1	Log of fracture energy vs. log of peel rate for sealant on glass and aluminum.	103
Figure 5.2	Model of peel failure occurring near the interphase in the sealant/aluminum specimen.	110
Figure 6.1	Organic contaminant layer thickness (nm) for different surface treatments.	116
Figure 6.2	AFM images for the water rinsed and argon plasma cleaned "Mirror Finish" samples.	118
Figure 6.3	AFM images for the "Bright Anneal" stainless steel sample after the water rinsing.	120
Figure 6.4	Fracture energy G (N/m) as a function of the peeling rate for all samples.	123
Figure 6.5	Fracture energy vs. crack rate after vertical shifting to determine relative vertical displacements.	126
Figure 6.6	a.) Relative G_0 vs. surface treatment and peeling condition. b.) Bulk data not included.	127
Figure 6.7	AFM images for the water rinsed and argon plasma cleaned "Mirror Finish" samples.	132
Figure 6.8	AFM images for the water rinsed and argon plasma cleaned "Bright Anneal" samples.	133
Figure 6.9	Relative vertical shift in threshold fracture energy as a function of carbonaceous layer contamination thickness.	135

Figure 6.10	Atomic percent Si removed after cleaning in hexane as a function of the carbonaceous contaminant layer.	137
Figure 6.11	Decrease in atomic percent silicon after debonding in water vs. air.	139
Figure 6.12	Fracture energy (N/m) as a function of the PDMS film thickness left on the surface after peeling.	140
Figure 6.13	Fracture energy (N/m) as a function of the PDMS film thickness left on the surface after peeling. Extrapolation to 100% cohesive failure.	142
Figure 7.1	Stress vs. strain under equilibrium conditions for sealant formulation 249-3.	146
Figure 7.2	Stress vs. complex strain function for sealant 249-3 using Gaussian elastomer model at equilibrium.	147
Figure 7.3	Scanning electron micrographs of polished and cleaned aluminum.	150
Figure 7.4	Logarithm of fracture energy vs. logarithm of crack speed.	152
Figure 7.5	SEM of aluminum fracture surface.	154
Figure 7.6	Master curve for 50°C and 49% relative humidity.	156
Figure 7.7	Shift factor plot for a_{th} .	159
Figure 7.8	Shift factor plot for a_T using an Arrhenius relationship.	160
Figure 7.9	Master curves for log of fracture energy vs. log of crack rate extended to cover 20 decades of crack rate.	162
Figure 8.1	Stress vs. displacement for 249-3 sealant cured at 27°C in butt joint configuration to glass substrates.	165
Figure 8.2	a.) Slope, m , vs. temperature for regression data of Fig. 8.1. b.) Intercept, b , vs. temperature data of Fig. 8.1.	167

Figure 8.3	Crack length vs. time for sealant 249-3 in an aluminum butt joint.	169
Figure 8.4	Log of strain energy release rate vs. log of crack speed for aluminum butt joint.	171
Figure 8.5	Comparison of fracture data for silicone/aluminum butt joint and silicone/aluminum 45° peel test.	172
Figure 9.1	a.) Joint movement for 12.7 mm joint with reference temperature 30° C. b.) strain energy release rate for the same joint with silicone sealant 249-3.	176
Figure 9.2	Daily high and low temperature for Miami Florida during 1994. Dashed horizontal line is sealant application temperature.	179
Figure 9.3	Daily high and low relative humidity for Miami Florida during 1994. Dashed horizontal line is point where failure mode changes from interphase to cohesive in sealant.	181
Figure 9.4	Daily crack growth in aluminum joint for Miami climate.	182
Figure 9.5	Daily high and low temperature for Wittman Arizona during 1994. Dashed horizontal line is sealant application temperature.	183
Figure 9.6	Daily high and low relative humidity for Wittman Arizona during 1994. Dashed horizontal line is point where failure mode changes from interphase to cohesive in sealant.	184
Figure 9.7	Daily crack growth in aluminum joint for two different climates.	185

LIST OF TABLES

Table 2.1	Common test specifications for sealant materials.	23
Table 3.1	Sealant formulations and reference numbers.	36
Table 3.2	Summary of the chemical composition (bulk), designation and structure of stainless steel.	39
Table 3.3	Summary of stainless steel type, surface and cleaning treatment.	42
Table 3.4	Atomic density and inelastic mean free path values used in ESCA analysis.	52
Table 4.1	Sealant swelling and gel data for hexane solvent.	70
Table 4.2	Stress vs. strain summary for equilibrium strain.	75
Table 4.3	Stress vs. strain summary for 0.33 1/s strain rate.	81
Table 4.4	Summary of adhesion test results for sealant on glass and aluminum.	87
Table 4.5	Regression data for glass adhesion.	89
Table 4.6	Regression data for aluminum adhesion.	94
Table 5.1	ESCA analysis of cured sealant, solvent cleaned aluminum and solvent cleaned glass.	101
Table 5.2	ESCA analysis of glass fracture surfaces.	106
Table 5.3	ESCA analysis of aluminum fracture surfaces.	108
Table 6.1	Surface composition of "Bright Anneal" and "Mirror Finish" stainless steel for different cleaning treatments.	115
Table 6.2	Atomic composition of cured sealant.	121
Table 6.3	Regression analysis for fracture energy curves in Fig. 6.4.	124

Table 6.4	Surface composition of the interface failure of the stainless steel substrate after peeling in air and the values of the PDMS layer thickness (D_{PDMS}).	129
Table 6.5	Surface composition of the interface failure of the stainless steel substrate after peeling in water and the values of the PDMS layer thickness (D_{PDMS}).	130
Table 7.1	Rubber properties obtained at equilibrium strain rate for sealant 249-3.	148
Table 7.2	ESCA results for polished and cleaned aluminum.	151
Table 7.3	ESCA results for aluminum fracture surface.	155
Table 7.4	Summary of shift factor data and linear equation coefficients.	158
Table 8.1	Summary of crack growth data for the pure shear butt joint tested at 49% relative humidity and 50°C.	170

I. Introduction

1.1 Description of Problem and Thesis Statement

There are two specific reasons for measuring adhesion. The first reason is to obtain a numerical value which can compare the difference in adhesion between one formulation, substrate or surface treatment and another. The second and more difficult application of adhesion data is towards the estimation of joint performance in the field.

It is commonly known that current test methods are not well suited for measuring intrinsic adhesive forces.¹ The material properties of a specific adhesive or sealant and interphase are difficult to isolate from the joint system as a whole. The forces and displacements measured usually change whenever the geometry, rate or environment change. Therefore, a particular adhesive and substrate system may perform better than another when tested in a peel test but perform worse when another test method, joint geometry, or test rate is employed. A good example of this problem can be seen in Figure 4.10. In this case, a low modulus sealant has a higher fracture energy than a high modulus sealant when tested at a high strain rate. When the same two sealants were tested at a low strain rate, the high modulus sealant had the higher fracture energy.

Therefore, it is necessary to quantify the material response of the joint system as a function of the state of stress, physical and chemical, and the rate of stress for the test method in question. Once this data is obtained, it can be used on any other test method or joint configuration so long as the state of stress and rate of stress are also defined.

The above difficulties are further complicated by the need to obtain long term information on the sealant durability often spanning many decades. It is impractical for all but the most theoretical, and well funded scientist, to conduct real time experiments. Therefore, researchers have established methods for accelerating the physical and chemical processes which control the speed of an experiment. For example, stress relaxation

experiments on an amorphous polymer conducted at high temperature over a period of hours can be used to describe the stress relaxation of the same polymer at ambient temperature, which would take years to occur in real time. This method of accelerating a test is known as time-temperature-superposition. The same method can be used for variables other than temperature. This more general method is known as “the method of shifting variables”. Additionally, more than one variable can be shifted at a time to obtain long term data as a function of several variables. For a silicone sealant joint, some common significant variables are rate, temperature and relative humidity. This leads to the following thesis statement:

Sealant material properties measured as a function of rate, temperature and relative humidity for a specific sealant and substrate can be used to predict the long term performance of sealant joints independent of the joint geometry so long as the same materials are used to construct the joint.

The purpose of this dissertation was to test the validity of the above thesis statement. Toward this goal, several studies were conducted in order to obtain material properties for silicone sealant and various substrates in three different joint geometries and as a function of temperature, test rate and relative humidity.

In Chapter IV, the 180° peel test was studied at different test speeds, peel thicknesses and sealant moduli on glass and aluminum.

In Chapter V, the 45° peel test was used to investigate the fracture energy of a high and a low modulus sealant, on glass or aluminum, under wet or dry conditions and over several decades of rate.

The study described in Chapter VI used the same test method and conditions of the study in Chapter V to investigate the effect of roughness and contamination on the fracture energy of silicone sealant to stainless steel.

In Chapter VII, the fracture energy of silicone sealant from polished aluminum was measured as a function of rate, temperature and relative humidity. In this same chapter, the method of shifting variables was used to prepare doubly shifted master curves and shift factor plots describing the dependence of the fracture energy on rate, temperature and relative humidity.

The fracture energy of the same sealant and aluminum used in the previous study was measured for the butt joint geometry and described in Chapter VIII. The resulting fracture energy data was compared to the 45° peel test data in Chapter V.

Finally, in Chapter IX, the daily crack growth over the course of one year for sealant bonded to aluminum in a butt joint was predicted for the two different climates of Wittman, Arizona and Miami, Florida.

1.2 References

¹ Adhesion and Adhesives, A. J. Kinloch, Ed., pg 57. Chapman and Hall, London (1987).

2 Literature Review

2.1 Applications of Sealant Compounds

Sealants are used extensively in nearly all fields of construction and materials design. Many books and journals are devoted to the subject.¹⁻⁷ Sealants are low modulus viscoelastic adhesives. Most sealant applications are in non-load bearing joints.

Sealants are used as a protective barrier to prevent the movement of gases, liquids and solids. Reduction of vibration, such as mechanical shocks, engine vibrations and sound, is commonly accomplished with sealants. Sealants are especially suited for protecting relatively large joints which undergo cyclic strains. Sealants are needed whenever large materials are joined. This is true because large bodies exhibit significant dimensional changes when their environment changes. Decreasing temperature decreases the size of the substrates causing an increase in the joint width. Therefore, the sealant experiences tensile forces during the winter months and compressive forces during the summer. A ten meter expanse of concrete will shorten or lengthen by as much as 4 mm due to annual changes in temperature. Therefore the most common use of sealant materials is in the commercial and home construction market. The focus of this dissertation is mainly on expansion joints for the construction market.

Building construction provides numerous opportunities for sealant use, starting with transverse and longitudinal expansion joints cut into the pavement and sidewalks leading up to the building. Expansion joints are the lowest load applications but

extremely high strain sealant applications. A typical expansion joint design can be found in Figure 2.1 Expansion joints can be horizontal, vertical, exposed or protected. The joints used for pavement and sidewalks are usually horizontal and exposed to pedestrian or vehicle traffic. Similar joints can be found running vertically between walls and on the exterior of large buildings. Such joints are usually not exposed to mechanical abrasion. The aforementioned joints are all examples of high movement joints which are not expected to carry significant loads. However, the sealant joint does contain significant stresses resulting from the changes in joint width which occur during thermal or weather related expansion and contraction of the substrates. The magnitude of the stress is directly related to the amount of strain and the modulus of the sealant as well as the joint design. Therefore, the modulus of the sealant is minimized to reduce the stress in the sealant and at the interphase of the sealant and the joint. In addition, the width of the joint is increased to reduce the amount of strain for a given movement. Furthermore, the width to depth ratio, commonly called the aspect ratio, is usually between two and four. The aspect ratio is optimized to maintain the correct stiffness in the joint without causing resulting in a excessively high stress intensity at the edge of the interphase between the sealant and the substrate.

Sealants used for structural glazing are often expected to carry a load. A typical structural glazing application is detailed in Figure 2.2. The sealant is used to seal out moisture and gases, dampen vibrations, and even support the weight of the window glass

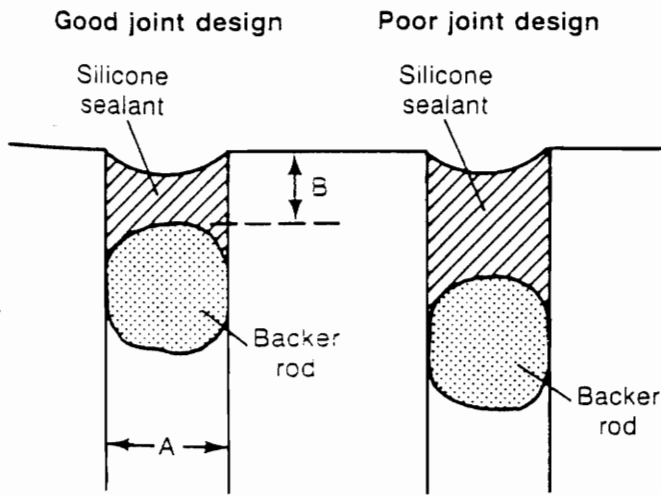


Figure 2.1 Typical expansion joint design. Adapted from Ref. 4.

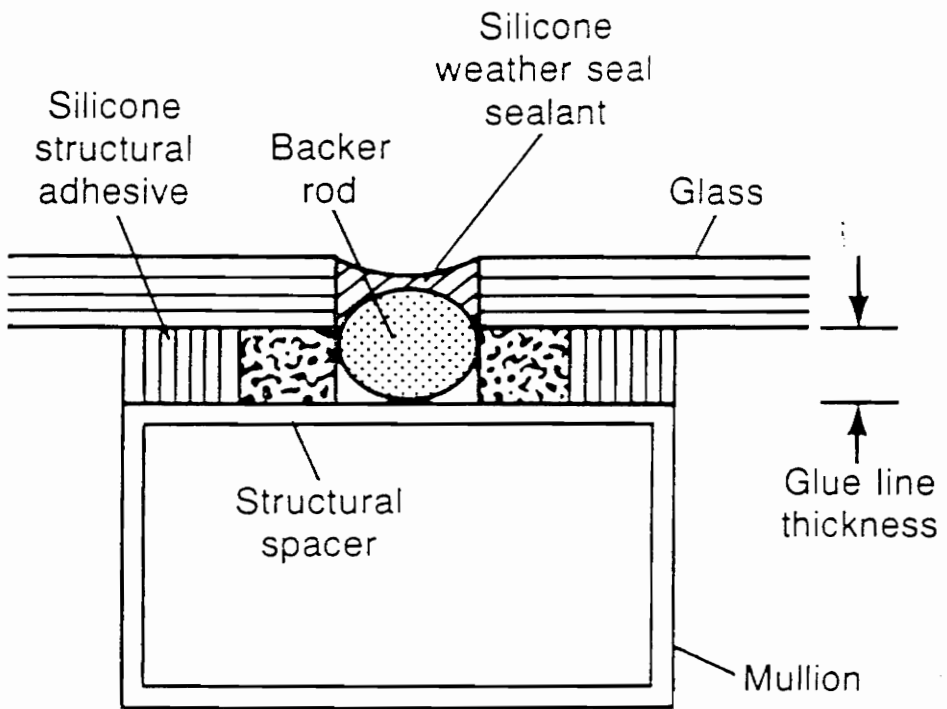


Figure 2.2 Typical structural glazing application. Adapted from Ref. 4.

in some cases. Therefore, the modulus of structural glazing sealant is higher than that of sealant used for expansion joints. Otherwise the glass may sag completely out of the sash. This results in high stresses in the sealant and at the bond line of the sealant and the sash. Therefore, structural glazing is a very severe sealant application.

2.2 Silicone Sealant Chemistry and Properties

As its name implies, silicone sealant is based on silicone polymer. It should not be confused with organic sealants which are “siliconized”. Such sealants are composed of a purely organic polymer with a few percent of silicone oil or silane adhesion promoter added. The many unique physical properties of silicone sealants can be related directly to the polydimethylsiloxane polymer of which all silicone sealants are comprised.

2.2.1 Chemistry of Polydimethylsiloxane

The development of polydimethylsiloxane (PDMS), commonly referred to as silicone, began with the isolation of silicon metal in the early 1800's. The first major work in organosilicon chemistry was conducted by Kipping and Robinson in 1900 through 1920.⁸ Kipping went on to define the knowledge base of organosilicon compounds through the use of Grignard reagents⁹ It was Kipping who coined the term silicone for the silicon analog of ketone.¹⁰ Today, the term silicone refers to the general class of chemicals which contain at least one silicon to oxygen bond and one silicon to carbon bond. The history of silicone chemistry has been reviewed by Weyenberg¹¹ and Liebhatzky.¹²

Silicone polymer is prepared by a direct process where silicon metal is converted to a chlorosilane by reaction with methyl chloride as described in Figure 2.3.¹³⁻¹⁵ This process is often referred to as the Rochow process after E.G. Rochow. Hydrolysis of the chlorosilane results in silicone oligomers and hydrochloric acid. The hydrochloric acid is then used to make more methyl chloride from methanol.

Silicone polymer has many unusual properties when compared to typical organic polymers. The flexibility and conformation of silicone has recently been reviewed by Grigoras and Lane.¹⁶ Silicone is a highly flexible polymer. The bond angle between Si-O-Si varies between 135 to 180° which is much wider than the carbon-carbon bond of most organic polymers. In addition the bond is unusually short at 0.1656 nm and has a low barrier of linearization at 0.3 kcal/mol. The Si-O-Si bond character is only partially explained by (*p-d*) π bonding because of the ionic character of the bond. The Si-O-Si bond is about 52% ionic by the Pauling scale. In contrast, the O-Si-O bond is fixed at 111° with a length of 0.1890 nm.

The flexibility of the silicone polymer is the key structural feature governing nearly all of its physical properties. It has a glass transition temperature of approximately -123 °C and a melting temperature of -50 °C. The free volume of silicone is 0.071.¹⁷ Therefore, the polymer is 10 to 20 times more permeable to gases, vapors, and hydrocarbons as compared to common organic polymers. The surface energy of silicone polymer is approximately 23 mN/m. This makes the polymer appear completely

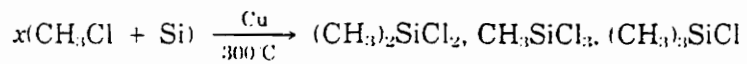
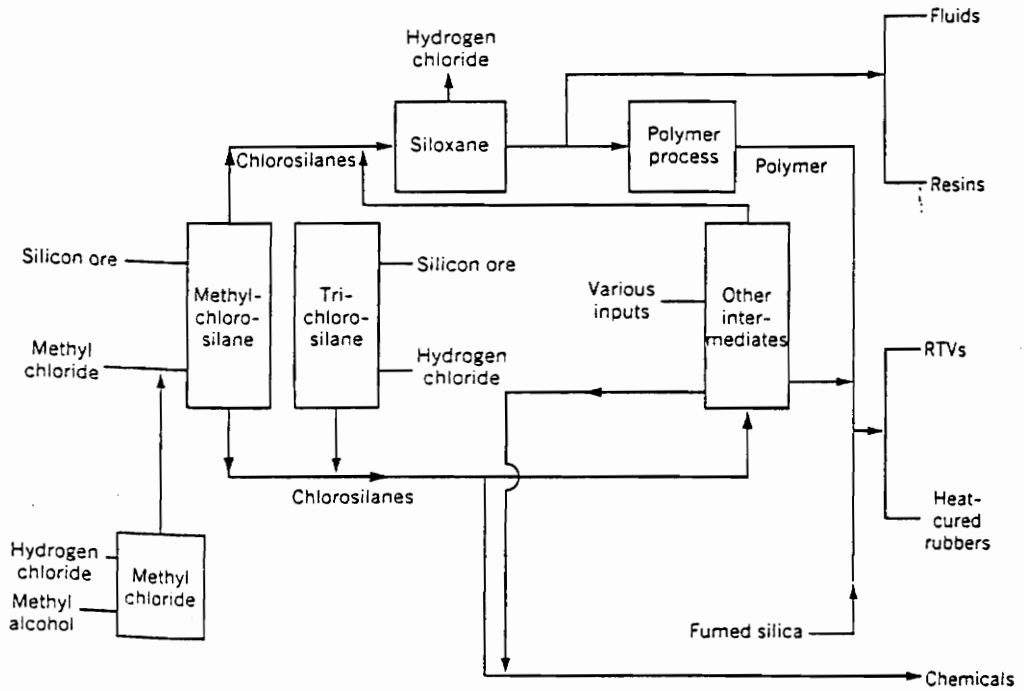


Figure 2.3 The direct process for production of silicone polymer. Adapted from Ref. 13 and 14.

hydrophobic to liquid water. Silicone polymer has excellent weathering characteristics. Oxygen and ultraviolet light do not degrade the polymer as fast as organic polymers are degraded. However, the ionic nature of the silicone polymer facilitates attack by acid or base.

2.2.2 End-linking Reaction for Sealant Cure

The three most common methods for forming a gel with PDMS are condensation, peroxide or addition cure mechanisms. The condensation method is most commonly employed with room temperature cure systems. In this instance, the gelation mainly proceeds at the reactive ends of the polymer. Therefore, it is often referred to as end-linking rather than cross-linking which is reserved for statistically random gelation. A general outline for the end-linking reaction used in this work is found in Figure 2.4.^{18,19}

For the sealant used in this study, the end-linker was methyltriacetoxysilane and the catalyst was dibutyltindilaurate. The rate of cure is governed by the concentration of catalyst, end-linker, water, acetic acid and silanol. The rate limiting step is the diffusion of moisture into the sealant and the diffusion of acetic acid out of the sealant. Under standard laboratory conditions, gelation proceeds from all exposed surfaces and propagates through the sealant at a rate of about 2 mm/day.

2.2.3 Reinforcing Filler

Silicone gels are notoriously weak and easily torn. The modulus and tear strength can be greatly increased by the addition of an appropriate filler. Fumed silica is the most

common filler used with silicone polymers.²⁰ The fumed silica imparts unique reinforcement and flow properties to the polymer. Thomas and Moore have demonstrated a forty fold increase in tensile strength.²¹ This is mainly the result of the highly structured nature (grape-like clusters of silica particles approximately 5 nm in diameter for each particle in the cluster) of fumed silica and its ability to hydrogen bond with the polymer and itself. The unusual structure of the fumed silica is the result of its method of production. This silica is prepared by the combustion of chlorosilanes in a hot flame. The resulting fume is collected and called fumed silica.

2.3 Theories of Adhesion

The scientific method attempts to provide theories which can explain events and observations. Theories are necessary to guide research in a logical progression towards understanding and controlling observations. Naturally, the development of adhesion as a science was accompanied by the evolution of several theories on the topic. Being a relatively new science, the theories of adhesion are constantly being reviewed, updated and improved.²²⁻²⁵ For the case of an individual joint, one or more of the theories of adhesion may be applicable. The various theories can be assimilated under the following four major theories of adhesion which are very briefly described below.

2.3.1 Mechanical Interlocking

Packham and Johnston have recently reviewed this theory.²⁶ The theory of mechanical interlocking suggests that good adhesion occurs when a liquid adhesive can

flow into pores on the surface of a solid substrate and solidify.²⁷ The result is a mechanical mechanism, similar to a dovetail joint, which prevents separation of the adhesive from the substrate. This theory is only applicable to rough or porous substrates and adhesives which are applied in the liquid state. Some common substrates to which this theory is applied are: wood, anodized aluminum, bone, masonry, and grit blasted surfaces.

2.3.2 Diffusion Theory

Diffusion theory is similar to mechanical interlocking only on the molecular level. This mechanism can only occur when the adhesive is significantly soluble in the substrate and the kinetics of diffusion allow enough flow before the adhesive solidifies.²⁸ Common applications of this theory are in solvent welded and spin welded plastic components.

2.3.3 Electronic Theory

Deryaguin has proposed that the transfer of electrons between the adhesive and the substrate can generate an attractive charge between the two.²⁹ This is one of the more controversial theories. Many researches are in disagreement over the magnitude of the forces involved in this mechanism.

2.3.4 Adsorption Theory

Adsorption theory includes physisorption and chemisorption. This theory is most often referred to when discussing sealant adhesion.³⁰ The low surface energy of the

silicone polymer promotes wetting and spreading on many substrates. This is the physisorption mechanism and only secondary bonding forces are involved. Often the thermodynamic work of adhesion as calculated by surface energy methods can be applied. Gutowski has modeled the adhesion of silicone sealants on several substrates using this theory.³¹ Reaction between silanols in the polymer and hydroxyl groups on the substrate are often proposed as the chemisorption mechanism. Plueddemann has pioneered the chemisorption theory as it applies to silane coupling agents.³²

2.4 The Method of Reduced Variables

Many books have been devoted to the subject of polymer viscoelasticity.³³⁻³⁶ Polymer viscoelasticity enjoys the highest level of theoretical development of the method of reduced variables, specifically, the variables of time and temperature. The more generalized method will be described for the variables of interest in this dissertation.

The method of reduced variables is used to accelerate the mechanism of a reaction or event in a predictable way so the results can be extrapolated over many years. This can be accomplished by increasing the stress (physical or chemical) or the temperature of the test to speed up the rate of the event in question. The method of accelerating the test involves finding variables which will accelerate the test without changing the mechanism of the process being measured. Some common variables are temperature, frequency, rate, humidity, filler level, pH, and polarity. Once the appropriate variables are obtained, the experimenter needs to conduct short duration tests over a range of the variables involved.

This will result in a series of curves which when plotted on a semi-log or a log-log scale against time or rate can be horizontally shifted to obtain a continuous curve spanning many decades of time. An example of such an experiment can be seen in Figure 2.5.³⁷ In this instance, the variable of interest was temperature and the dependent variable was tensile modulus. The inset is the shift factor plot. The shift factor, a_T , determines the amount of shifting along the horizontal axis necessary for a specific isotherm to match the master curve of a given reference temperature. The plot of $\log a_T$ vs. $\log T$ should be a smooth monotonic curve. An inflection in this curve would suggest a change in the mechanism of the process under observation.

More than one shifting variable can be used to develop the master curve.

However, it is necessary to assume that the variables in question are additive only and do not interact with each other. Sumita *et al.* used temperature and filler concentration to prepare a master curve of tensile yield stress for nylon.³⁸ Diamant and Folman used the same variables on polybutadiene.³⁹

2.5 Fracture Theory

Fracture mechanics can be described as the study of the growth of small flaws or cracks in a macroscopically homogeneous material. Again, many books have been written solely on the subject of fracture mechanics.⁴⁰⁻⁴³ The energy balance approach is most often applied to rubbery materials. Hamed has recently reviewed this approach for rubber vulcanizates.⁴⁴ The energy required to propagate a crack is divided into two

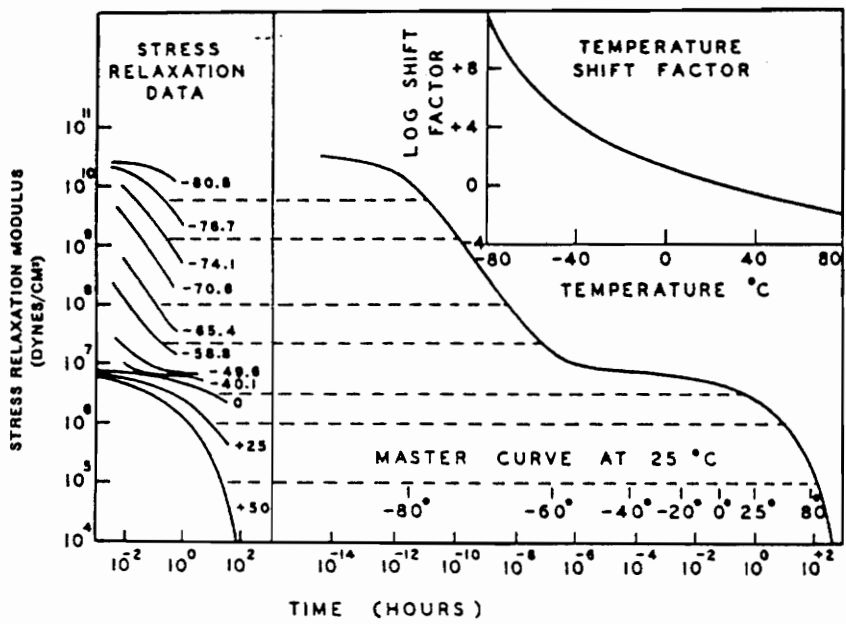


Figure 2.5. An example of the method of reduced variables. Adapted from Ref. 37.

parts, the intrinsic adhesive fracture energy, G_o , and the energy dissipated viscoelastically.

The energy needed to separate the two surfaces can be broken down as follows:⁴⁵

$$G = G_o \phi \quad (2.1)$$

$$\log G = \log G_o + \log \phi \quad (2.2)$$

where G is the strain energy release rate and ϕ is a dissipation function which is dependent on the temperature, the crack speed, and the average strain of the polymer. At constant temperature and strain, ϕ is a function of rate only. Equation 2.2 decouples the surface effects from the bulk effects. Changes measured as a function of surface changes will yield a series of curves which can be superimposed on each other by vertical shifting when plotted on a log-log graph of rate versus strain energy as seen in Figure 2.6. The amount of vertical shifting equals:

$$\Delta \log G = \log G_{o1} + \log \phi_1 - \log G_{o2} - \log \phi_2 \quad (2.3)$$

where ϕ_1 is assumed to be equal to ϕ_2 because the bulk material is the same for all the curves. The numerical subscripts on the right hand side of equation 2.3 represent different curves from the plot in Fig. 2.6. The above relationship has been useful for peeling conditions which do not include changes in the dissipation term.

2.5.1 Fracture Energy for the Peel Test

The fracture mechanics of the peel test have been extensively studied and recently reviewed.⁴⁶⁻⁵³ The fracture energy for the peel test is described by the following equation

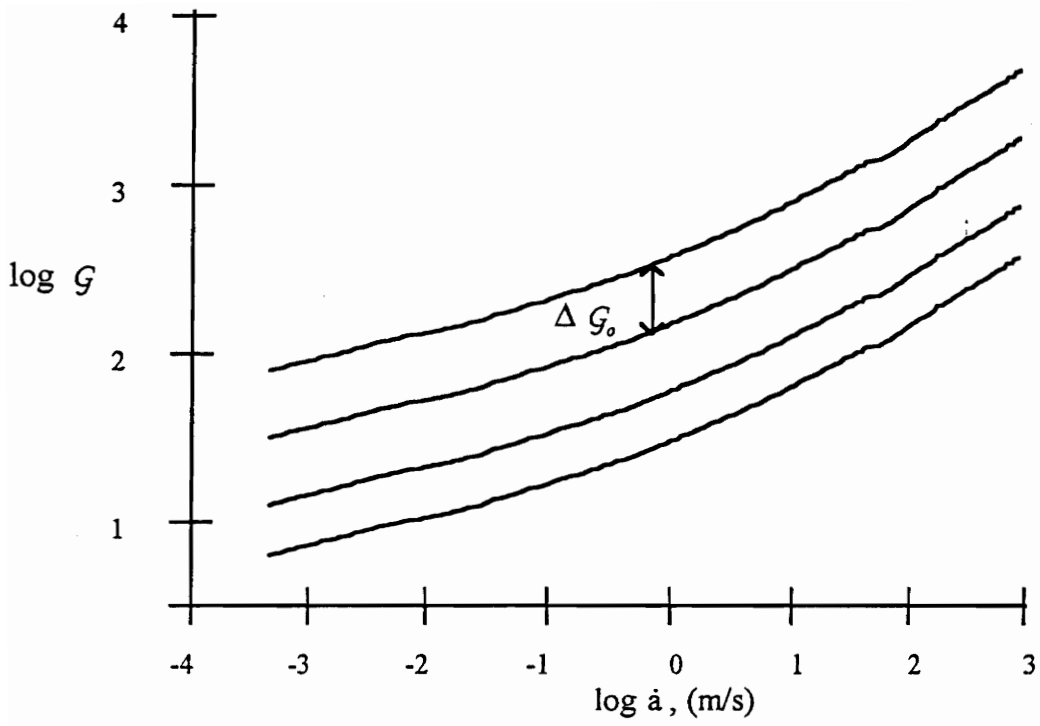


Figure 2.6. Generalized fracture energy vs. crack speed on log-log scale. Adapted from Ref. 50.

$$G = P/w(1-\cos \theta) \quad (2.4)$$

where P is the load, w is the peel width and θ is the peeling angle. Equation 2.4 assumes no strain occurs in the detached strip after peeling.

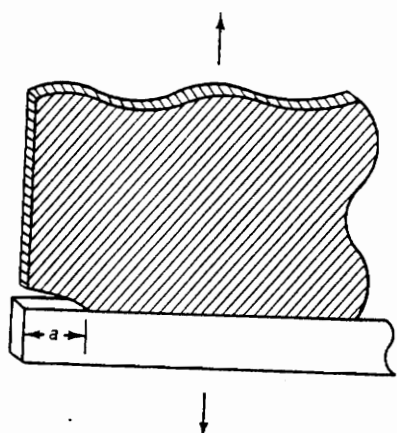
2.5.2 Fracture Energy for the Butt Joint in Tension

One of the more common sealant applications is the butt joint as described in Fig. 2.1. Gent has analyzed this joint geometry for cases of thin adhesive layers and for thick adhesive layers as depicted in Figure 2.7a and 2.7b.⁵⁴ For the case of the thin adhesive layer, the failure load was not a function of the crack length. However, the failure load was inversely proportional to the square root of the bond thickness. For a thick adhesive layer, the failure load was inversely proportional to the square root of the crack length and not related to the adhesive thickness.

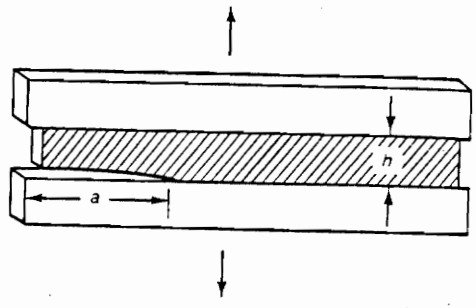
When the adhesive layer is thin and the width is small, 10 mm and 1 mm respectively, and the length is large, i.e. 100 mm, then the specimen is under a state of plain stress and the fracture energy is independent of the crack length as seen in Fig. 2.7c. The fracture energy for such a joint as just described, commonly called the pure shear test specimen, can be calculated from the following equation:⁵⁵

$$G = Wh_0 \quad (2.5)$$

where W is the strain energy density calculated as the area under the equilibrium stress strain plot and h_0 is the undeformed thickness of the sample.



a.)



b.) and c.)

Figure 2.7 Various configurations of the sealant butt joint. a.) thick adhesive layer, b.) thin adhesive layer, c.) thin adhesive layer with small depth. Adopted from Ref. 55 and 56.

2.6 Current Sealant Test Specifications and Recent Trends

Silicone sealant technology has rapidly progressed over the 50 years of its life. Unfortunately the test methodology has lagged behind. The technology for characterizing the sealant has been available for many years. However, the motivation to implement this technology is hindered by the desire to rapidly test and sell sealant. The various organizational bodies which define and implement new test standards are torn between improving technology and maintaining market position. A clear cut method for defining a good sealant from an average sealant is only valuable to the suppliers of good sealants. Therefore, the committees tend to settle for less definitive tests as outlined in section 2.6.1. In addition, manufacturers desire tests which are very fast in order to approve production lots in a timely fashion. It is left to the independent scientist, academia and product development stewards to facilitate the use of characterization methods which can define the performance of a sealant through measurement of material properties and sound application of fracture mechanics and engineering design. To this end, many recent and some older papers are discussed in section 2.6.2.

2.6.1 ASTM, Military and Federal Test Specifications

Table 2.1. contains a list of many of the various test specifications for determining the applicability of sealant formulations. The list of specifications are not inclusive. However, the major test methods are repeatedly outlined within each specification. The following is a brief description of the key points of the various test methods. Only the

Table 2.1. Common test specifications for sealant materials.

Application	Specification
construction-industrial	Federal Spec. TT-S-00227 two component
construction-industrial	Federal Spec. TT-S-00230 one component
architectural sealant	Federal Spec. TT-S-001543
general-purpose silicone	Military Spec. MIL-A-46106
silicone for electronics	
mechanical	Military Spec. MIL-A-46146
potting	Military Spec. MIL-I-81550
aerospace fuel tank sealant	Military Spec. MIL-S-8802
elastomeric joint sealants	ASTM C-920

tests which are conducted after curing the sealant will be discussed.

In all cases, the effect of strain rate is not addressed. In addition, only one or two different test temperatures are studied. Since the mechanical response of the sealant is both time and temperature dependent, it is imperative that tests be conducted to quantify this dependency. Otherwise, data taken at one temperature and rate can not be compared to tests conducted at any other temperature or rate.

Often, the testing and analysis are conducted using the assumptions of continuum mechanics. For example, the tensile adhesion test, ASTM C1135, and the cyclic strain version, ASTM C719, report either the stress to break the bond or the time for the bond to break. The butt joint is assumed to be homogeneous and no quantification of cracking or damage is conducted until after the specimen has completely failed. As described in section 2.5, fracture mechanics based test methods can provide more useful information regarding the mechanism and rate of crack growth in a particular joint.

2.6.1.1 Physical Properties of Cured Sealant

The key physical properties of the cured sealant are tensile strength, secant modulus at 100% elongation, elongation to break and hardness. The first three quantities are obtained from a stress vs. strain experiment conducted at a strain rate of 0.33/s and temperature of 25 °C. The stresses are calculated by dividing the force by the original sealant cross sectional area. The hardness of the cured sealant is measured using ASTM

C-661 Shore A durometer test method. The hardness is measured at 25 °C without a controlled rate of indentation.

2.6.1.2 Adhesion

ASTM C-794 adhesion in peel test method is the most frequently used adhesion test. It is a 180° peel test conducted at one rate of 8.4×10^{-4} m/s. The average peel force is divided by the width of the specimen (0.0254 m) and reported as the peel strength. The failure mode is noted by visual determination. Cohesive failure is easily determined when the crack propagates in the bulk of the sealant. When no trace of sealant is observable on the surface of the substrate, then the failure mode is considered adhesive.

ASTM C-1135 Determining Tensile Properties of Structural Sealants is a common test method for determining the adhesive strength of a joint in an actual joint configuration. The tensile adhesion test uses a butt joint geometry pulled in uniaxial tension at a rate of 6.7×10^{-2} s⁻¹. The joint dimensions are defined in Figure 2.8. The secant modulus is calculated at 10, 25, 50 and 100% elongation. The stress at break is also calculated. All stresses are calculated by dividing the force by the original area of the sealant. The mode of failure is noted using the same method as in ASTM C-794.

2.6.1.3 Durability

Tests methods ASTM C-794 and C-1135 are conducted after 1 day and 7 days of water immersion to evaluate the durability of the sealant bond. Immediately after removal

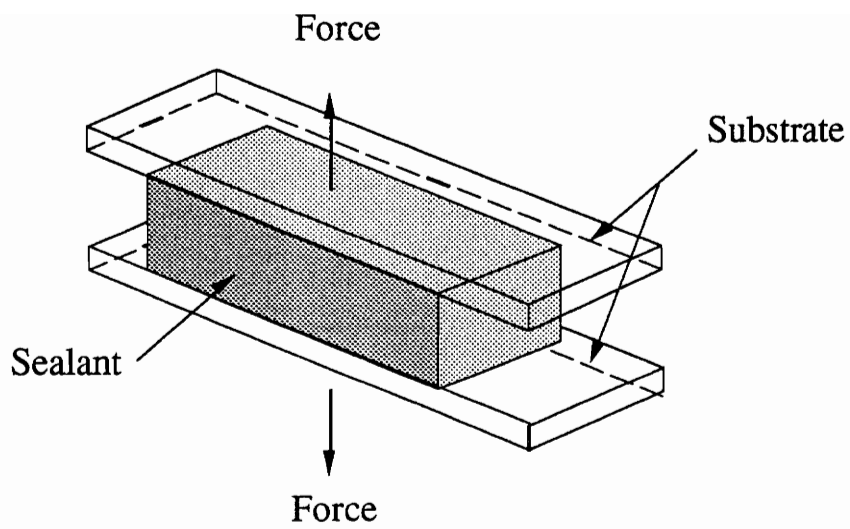


Figure 2.8 Tensile adhesion test specimen used for ASTM C-719. Sealant dimensions are 12.7 mm x 12.7 mm x 50.8 mm.

from the water, the tests are conducted and analyzed as described in the above paragraphs.

By far, the most definitive and severe adhesion test is the ASTM C-719 cyclic strain test using the ASTM C-1135 test geometry. The butt joint is cycled at a specified strain amplitude such as ± 0.125 or ± 0.25 . Before cycling, the butt joint is compressed at 70 °C for seven days then subjected to 10 strain cycles at room temperature. This is followed by 16 hours of compression at 70 °C then 10 more strain cycles at -26 °C. The percent failure through the sealant cross section is determined visually. The failure mode is determined as described in ASTM C-1135.

2.6.2 Recent Trends in Sealant Testing

Many papers have recently been published which attempt to address the viscoelastic properties of the sealant. Tock *et al.* have measured the stress vs strain response for a high modulus and medium modulus silicone sealant at three different strain rates and three different temperatures. In the same paper, Tock *et al.* used the theory of ideal elasticity and a modified Maxwell element to interpret the results.⁵⁶ They found the ideal elastomer theory to work well for strains less than 0.3. The modulus of the sealant decreased when the temperature increased. This did not follow the theory of ideal elasticity. However, the researchers did not recognize the need to conduct measurements at equilibrium when using this theory to predict cross-link density and temperature effects. Several researchers have investigated the stress relaxation of

silicone sealant at different temperatures.^{57,58} Stein and Prutzman have measured the stress relaxation of a model tin catalyzed silicone sealant as a function of temperature and in the presence or absence of moisture vapor.⁵⁹ Evidence for catalyzed hydrolysis of the siloxane bond was indicated. An activation energy of 10.3 kcal/mole was determined for the hydrolysis reaction. The hydrolysis was not observable when the tin catalyst was absent or the cure time was very long. Catsiff *et al.* has modeled the mechanical response of sealant butt joints under cyclic strain using a finite element approach.⁶⁰⁻⁶² In this study, the stresses and deformation of the polymer were estimated after each cycle of strain with good correlation to experimental results.

The durability of sealant bonds have been studied by several different research groups. In all cases, the sealant butt joint was used to model the sealant in an actual expansion joint. Sandberg and Albers developed empirical reduction factors to modify cyclic strain to break data for the effects of water immersion, heat aging and ultraviolet light.⁶³ Karpati has constructed master curves and failure envelopes for strain to break using temperature as the shifting variable.⁶⁴ In the same work, the strain to break was related to the cycles to fail for a given strain. In a different work, Karpati describes a cyclic strain outdoor exposure rack for screening silicone sealants.⁶⁵

In general, the trend has been to move away from the 180° peel test. Tensile adhesion testing under cyclic strain is the emerging method of choice. In nearly all the literature, the continuum mechanics approach is used to interpret the results. Only Gent

has attempted to use fracture mechanics to determine the relationship between tensile and shear stresses vs crack length for a sealant butt joint.⁶⁶ Numerous applications of fracture mechanics to rubber formulations have been documented as previously discussed in section 2.5. Yet, few experimenters have attempted to use fracture mechanics methods to analyze crack growth rate for a sealant formulation. Instead, durability is quantified as the time or number of cycles for a certain percentage of specimens to break catastrophically.

2.7 References

- ¹ Building Seals and Sealant; Fire Standards; Building Constructions, Annual Book of ASTM Standards, ASTM, Philadelphia, Pennsylvania.
- ² *Construction and Structural Adhesives and Sealants-An Industrial Guide*, E. W. Flick, Ed., Noyes Publications (1988).
- ³ *Adhesives, Sealants, and Coatings for the Electronics Industry*, E. W. Flick, Ed., Noyes Publications (1986).
- ⁴ *Engineered Materials Handbook, vol 3*. H.F. Brinson Ed., ASM International (1990).
- ⁵ Adhesives, Sealants and Primers, D.A.T.A. Digest, 5 ed. International Plastics Selector (1989).
- ⁶ J. M. Klosowski, *Sealants in Construction*, Marcel Dekker, Inc., New York (1989).
- ⁷ J. R. Panek and J. P. Cook, *Construction Sealants and Adhesives*, Wiley, New York (1984).
- ⁸ R. Robison and F. S. Kipping, *Journal of the Chemical Society*, **93**, 439 (1908).
- ⁹ F. S. Kipping, *Journal of the Chemical Society*, **91**, 209 (1907).

- ¹⁰ F. S. Kipping, *Journal of the Chemical Society*, **79**, 449 (1901).
- ¹¹ D. Weyenberg, "Silicones: Past, Present, and Future" Presented at International Organosilicon Symposium, St. Louis, MO, June 1987.
- ¹² S. Liebhatsky, *Silicones Under the Monogram*, Wiley, New York (1978).
- ¹³ C. A. Burkhard, E. G. Rochow, H. S. Booth, and J. Hartt, *Chemistry Reviews*, **41**, 97 (1947).
- ¹⁴ E. G. Rochow and W. F. Gilliam, *Journal of the American Chemical Society*, **67**, 963 (1945).
- ¹⁵ H. C. Brown, Ethyl Corp U.S. Pat. 2,762,824.
- ¹⁶ S. Grigoras and T. Lane, "Conformational Analysis of Substituted Polysiloxane Polymers," *Silicone-Based Polymer Science: a comprehensive resource*, J. Zeigler and G. Fearon Ed. American Chemical Society, Washington 1990.
- ¹⁷ J. D. Ferry, *Viscoelastic Properties of Polymers*, Wiley, NY (1980).
- ¹⁸ L. F. Ceyzeriat and P. Domant, Rhône-Poulenc, German Application 1121329.
- ¹⁹ L. B. Bruner, Dow Corning U.S. Patent 3035016.
- ²⁰ H. Cochrane and C. S. Lin, *Rubber Chemistry and Technology*, **66**(1), 48 (1993).
- ²¹ D. K. Thomas and B. B. Moore, *Polymer*, **13**(3), 109 (1972).
- ²² K. W. Allen, *Journal of Adhesion*, **21**, 261 (1987).
- ²³ D. H. Kaelble, *Physical Chemistry of Adhesion*, John Wiley and Sons, Inc., New York, 1971.
- ²⁴ W. C. Wake, *Polymer*, **19**, 291 (1978).
- ²⁵ A. J. Kinloch, *Adhesion and Adhesives*, Ch 3, Chapman and Hall, New York (1987).

- ²⁶ D. E. Packham and C. Johnston, *International Journal of Adhesion and Adhesives*, April, pp 131 (1994)
- ²⁷ J. W. McBain and D. G. Hopkins, *Journal of Physical Chemistry*, **29**, 188 (1925)
- ²⁸ S. S. Voyutskii, *Autohesion and Adhesion of High Polymers*, Wiley-Interscience, New York, 1963.
- ²⁹ B. V. Deryaguin, *Research*, **8**, 70 (1955).
- ³⁰ E.P. Plueddaman, *Journal of Paint Technology*, **42**(550), 600 (1970).
- ³¹ W. S. Gutowski, *Journal of Adhesion*, **22**, 183 (1987).
- ³² E. P. Plueddemann, *Silane Coupling Agents*, Plenum, New York (1982).
- ³³ A. V. Tobolsky, *Properties and Structure of Polymers*, John Wiley (1960).
- ³⁴ L. E. Nielson, *Mechanical Properties of Polymers*, Reinhold (1962).
- ³⁵ J. D. Ferry, *Viscoelastic Properties of Polymers*, 2nd ed., John Wiley (1970).
- ³⁶ J. J. Aklonis and W. J. MacKnight, *Introduction to Polymer Viscoelasticity*, 2nd ed., John Wiley (1983).
- ³⁷ E. Castiff and A. V. Tobolsky, *Journal of Polymer Science*, **19**, 111 (1956).
- ³⁸ M. Sumita, T. Shizuma, K. Miyasaka and K. Ishikawa, *Journal of Macromolecular Science, Physics*. **B22**(4), 601 (1983).
- ³⁹ Y. Diamant and M. Folman, *Polymer*, **20**, 1025 (1979).
- ⁴⁰ E. H. Andrews, *Fracture in Polymers*, American Elsevier, New York (1968).
- ⁴¹ H. H. Kausch, *Polymer Fracture*, 2nd ed., Springer-Verlag, Berlin, (1987).

- ⁴² A. J. Kinloch and R. J. Young, *Fracture Behavior of Polymers*, Applied Science, New York (1983).
- ⁴³ L. G. Williams, *Fracture Mechanics of Polymers*, Horwood, Chichester, England (1984).
- ⁴⁴ G. R. Hamed, *Rubber Chemistry and Technology*, **64**(3), 493 (1991).
- ⁴⁵ E. H. Andrews and A. J. Kinloch, *Proceedings of the Royal Society (London)*, Vol. A332, 1973, pp 401.
- ⁴⁶ D. H. Kaelble, *Journal of Colloid Science*, **19**, 1964, pp 413
- ⁴⁷ A. N. Gent and A. J. Kinloch, *Journal of Polymer Science, A-2*, **9**, 1971, pp 659.
- ⁴⁸ A. N. Gent and J. Schultz, *Journal of Adhesion*, Vol. 3, 1972, pp 281.
- ⁴⁹ A. N. Gent and G. R. Hamed, *Rubber Chemistry and Technology*, Vol. 51, 1978, pp 354.
- ⁵⁰ D. Maugis, *Journal of Adhesion*, Vol. 1, No. 2, 1987, pp 105.
- ⁵¹ T. Igarshi, "Peel-Strength and Energy Dissipation," *Adhesive Joints: Formation, Characteristics and Testing*, ed. K. L. Mittal, Plenum Press, New York, 1984, pp 419.
- ⁵² J. R. Huntsberger, "Interpreting Peel Tests," *Treatise on Adhesion and Adhesives*, ed. R. L. Patrick, Vol. 6, Marcel Dekker, New York, 1989, pp 1.
- ⁵³ G. R. Hamed, "Energy Conservation During Peel Testing," *Treatise on Adhesion and Adhesives*, ed. R. L. Patrick, Vol. 6, Marcel Dekker, New York, 1989, pp 33.
- ⁵⁴ A. N. Gent, *Rubber Chemistry and Technology*, **47**(1), 202 (1974).
- ⁵⁵ R. S. Rivlin and A. G. Thomas, *Journal of Polymer Science*, **10**, 291 (1953).

- ⁵⁶ R. W. Tock, M. V. R. N. Dinivahi and C. H. Chew, *Advances in Polymer Technology*, **8**(3), 317 (1988).
- ⁵⁷ D. W. Clegg, S. W. Addy, A. A. Collyer, I. K. Jones and S. Webb, *Polymer Communications*, **25**(3), 73 (1984).
- ⁵⁸ H. S. -Y. Hsich, L. C. Yanyo and R. J. Ambrose, *Journal of Applied Polymer Science*, **29**, 2331 (1984).
- ⁵⁹ J. Stein and L. C. Prutzman, *Journal of Applied Polymer Science*, **36**, 511 (1988).
- ⁶⁰ E. H. Catsiff, R. F. Hoffman, and R. T. Kowalewski, *Journal of Applied Polymer Science*, **14**, 1143 (1970).
- ⁶¹ E. H. Catsiff, R. F. Hoffman, and R. T. Kowalewski, *Journal of Applied Polymer Science*, **14**, 1159 (1970).
- ⁶² E. H. Catsiff, *Journal of Applied Polymer Science*, **15**, 1021 (1971).
- ⁶³ L. B. Sandberg and M. P. Albers, *Journal of Adhesion*, **15**, 27 (1982).
- ⁶⁴ K. K. Karpati, "Development of Test Procedure for Predicting Performance of Sealants", *Plastics mortars, sealants and caulking compounds*, R.B. Seymour Ed., American Chemical Society symposium series; 113, (1979).
- ⁶⁵ K. K. Karpati, *Journal of Coatings Technology*, **56**(710), 29 (1984).
- ⁶⁶ A. N. Gent, *Rubber Chemistry and Technology*, **47**(1), 202 (1974).

III. Experimental

3.1 Materials

To reduce the experimental error, all the materials used in this study were obtained or prepared from the same lots of material.

3.1.1 Sealant Compounding

Sealant formulations were compounded by the author to insure purity of the sealant and allow complete disclosure of the chemical composition. No pigments, fungicides or coupling agents were added to the formulation. The sealant compounding was performed in building DC4 at the Dow Corning Corporation facilities in Midland, Michigan.

Clear silicone sealant was used in this body of work. The sealant type is commonly known as "acetoxysilane" or "RTV-1" which is an acronym for "Room Temperature Vulcanization One-part". The acetoxysilane cure system was chosen for its good shelf stability and world wide recognition. The catalyst used was dibutyltin dilaurate, which was produced by Witco Corporation in N.Y. under the name FOMREZ UL-28[®] in 95% purity. The methyltriacetoxysilane end-linker was obtained from the Dow Corning Corporation in 89% purity.

The primary ingredient was polydimethylsiloxane- α,ω -diol, supplied by Dow Corning Corporation, with 42,000 g/mol number average molecular weight and with a viscosity of 14,000 centistoke. Methyl-terminated PDMS, supplied by Dow Corning

Corporation under the name 200 fluid[®] 14,800 g/mol number average molecular weight and 1000 cs viscosity, was added to adjust the modulus of the sealant. The polydispersity of both polymers is approximately 2.2. The methyl-terminated polymer does not end-link during the cure reaction. Instead, it acts like a diluent or plasticizer to reduce the end-link density. The ratio of end-linker reactive sites to reactive polymer ends was held constant at 16.5:1. Excess end-linker was used to react with excess water to reduce the cure rate and improve the shelf life of the uncured sealant.¹

Fumed silica, trade name L-90[®] obtained from Cabot Corporation, Akron OH, was added to the sealant to control the rheology and increase the modulus of the sealant.² The fumed silica was approximately 94% pure with a nitrogen BET surface area of 90 m²/g. The impurity is mostly adsorbed water. The sealant was prepared on a 3.7 L double planetary mixer manufactured by H. Ross and Sons, Inc., Wilmington, DE. The order of addition of the ingredients was as listed in Table 3.1. All mixing was performed under nitrogen. After mixing for twenty minutes, the sealant was degassed for 5 minutes under 800 mbar vacuum with mixing. The sealant was packaged into 178 ml polyethylene cartridges, obtained from Semco Incorporated, Chicago, IL. The cartridges were centrifuged for 20 minutes to remove any air entrapped during packaging. The yield was approximately 10 cartridges.

Table 3.1. Sealant formulations and reference numbers.

Sealant Designation	42,000 Mn HO(Si ₂ (CH ₃)O) _n H	1,000 Mn CH ₃ (Si ₂ (CH ₃)O)Si ₃ CH ₃	End-linker*	Fumed silica
45-1	100.0	0.0	6.0	6.0
45-2	83.3	16.7	5.0	6.0
45-3	66.6	33.4	4.0	6.0
45-4	50.0	50.0	3.0	6.0
249-3	100.0	0.0	6.0	12.2

*End-linker contains 8.26 wt% dibutyltindilaurate.

3.1.2. Substrates

3.1.2.1 Aluminum

The aluminum was 2.54 cm x 0.3175 cm extruded bar stock obtained from Heavener Hardware (Blacksburg VA). The alloy and heat treatment designation was 6061 T6. , i.e., no intentional oxide film formation technique was used in the manufacture of the aluminum.

3.1.2.2 Glass

Single strength float glass was obtained from Heavener Hardware and cut in the lab. The thickness of the glass was 1.27 mm. During the manufacture of the glass, the molten glass is cast onto the surface of molten tin. Some tin diffuses into the glass during this step. This results in one side of the glass containing some tin. The tin containing side of the glass was used for adhesion measurements. The tin containing side was chosen because the tin can be used as a tag element for the determination of the location of the glass surface during ESCA analysis. The tin containing side of the glass can be determined by observing the glass under ultraviolet light where the tin side will appear brighter than the no tin side of the glass. This was confirmed by ESCA analysis of both sides of the glass.

3.1.2.3 Stainless Steel

Two types of stainless steel, obtained from Ugine Savoie in France, were used for adhesion testing.³ The chemical composition, designation and structure of the stainless

steel is given in Table 3.2. Stainless steel foils have a 1 mm thickness after cold rolling and annealing at 1000 °C in a nitrogen-hydrogen atmosphere composed of 1/4 diatomic nitrogen and 3/4 diatomic hydrogen gas mixture. During the annealing process, a thin passive film forms with a surface roughness of 0.02 μm. After the annealing treatment, termed "Bright Anneal", the samples were protected with a pressure sensitive tape. The other surface treatment performed on the samples is termed "Mirror Finish" and consisted in polishing the surface in order to decrease the surface roughness.

3.2 Surface Preparation

Each substrate underwent surface treatments of various types as outlined in the sections below.

3.2.1 Aluminum

For the studies contained in Chapters IV and V, the aluminum was cleaned with detergent in deionized water followed by solvent cleaning in chloroethane then rinsed with acetone.

The aluminum used for the studies described in Chapters VI and VII was first polished with Brown Tripoli alumina polishing paste manufactured by Prairie Tool Company, Inc., Prairie du Chien, WI. The polishing technique consisted of a cotton cloth wheel which was driven by a grinder motor located in room 005 of Hahn hall. Each piece of aluminum was cut and then polished to a uniform smoothness. After polishing, tiny scratches running parallel to the spinning direction of the cloth wheel were observed

Table 3.2. Summary of the chemical composition (bulk), designation and structure of stainless steel.

Designation	Structure		Atomic concentration (%)						
			Fe	Cr	Ni	Mn	Si	Mo	C
AISI 304 (18/8)	Austenite	wt%	72	17.4	8.42	1.37	0.49	0.17	0.06
		at%	71	18.5	7.90	1.37	0.96	0.10	0.23

on the surface of the aluminum. After polishing, the aluminum was cleaned in chlorethane, then detergent and finally rinsed with deionized water. The polished aluminum was subjected to an argon plasma for 5 minutes at 50 watts. The plasma treatment was conducted in a March solid state Plasmod[®] radio frequency (13.56 MHz) generated glow discharge plasma unit made by March Instruments Inc., Concord, CA. Prior to plasma treatment, the chamber containing the samples was evacuated with a mechanical pump to $\sim 10^{-2}$ torr. The chamber was then filled with argon at a flow rate of ~ 1 liter/min and a pressure of 1 torr.

3.2.2 Glass

The glass used for the studies conducted in chapters IV and V was cleaned using the same method as described in the first part of section 3.2.1 above. The glass was cleaned with detergent in deionized water followed by solvent cleaning in chlorethane then rinsed with acetone.

3.2.3 Stainless Steel

Two surface treatments were used for the stainless steel; one representing a relatively clean surface and one representing a dirtier surface. Mantel *et al.*, have shown that the “as received” stainless steel surfaces contain organic contamination and significant levels of potassium.⁴ It was shown in the same work that potassium contamination on the stainless steel is not removed by plasma treatment, but is easily removed by deionized water. However, deionized water does not remove the organic

contamination. Therefore, the two surface treatments used for this study were a deionized water rinse and a deionized water rinse followed by argon plasma treatment. The deionized water rinse resulted in the dirtier surface containing organic contamination. And, the deionized water rinse plus argon plasma treatment resulted in a relatively clean surface. Hereafter, the water rinse treatment will be designated “water rinse” ;and, the water rinse plus argon plasma treatment will be designated “plasma treated”.

The surface treatments and cleaning procedures are described in Table 3.3. The argon plasma treatments were carried out in the March Plasmod[®] unit using the same conditions as for the aluminum substrate previously discussed in section 3.2.1. After any surface treatment, the samples were transferred within 15 minutes through the air to the ESCA or AFM instruments or bonded with the silicone sealant.

3.3 Characterization of Sealant Properties

3.3.1 Sol and Gel Fraction

The soluble fraction and insoluble fraction (gel) of the polymer network in hexane was measured using an analytical balance. The hexane used for this study was Fisher Scientific HPLC grade 99.97% pure. After curing the sealant for 43 days at ambient conditions, three 0.3 gram samples were cut from the cured sealant and weighed to the nearest 0.0001 gram. The initial weight of the sealant was designated W_0 . Each sample was placed in a 250 ml glass jar containing 100 ml of hexane. All three replicates were

Table 3.3. Summary of stainless steel type, surface and cleaning treatment.

Description	Surface treatment	Description	Cleaning treatment
304 B. A.	Bright Anneal: annealing at 1000 ^o in N ₂ + 3 H ₂	water	After peeling the protective PVC film and rinsing the sample for 1 minute in distilled water.
304 M. F.	Mirror Finish: annealing at 1000 ^o in N ₂ + 3 H ₂ and polishing	Ar Plasma	After peeling the protective PVC film, rinsing for 1 minute in distilled water and cleaning the surface with Argon plasma (50W 5min).

placed in the same jar. Each day for 5 days, the hexane was decanted from each sample jar and replaced with fresh hexane. After the fifth day, the sealant samples were weighed by removing them from the jar and patting them dry with a paper towel and placing them in a covered weigh dish. The swollen weight was designated W_s . The swollen polymer samples were then allowed to air dry for three days and then weighed again. The dry weight was designated W_g . One sample of the dry polymer, W_g , was placed in fresh hexane again for 48 hours and dried to constant weight to make certain the soluble fraction had been completely removed.

3.3.2 Modulus

The sealant modulus is a time dependent property. It was measured by three different methods and two different calculations. Measurements conducted at equilibrium were used to characterize the elastic response of the silicone polymer network. Measurements taken at rates faster than equilibrium include the viscous response of the silicone polymer network as well as the viscous response of the methyl ended polymer.

3.3.2.1 Equilibrium Uniaxial Tension

The modulus under quasi-equilibrium conditions was obtained by applying a dead load to the end of a hanging dog bone and measuring the elongation of the sealant after 1 hour. The dog bone was cut from a sheet of cured sealant using an ASTM D-638-5 carbon steel die. The sheet of sealant was prepared by tooling sealant onto a

polypropylene film using a shims to control the sealant thickness. After curing, the sealant sheet was easily removed from the polypropylene film. The thickness of the starting sheet of sealant was 1.27 mm. A mark was placed on the sealant by applying carbon black to the dog bone using a thin template to make a mark 1 mm wide running across the neck of the dog bone specimen. The strain was measured using a custom made cathetometer. The cathetometer measured from 0 to 800 units and had a focal length of approximately 7.5 cm. The units were calibrated against a micrometer and the results plotted in Figure 3.1. One meter equals 170090 units. The cathetometer was also used to measure the cross sectional area of the sealant within the gauge length. Constant temperature was maintained by suspending the dog bones inside an insulated box and blowing heated air through the box as depicted in Figure 3.2. The box was made from 2.54 cm thick styrofoam and the air was heated though a copper coil wound around a resistance heater. The temperature was controlled by a Variac and a CN9000A temperature controller and K type thermocouple from Omega Engineering Inc., Stanford, CT. Lead sinkers were used to supply the load to the dog bone and were attached to the dog-bone with alligator clips, 4.5 kg monofilament line and swivel hooks.

3.3.2.2 Equilibrium Pure Shear Butt Joint

The stress vs displacement under quasi-equilibrium conditions was measured using a stress relaxation experiment. The sample geometry can be seen in Figure 3.3 An

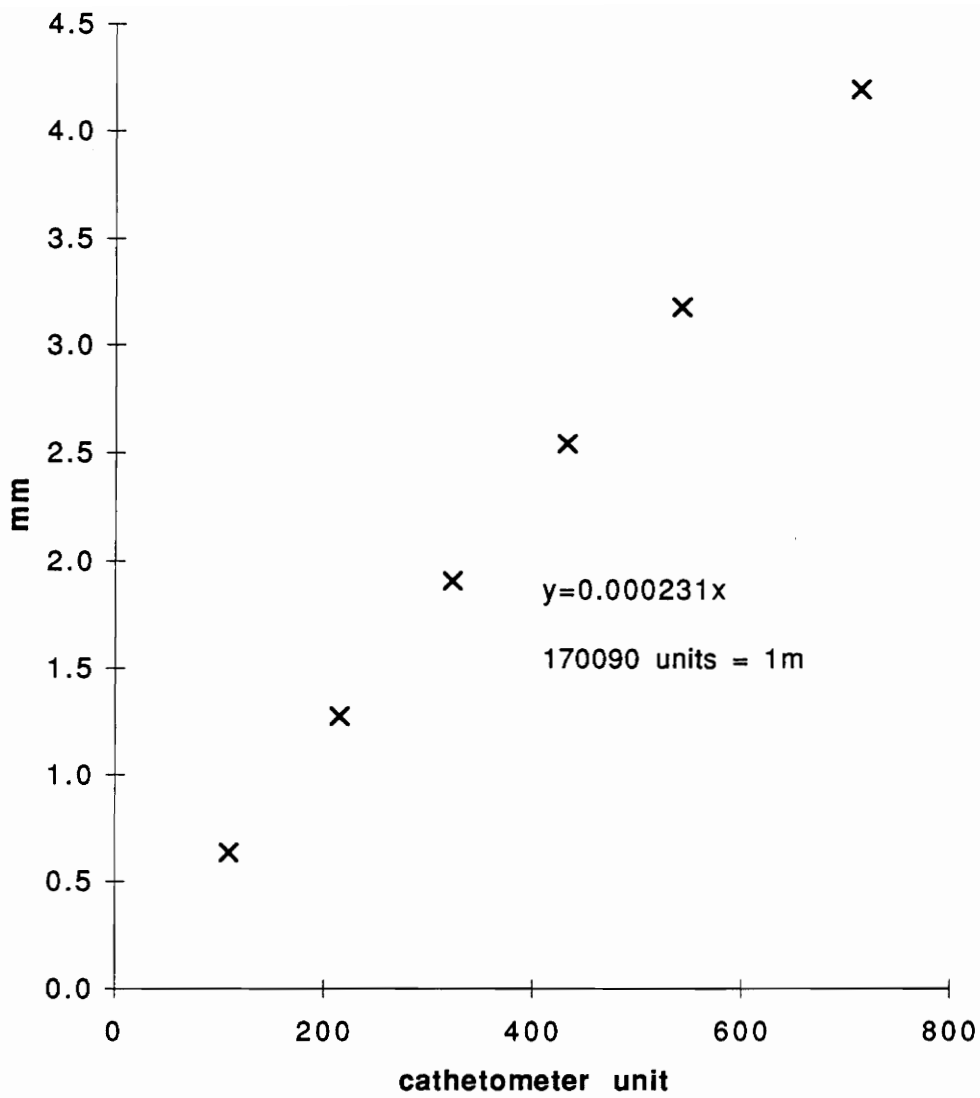


Figure 3.1. Calibration curve for cathetometer.

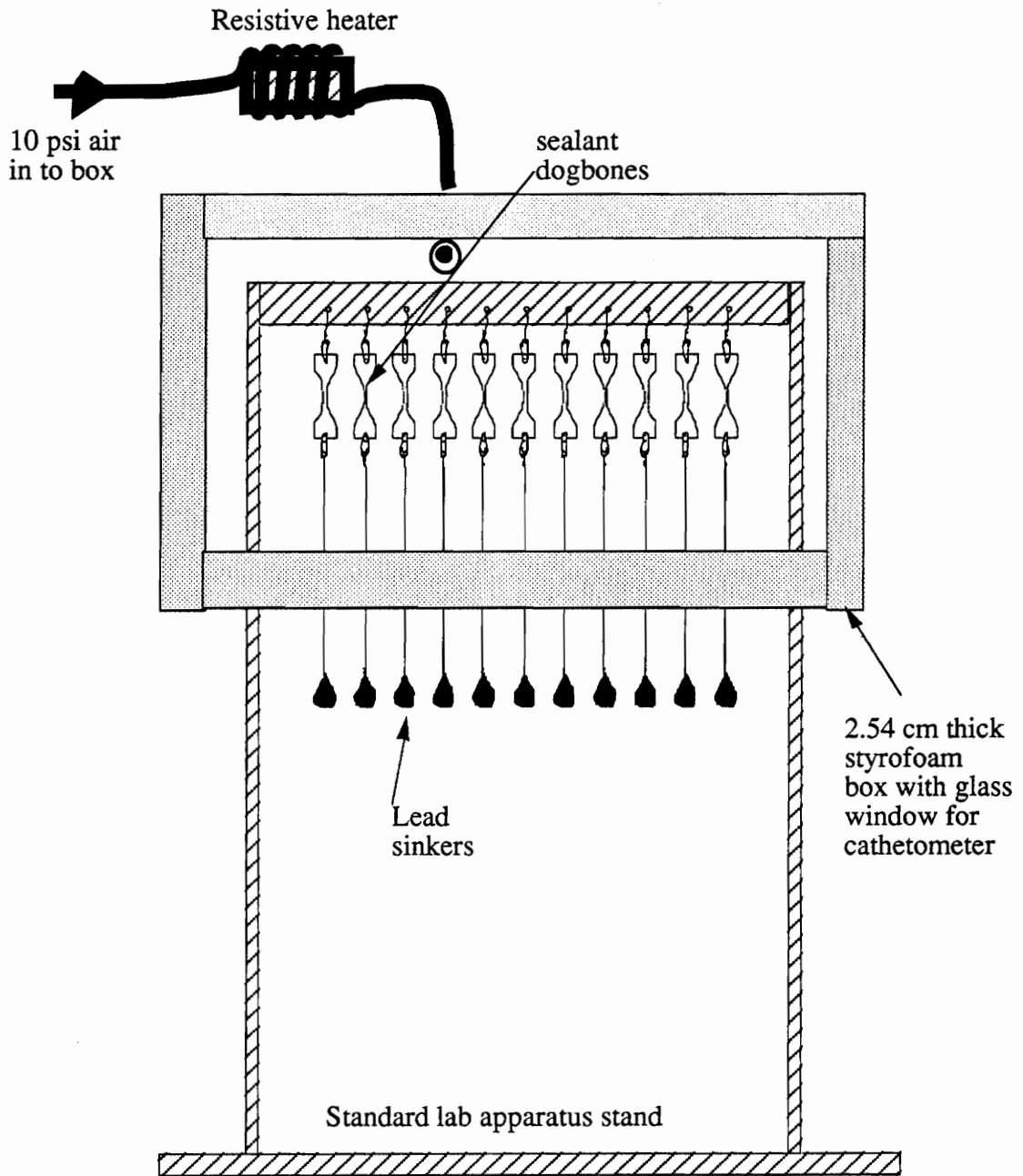


Figure 3.2. Apparatus for measuring stress vs strain at equilibrium conditions and constant temperature.

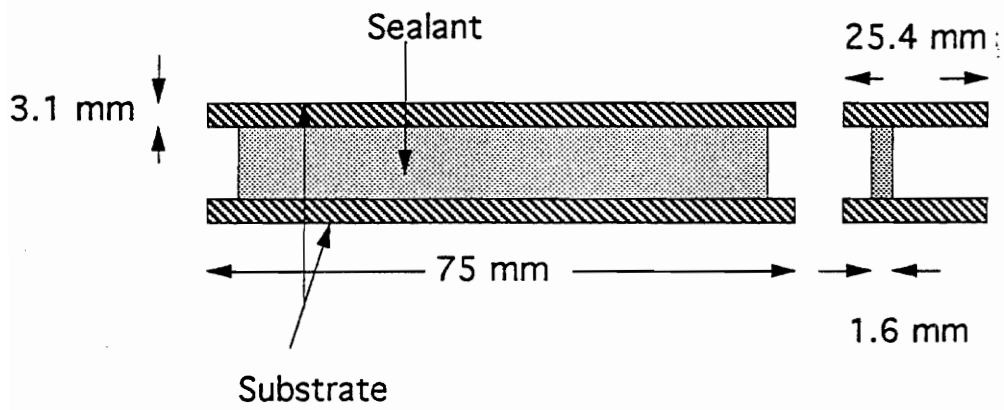


Figure 3.3 Pure shear butt joint sample geometry.

insulated steel box with a glass window was constructed identical to the styrofoam box in Figure 3.2. Temperature and relative humidity control was obtained by the method described in section 3.5.3. As depicted in Figure 3.4, the test specimen was suspended inside the box and held at a constant displacement by adjustment of a turn buckle at the top of the box. The turn buckle connected one side of the specimen to a load cell through a lever and fulcrum. The lever and fulcrum were used to insure that the resulting load was within the range of the load cell. The load on the specimen was continuously monitored by the load cell and output to a chart recorder. When the load reached equilibrium, taking approximately 1 hour, the displacement and load were recorded.

3.3.2.3 Strain Rate of 0.33 s^{-1}

The modulus of the sealant was measured using an Instron testing machine Model No. 1123 with a 500 g load cell and computer control software supplied by Instron. The tests were conducted at the Dow Corning Corporation facility in Midland, Michigan. Dog bone shaped test specimens were cut from sheets of sealant using an ASTM D-638-5 carbon steel die. A strain gauge was used to measure the change in length of the 25.4 mm gauge length. The cross head speed was 8.5 mm/s, which results in a strain rate of 0.33/s.

3.4 Characterization of Surface Properties

3.4.1 Scanning Electron Microscopy

Photomicrographs of the fracture surfaces and clean surfaces at 10000 times

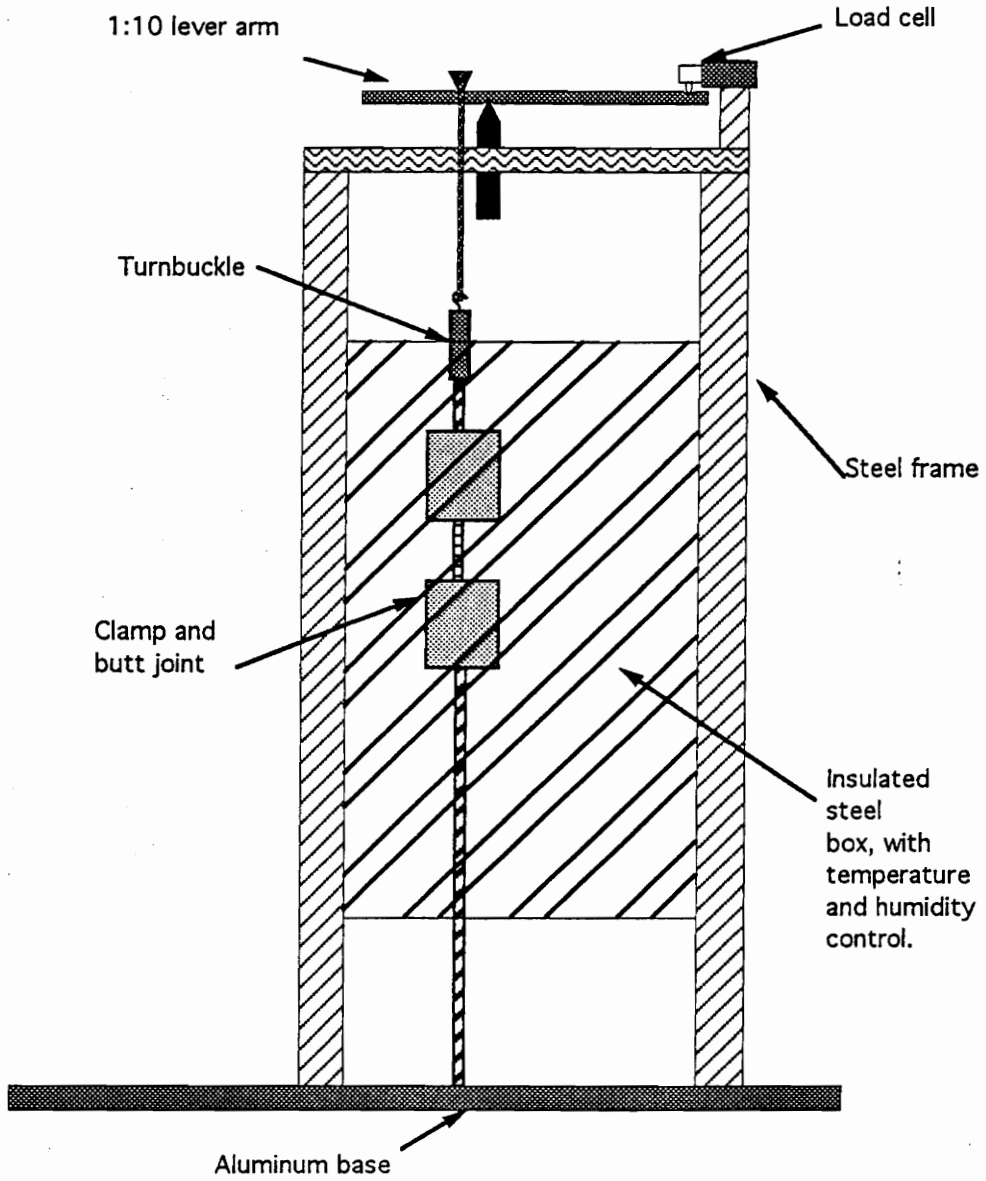


Figure 3.4 Side view of pure shear butt joint test frame and insulated box.

magnification were obtained with an ISI-SX-40 scanning electron microscope (SEM). The SEM was operated at an acceleration voltage of 20 kV. The samples were secured to brass mounts using double stick tape. The samples were made more conductive by sputtering gold with an Edwards Sputter Coater S150B. After sputtering the gold onto the samples, silver paint was used to insure electrical contact between the surface of the sample and the brass mounting fixture.

3.4.2 Electron Spectroscopy for Chemical Analysis

ESCA analysis was performed using a Perkin Elmer PHI 5400 spectrometer employing a Mg K α (1253.6 eV) achromatic X ray source operated at 15 kV with a power of 400 W. Typical operating pressures were $\sim 2 \times 10^{-8}$ torr and the area analyzed was a 1x3 mm rectangle. The spectrometer was calibrated to the 4f_{7/2} photopeak of gold at 83.8 eV and all binding energies were referenced to the carbon C 1s photopeak at 285.0 eV from adventitious carbon. The full width at half-maximum obtained for the Ag 3d_{5/2} line is 0.9 eV. Survey (wide) scan spectra were obtained with a pass energy of 44.75 eV for all samples to determine what elements were present in the top 5 nm of the surface. Multiplex (narrow) scan spectra were obtained with a pass energy of 17.9 eV for all major photopeaks to determine the binding energy and atomic concentration.

The line shapes used for curve fitting analyses were pure Gaussian for C 1s and O 1s photopeaks and were asymmetric Gaussian/Lorentzian for the Cr 2p and Fe 2p photopeaks. All the lines were computer generated. The atomic sensitivity factors used

for quantitative determination were obtained from the Physical Electronics (Perkin-Elmer) software. The background in the peak area computations was assumed to be linear. The error in the measurements of atomic concentrations can be estimated to be +/- 10%.

The oxide thickness on a metal surface can be calculated from the relative intensity of the metal and the oxide ESCA peaks and assuming a uniform overlayer by using the following equations:⁵

$$\frac{I_m}{I_o} = \frac{N_m \lambda_m}{N_o \lambda_o} \cdot \frac{\exp[-(d/\lambda_o \sin \theta)]}{1 - \exp[-(d/\lambda_o \sin \theta)]} \quad (3.1)$$

$$d = \lambda_o \sin \theta \ln \left(\frac{N_m \lambda_m}{N_o \lambda_o} \cdot \frac{I_o}{I_m} + 1 \right) \quad (3.2)$$

where I_m and I_o are the intensities of the metal and the oxide photoelectron peaks respectively; N_m and N_o are the atomic densities of metal and oxide; λ_m and λ_o are the inelastic mean free paths of the appropriate photoelectrons; and, the take off angle, θ , is 45°. The values of atomic densities and inelastic mean free paths for the metal and oxide can be found in Table 3.4.

A deviation to the exponential attenuation law is noted for take-off angles less than 30°. This can possibly be due to the non-uniform nature of the organic contamination layer. Although this simple uniform overlayer model applied to convert

Table 3.4 Atomic density and inelastic mean free path values used in ESCA analysis.

Layer	Aluminum alloy	Aluminum oxide	Iron/chromium oxide	Organic	Silicone
N (g/cm ³)	2.7	3.9	5.2	1.2	1
λ (nm)	2.2	2.4	1.2	1.85	1.85

ESCA intensity ratios into a value for the overlayer thickness has been criticized, the comparison of the given results can be taken as reasonable.⁶

Equation 3.1 has been modified for use with organic contamination.⁴ When an organic contaminant layer is assumed to be a homogeneous and continuous film on top of the oxide layer, the thickness of this contaminant layer (d_c) can be estimated from the integrated spectral intensity of the C 1s photopeak as follows:

$$\frac{I_o}{I_c} = \frac{N_o \lambda_o}{N_c \lambda_c} \cdot \frac{\exp[-(d/\lambda_c \sin \theta)]}{1 - \exp[-(d/\lambda_c \sin \theta)]} \quad (3.3)$$

where I_o and I_c are the intensities of the oxide and carbon photoelectron peaks respectively; N_o and N_c are the atomic densities of oxide and carbon; λ_o and λ_c are the inelastic mean free paths of the O 1s and C 1s photoelectrons; and, the take off angle, θ , is 45°. Using values given in Table 3.4, equation 3.1 can be simplified as shown below.

$$d_c(\text{nm}) = 1.31 \cdot \ln(3.5 I_c / I_o + 1) \quad (3.4)$$

with

$$\frac{I_c}{I_o} = \frac{\%C}{1 - \%C} \quad (3.5)$$

where %C is the atomic concentration of carbon calculated from ESCA spectra of carbon.

The same procedure has been applied to convert ESCA intensity ratios of silicone, measured on the interface failure side of steel substrate, into a value for the PDMS thickness. Assuming that this PDMS layer has the same composition as the bulk then

I_{PDMS} is four times the Si 1p photoelectron intensity, I_{Si} , calculated from ESCA spectra.

Again using values given in Table 3.4, Equation 3.1 can be simplified as shown below.

$$d_{\text{PDMS}}(\text{nm}) = 1.31 \cdot \ln(3.4I_{\text{PDMS}}/I_o + 1) \quad (3.6)$$

with
$$\frac{I_{\text{PDMS}}}{I_o} = \frac{4I_{\text{Si}}}{1 - 4I_{\text{Si}}} \quad (3.7)$$

3.4.2 Atomic Force Microscopy

AFM can investigate conducting and non-conducting samples, as well as transparent and opaque samples because it uses a reflective optical technique to sense the position of the tip relative to the sample. The AFM has a very sharp pyramidal tip that protrudes from the underside of a small, flexible cantilever. With a soft cantilever that generates forces smaller than inter-atomic forces, the topography of the sample can be measured without displacing the atoms. The surface images were obtained from a Nanoscope III AFM (Digital Instruments Co.) with a silicon nitride tip.

3.5 Construction and Testing of Sealant Joints

Three different test configurations were prepared as described in the following paragraphs. The cure conditions for all the specimens was at least 21 days at ambient conditions.

3.5.1 180° Peel Configuration

A modified version of the ASTM C 794-80 adhesion in peel test was employed. The test specimens were prepared by tooling a specified thickness of sealant onto the surface of the cleaned adherends. The thickness was controlled by using draw down bars

of the correct thickness. Immediately after the sealant was applied, a fiberglass cloth was pressed unto the sealant. Before the cloth was applied, sealant was tooled into both sides of the cloth. Finally, a second layer of sealant was applied to the top of the cloth to give the final thickness of the specimen, t , which was kept constant at 6.4 mm as seen in Figure 3.5. The strained thickness, b , of the sealant was varied over three different thicknesses ranging from 0.5 to 6.4 mm. This controlled the thickness of the region in which failure could occur. The peel cloth used was 213 g/m^2 fiberglass cloth with a silane sizing agent. The peel width was 12.7 mm. and controlled by cutting the peel samples after fully cured using a razor and a straight edge. The sealant was allowed to cure for 21 days at ambient conditions before testing. The strain in the tearing member was negligible because the fiberglass cloth had a much higher modulus than the sealant. The strain energy release rate G can be approximated by equation 3.6

$$G = \frac{P}{w}(1 - \cos\theta) \quad (3.8)$$

where P is the peeling force, w is the peel width and θ is the peeling angle.

The samples were tested using an Instron testing machine Model No. 1123 with a variable range 90 kg load cell and computer control software supplied by Instron. The samples were clamped into the Instron with an aluminum fixture designed to prevent breaking the glass substrate. The fiberglass cloth was pulled away from the substrate at a peeling angle of 180° . The peeling rate was varied over the range, 0.085 to 8.5 mm/s. A pre-crack was made in the sealant by using a razor blade to cut through the sealant next

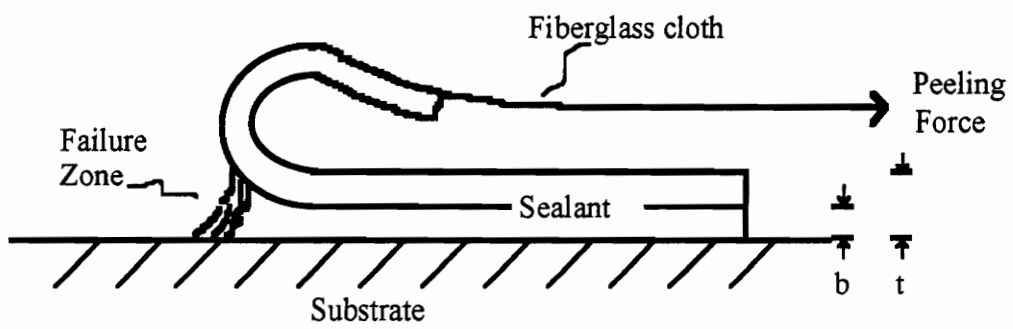


Figure 3.5. 180° peel test sample geometry for a peeling width of 0.0127 m.

to the substrate. Continuous data acquisition of the peeling force was achieved through the computer interface. The average peeling force at steady state peeling was used in all the data analysis. Visual inspection was used to determine the location of the crack growth.

3.5.2 45° Peel Configuration

The 45° peeling angle was chosen to minimize bending dissipation.⁷ The peel samples were prepared using the same techniques described in the previous section. However, the bond thickness was 1.27 mm and no additional sealant was tooled over the fiberglass cloth. Figure 3.6 describes the sample geometry. The peel sample was debonded under constant load while monitoring crack length using a creep frame and linearly variable displacement transducer as described in Figure 3.7. The load was controlled to the nearest gram. Crack length was measured to the nearest micrometer and monitored continuously by a chart recorder. The fracture energy was calculated by equation 3.8 with the variables defined in Figure 3.6. The crack growth rate was calculated from the steady state crack length vs. time data. An example of crack length vs. time data can be found in Figure 3.8. The range of crack speed recorded was 10^{-10} m/s to 10^{-3} m/s.

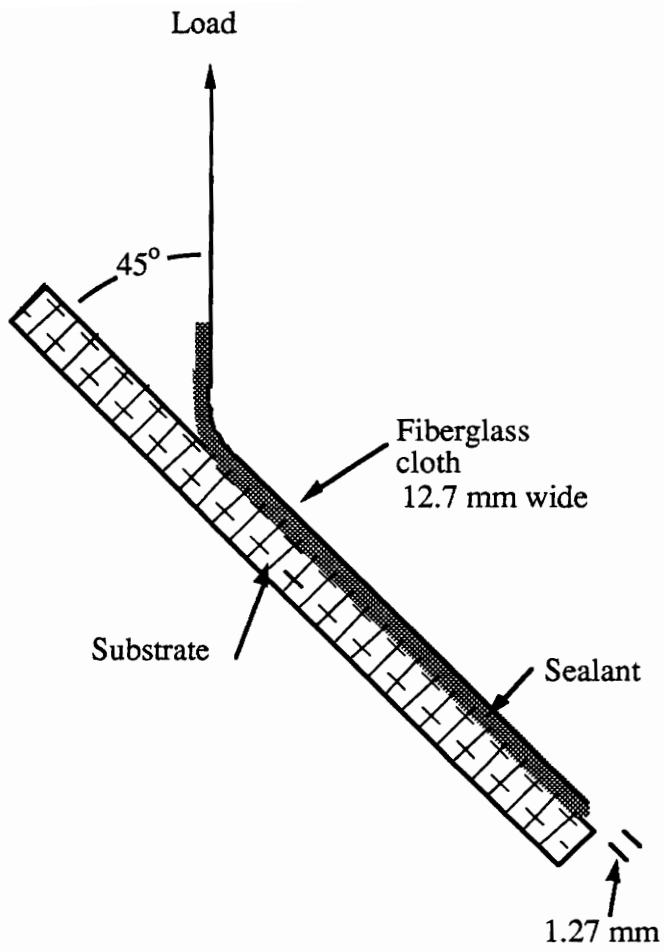


Figure 3.6. 45° peel specimen geometry.

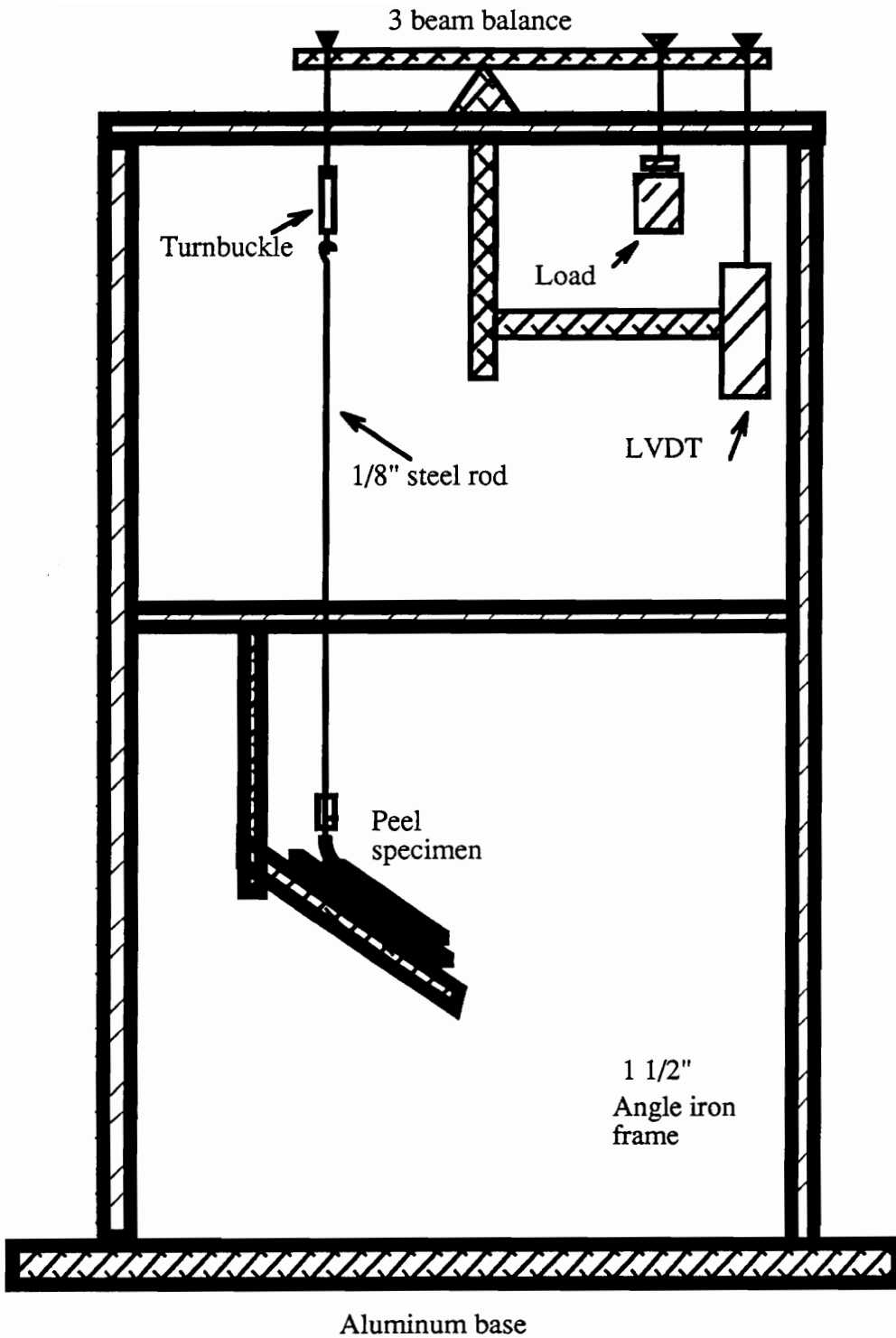


Figure 3.7. Creep frame and transducer for the 45° peel test.

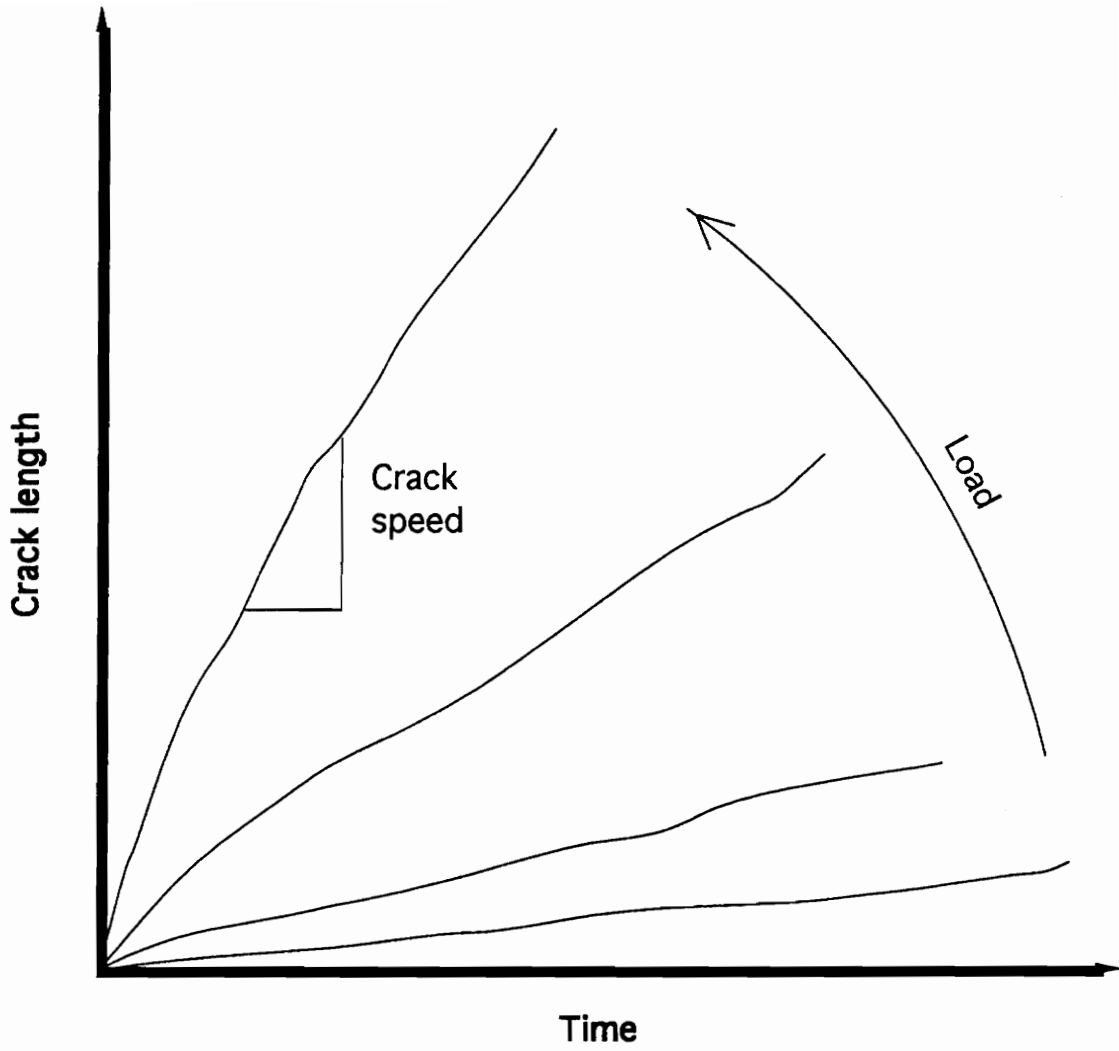


Figure 3.8. Crack length vs. time for a representative 45° peel specimen.

3.5.3 Water Immersion, Temperature and Relative Humidity Control for the 45°

Peel Test

In chapters IV and V, the peeling specimens were tested while immersed in ambient temperature water. This was accomplished by placing a polyethylene cooler under the sample holder and filling it with deionized water. The cooler was then moved into place so the peel sample was immersed in the water by raising or lowering a standard lab jack.

In chapters VI through VIII, the adhesive specimens were tested while controlling both the temperature and relative humidity. The temperature was controlled over a range of 5 to 90 +/- 0.5 °C, and the relative humidity was controlled between 5 and 85 +/- 0.5% relative humidity. A new peel specimen holder was constructed inside a fiberglass insulated galvanized steel box as detailed in Figure 3.9. The building air supply was used to convert the box into a forced air oven. Figure 3.10 contains a schematic diagram of the air stream and control system for maintaining constant temperature and relative humidity at temperatures above ambient. The air stream was regulated to 27 kPa then filtered and dried in a column containing Drierite®. The dry air stream was split and the flow balanced with precision needle valves and an electric solenoid valve. One side of the air stream was bubbled through deionized water which

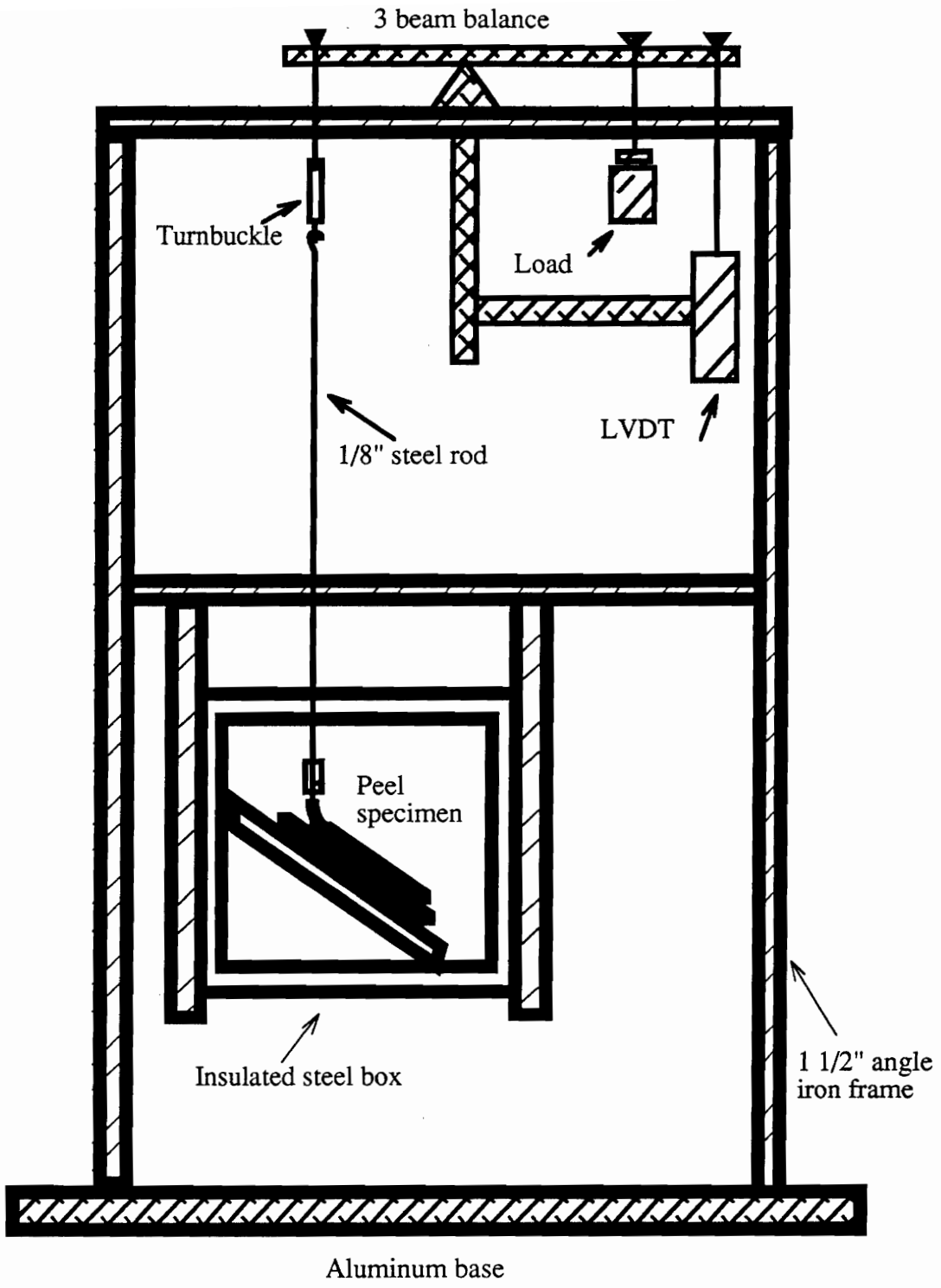


Figure 3.9. 45° peel specimen mounted in an insulated box.

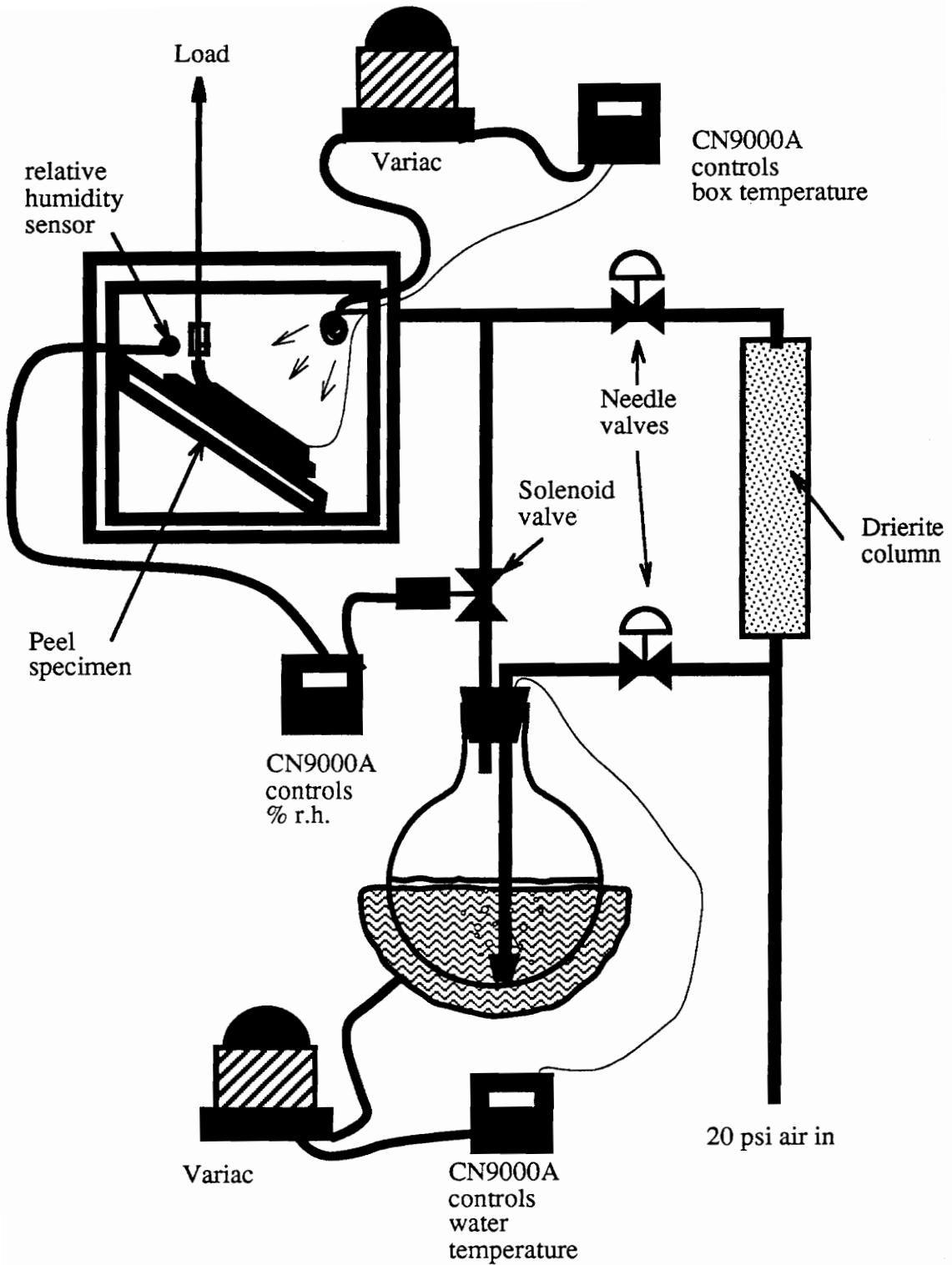


Figure 3.10. Control system for maintaining constant temperature and relative humidity for temperatures above ambient.

was heated to five degrees less than the oven temperature using a heating mantle and temperature controller. This wet stream was combined with the dry stream and fed into the oven where it was heated in a copper coil which was wrapped around a resistance heater. The temperature was controlled with a CN9000A temperature controller connected to the resistive heater and a K-type thermocouple imbedded in the sealant.

A relative humidity sensor was designed and constructed based on a circuit supplied by Panametrics Inc., Waltham, MA. The output of the sensor was calibrated and scaled to 0 to 20 mV. The MC 2 relative humidity sensitive capacitor was obtained from Panametrics. The entire circuit can be seen in Figure 3.11. This output from the sensor circuit was fed into a CN9000A controller from Omega. The controller was used to operate the solenoid valve which turned on and off the wet air stream.

The sub-ambient temperature flow diagram can be seen in Figure 3.12. A cold trap and copper coil heat exchanger were added to the dry air stream to lower the air temperature. The heat exchanger was a 4 liter dewar filled with isopropyl alcohol and dry ice. The wet air stream is not sent directly to the insulated box and not combined with the cold air stream until after the cold air has left the resistive heater.

3.5.4 Pure Shear Tensile Butt Joint

The test specimens were prepared as described earlier in Fig. 3.3. A 5 mm pre-crack was made in the sealant next to the aluminum on one end of the specimen by carefully cutting the sealant with a razor blade as seen in Fig. 2.7c. Crack growth at

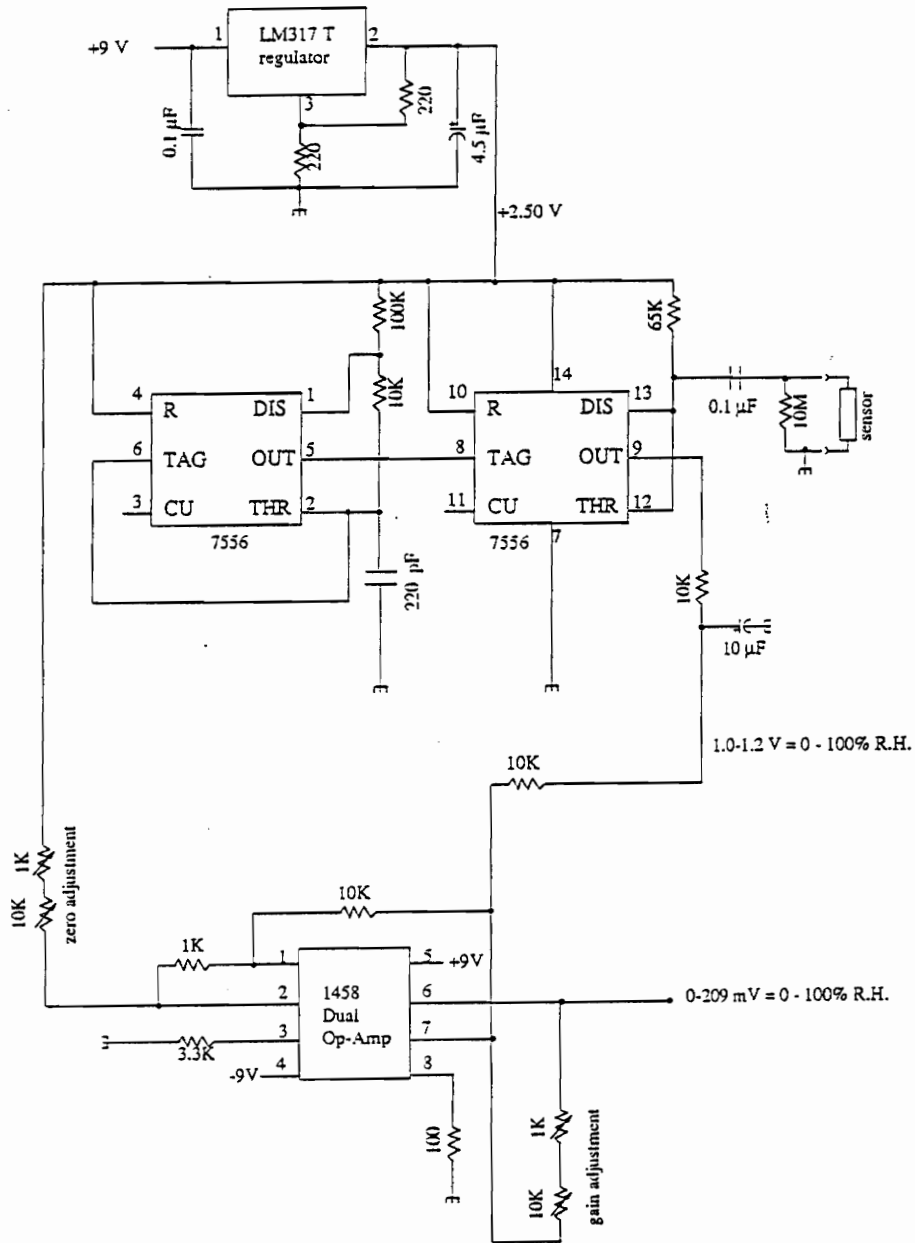


Figure 3.11. Circuit for measuring relative humidity. Output is linear 0 to 20 mV.

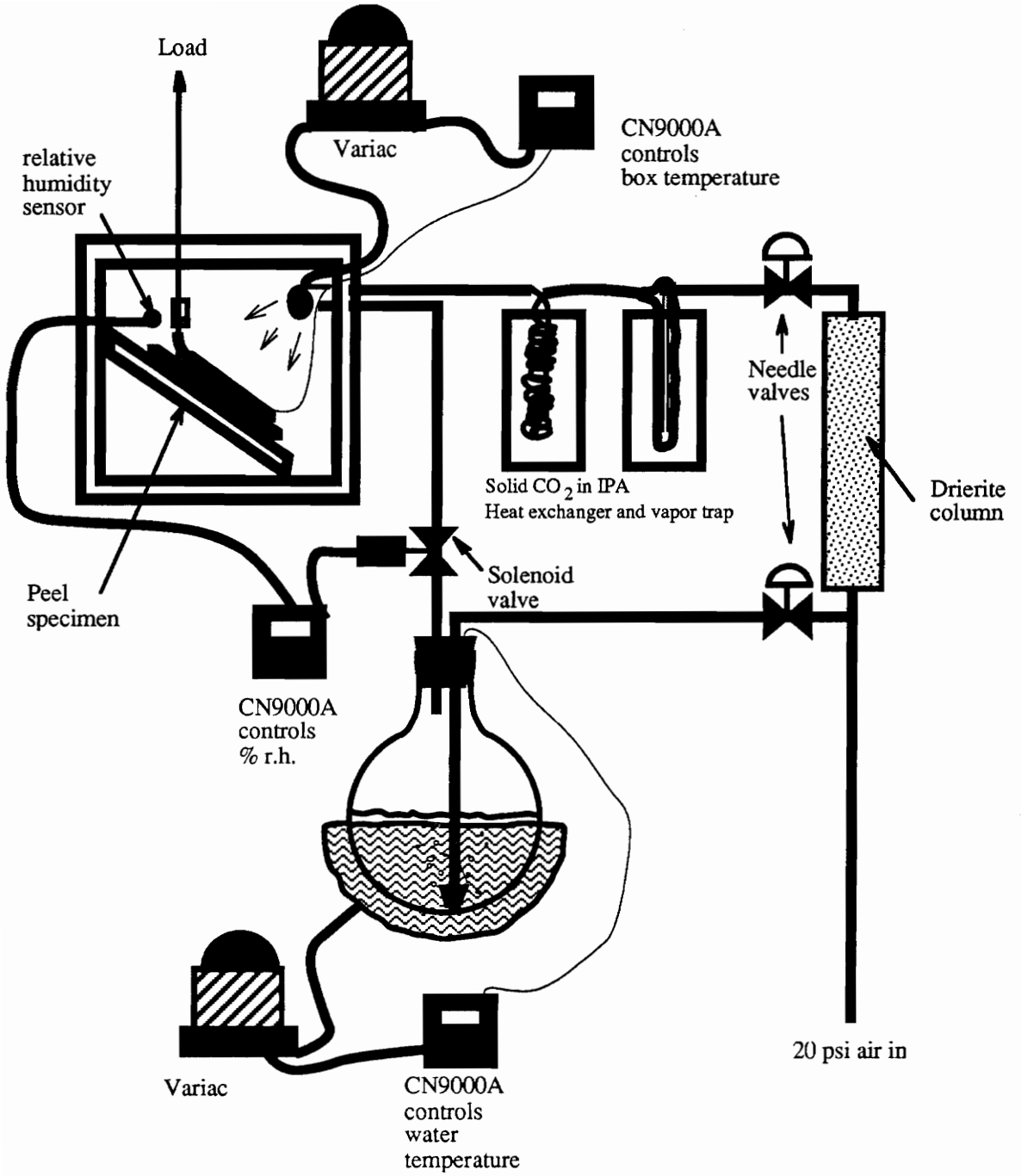


Figure 3.12. Control system for maintaining constant temperature and relative humidity for temperatures below ambient.

constant displacement was measured using the cathetometer and stress relaxation frame depicted in Figure 3.4. After the sample was allowed to come to equilibrium temperature, usually 20 minutes, a small displacement was applied to the joint by adjusting the turn buckle and crack growth was monitored.

3.6 References

- ¹ J. M. Klosowski, *Sealant in Construction*, Marcel Dekker, Inc., New York (1989).
- ² H. Cochrane and C. S. Lin, *Rubber World*, August, (1985).
- ³ M. Mantel, N. E. Shephard and J. P. Wightman, submitted to *Journal of Adhesion*, July 1995.
- ⁴ M. Mantel and J. P. Wightman, *Surface and Interface Analysis*, **21**, 595 (1994).
- ⁵ T. A. Carlson, *Surface and Interface Analysis*, **4**, 125 (1982).
- ⁶ P. L. J. Gunter, *Surface and Interface Analysis*, **19**, 161 (1992)
- ⁷ A. N. Gent and S. Y. Kaang; *J. Adhesion*, **24**, 173 (1987)

Chapter IV. Results and Discussion:

Effect of Peeling Thickness, Sealant Modulus and Peel Rate on 180° Peel

Adhesion of Silicone Sealant to Glass and Aluminum

The performance of a sealant is often assessed by 180° peel adhesion. The common parameters measured are peel force and failure mode at one test speed and temperature. The failure mode is determined by visual inspection. The peel force is a function of the peeling rate, peeling thickness, temperature, and strength of the interphase. An understanding of how these variables interact is necessary in order to translate the peel force results from one test configuration and speed to another. To facilitate this understanding, the peel force and failure mode in this study will be related to the sealant modulus, bond thickness, peeling rate and substrate type.

4.1 Sealant Characterization

Four different sealant formulations were prepared as described in section 3.1.1. The modulus of the sealant was varied by changing the ratio of polydimethylsiloxane- α,ω -dihydroxyl to polydimethylsiloxane- α,ω -dimethyl. The hydroxyl terminated polydimethylsiloxane is referred to as reactive polymer because the hydroxyl groups react with the methyltriacetoxysilane end-linker to link the ends of the polymer together during the curing reaction. The methyl terminated PDMS is referred to as the non-reactive polymer. The ratio of fumed silica to polymer was kept constant. The ratio of cross-linker to hydroxyl groups was also kept constant.

4.1.1 Sol and Gel Fraction

The cured sealant is a complicated system of fumed silica, cross-linker resin, catalyst, polydimethylsiloxane network, and uncross-linked polydimethylsiloxane. The extent of cross-linking was estimated by measuring the hexane soluble fraction of the silicone after curing for 2 weeks according to the procedure described in section 3.3.1. Table 4.1 contains the results of the swell and gel data. The analysis is complicated by the fact that fumed silica is added to the formulation along with excess cross-linker. The cross-linker residue is in the form of a methylsilsesquioxane resin. The fumed silica and cross-linker resin were assumed to be physically or chemically bonded to the polysiloxane network. Therefore, the weight of the silica and cross-linker is included in the polymer after swelling in hexane. After accounting for this added weight, the gel fraction and weight fraction were calculated. It was assumed that the volume of hexane in the swollen polymer was totally imbibed by the polymer and not by the fumed silica or resin. The gel data indicates that even the sealant formulation with no non-reactive polymer contains about 5% soluble polymer. This is consistent with the quality of the reactive polymer produced by condensation polymerization. The condensation polymer will contain approximately 5% cyclic polymer which may not react during the cross-linking process.¹

Figure 4.1 contains the gel fraction and soluble fraction data as a function of wt% reactive polymer for total polymer weight. The gel fraction increased as the amount of

Table 4.1 Sealant Swelling and Gel Data for Hexane Solvent.

Sealant formulation reference number	Initial weight, W_o , grams	Swollen weight, W_s , grams	Dry weight, W_g , grams	Swollen polymer volume fraction	Dry polymer gel fraction
45-1	0.538	1.994	0.516	0.179	0.957
	0.350	1.279	0.336	0.182	0.958
	0.231	0.792	0.221	0.195	0.953
	average			0.185	0.956
45-2	0.732	2.722	0.638	0.160	0.861
	0.586	2.208	0.511	0.157	0.863
	0.355	1.344	0.310	0.157	0.863
	average			0.158	0.862
45-3	0.520	2.033	0.403	0.132	0.759
	0.315	1.227	0.243	0.132	0.757
	average			0.132	0.758
45-4	0.698	2.919	0.471	0.105	0.653
	0.447	1.898	0.301	0.103	0.652
	0.304	1.284	0.205	0.104	0.652
	average			0.104	0.652

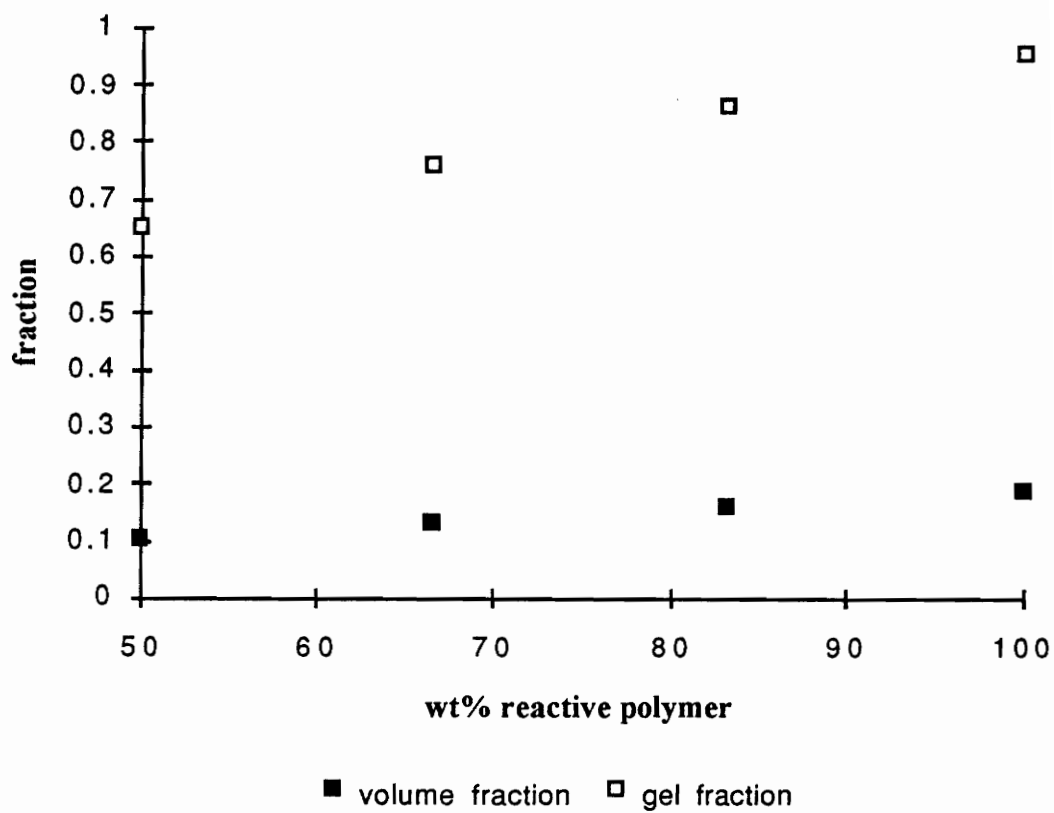


Figure 4.1 Volume fraction and gel fraction for sealants using hexane solvent.

reactive polymer in the formulation increased. This trend was expected. The volume fraction of polymer in the swollen network increased as the amount of reactive polymer in the formulation increased suggesting a decrease in the cross-link density which is not readily explained.

4.1.2 Modulus

4.1.2.1 Equilibrium conditions

The sealant responds to stresses in a viscoelastic manner. The PDMS network has the physical characteristics of a viscoelastic solid. The solvent soluble PDMS fraction has the physical characteristics of a viscoelastic liquid. When the sealant is stressed at a high rate, the viscous portion of the material response dominates the outcome. At low stress rates, the viscous portion of the material response is negligible. At slow rates, only the elastic portion of the polymer response is evident. The elastic portion of the polymer response originates mainly from the polymer network or gelled PDMS. Equilibrium stress vs. strain data separates the viscous portion of the response from the elastic portion. The viscous portion completely decays under equilibrium conditions to yield only the elastic contribution.

The equilibrium stress vs. strain was measured according to section 3.3.2.1. The stress vs. strain isotherms were analyzed by plotting the engineering strain vs. the engineering stress as shown in Figure 4.2. The energy to break per unit volume, W_b , can be calculated by taking the following integral:

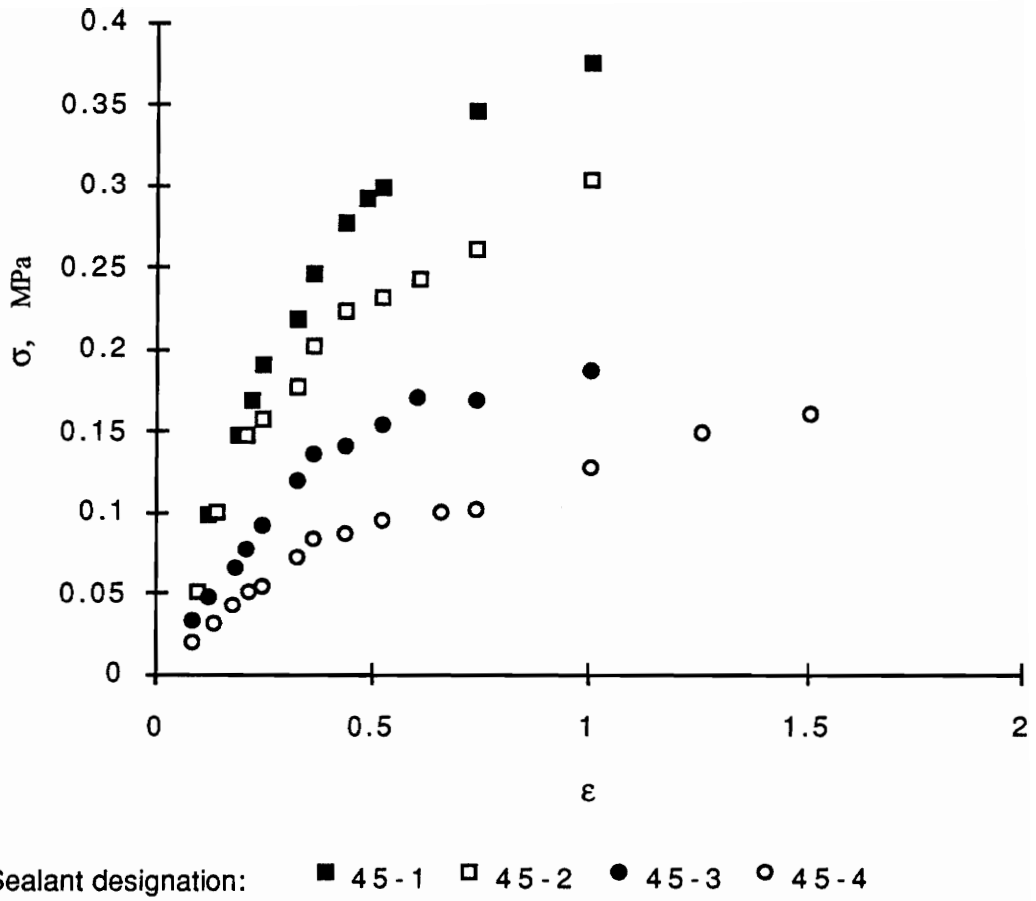


Figure 4.2 Stress vs. strain for equilibrium condition.

$$W_b = \frac{W}{A_0 l_0} = \int_0^{\epsilon_b} \sigma d\epsilon \quad (4.1)$$

where A_0 is the initial area, l_0 is the initial length of the neck of the dogbone and W is the work done per increment of strain. The term ϵ is $(l-l_0)/l_0$ where l is the new length of the stretched neck, and ϵ_b is the strain to break. The quantity σ is F/A_0 where F is the force on the dogbone. The slope of the line tangent to the origin yields the engineering modulus. The strain to break, stress to break, modulus, and energy to break for the four sealants can be found in Table 4.2. In Figure 4.3, the energy to break is plotted against the gel polymer fraction based on the gel fraction data from Table 4.1. The energy to break was higher for the more highly gelled sealant. This is expected because the network has more elastically active chains than the less gelled sealant. Only the elastically active chains contribute to the equilibrium stress strain data.

If the sealant is assumed to behave according to the statistical theory of rubber elasticity in a Gaussian manner, the stress can be related to the strain by a complex function of the strain.² The function is $\lambda - \lambda^{-2}$ for simple extension where λ is the extension ratio defined as l/l_0 .³ The following equation relates the stress to the strain function using the proportionality constant E , the tensile modulus:

$$3\sigma = E(\lambda - \lambda^{-2}) \quad (4.2)$$

Table 4.2 Stress vs. strain summary for equilibrium strain.

Sealant designation	Strain to break	Stress to break, MPa	Modulus, MPa		Energy to break, GJ/m ³
			Young's	Gaussian chain elastomer	
45-1	1.0	0.38	0.59	0.84	0.85
45-2	1.0	0.30	0.51	0.69	0.69
45-3	1.0	0.19	0.37	0.48	0.42
45-4	1.5	0.16	0.22	0.27	0.50

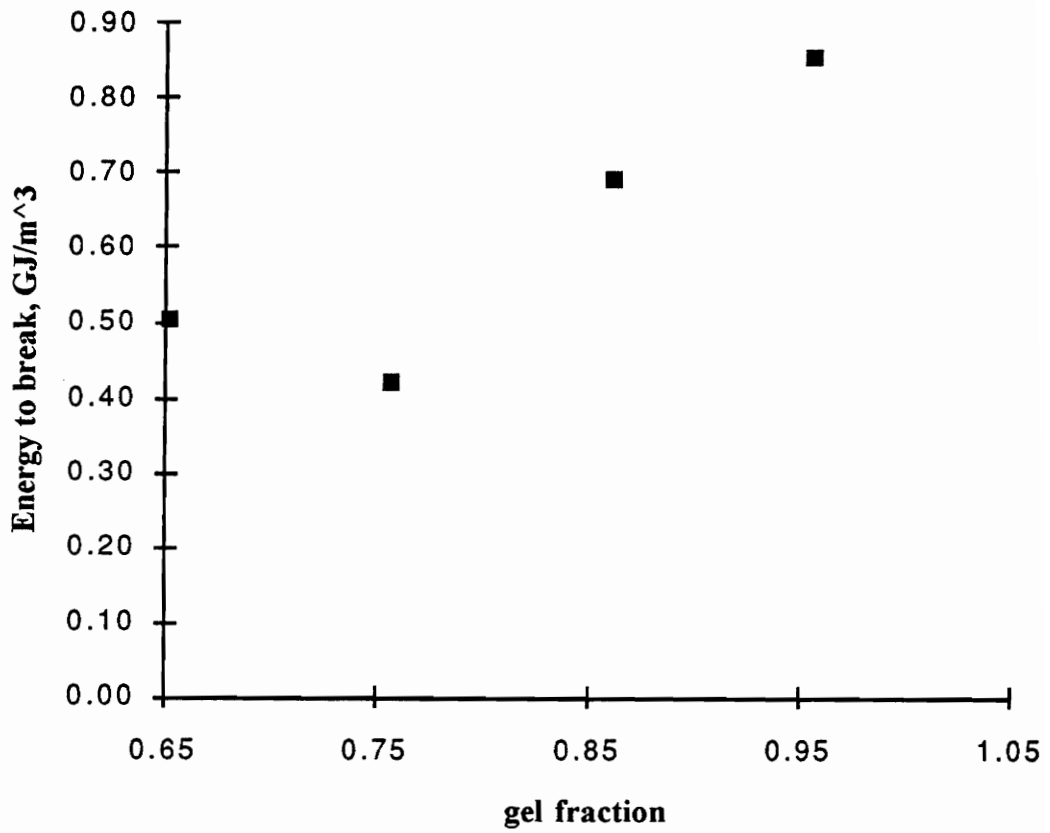


Figure 4.3. The energy to break vs. gel fraction under equilibrium.

Figure 4.4 contains the results of the above analysis for the equilibrium data. The modulus was calculated from the linear region of the curves extending from 0 to 0.4 on the x-axis and can be found in Table 4.2. The Young's modulus and statistical elastomer modulus are plotted against the PDMS gel fraction in Figure 4.5. The modulus decreased as the gel fraction decreased.

4.1.2.2 Test Rate of 0.33 s^{-1}

Stress vs. strain isotherms were obtained using the methods described in section 3.3.2.2. The data was analyzed exactly as in 4.1.2.1. The stress vs. strain isotherms can be found in Figure 4.6. The sealant is much tougher at the non-equilibrium straining rate. This occurs because the viscous portion of the polymer response is significant under non-equilibrium conditions. Under equilibrium conditions, the viscous component of the polymer physical response is absent. Table 4.3 contains the data for strain to break, stress to break, modulus and energy to break.

As can be expected, the strain to break increased with increasing diluent level. The stress to break and the modulus were both reduced by adding diluent. Figure 4.7 plots the energy to break vs. the gel fraction for both the equilibrium data and the 0.33 s^{-1} strain rate. The sealants' viscoelastic response is plainly evident. For the equilibrium data, the viscous component of the material response is minimal and the energy to break increased as the gel fraction increased. This is due to an increase in number of elastically effect network chains. The trend is reversed for the 0.33 s^{-1} strain rate data. The highly

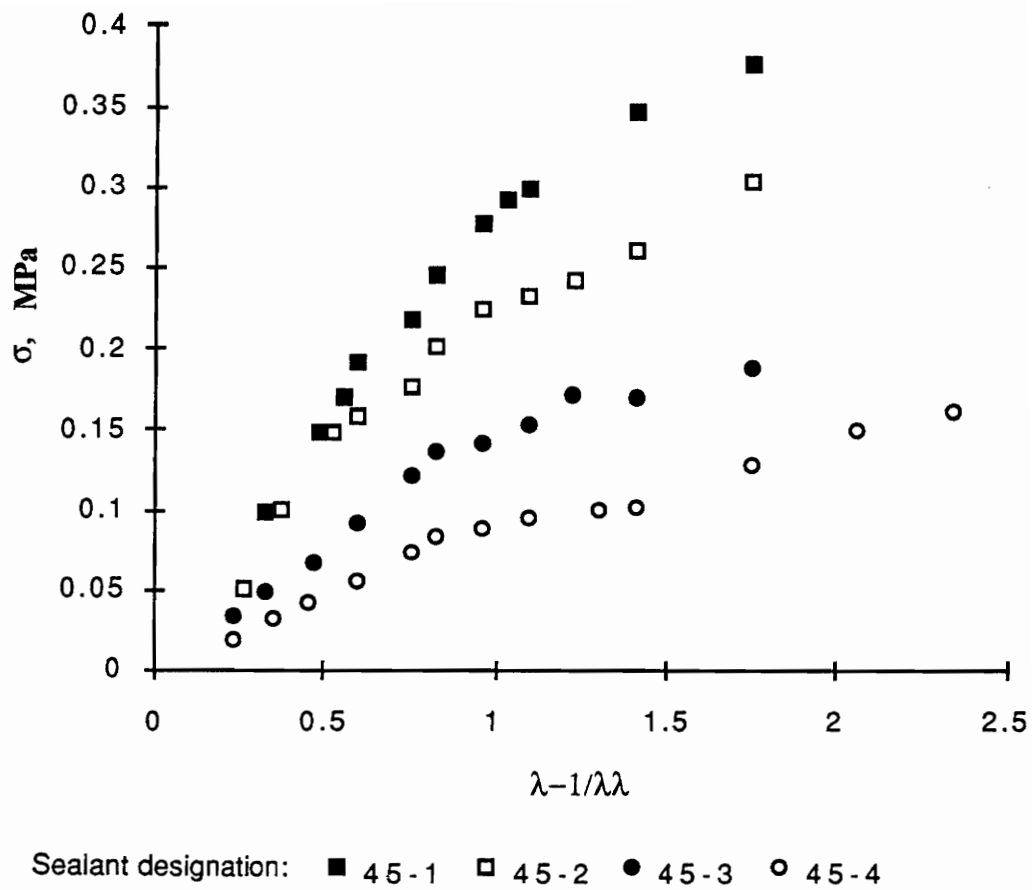


Figure 4.4. Stress vs. strain for Gaussian chain elastomer model at equilibrium.

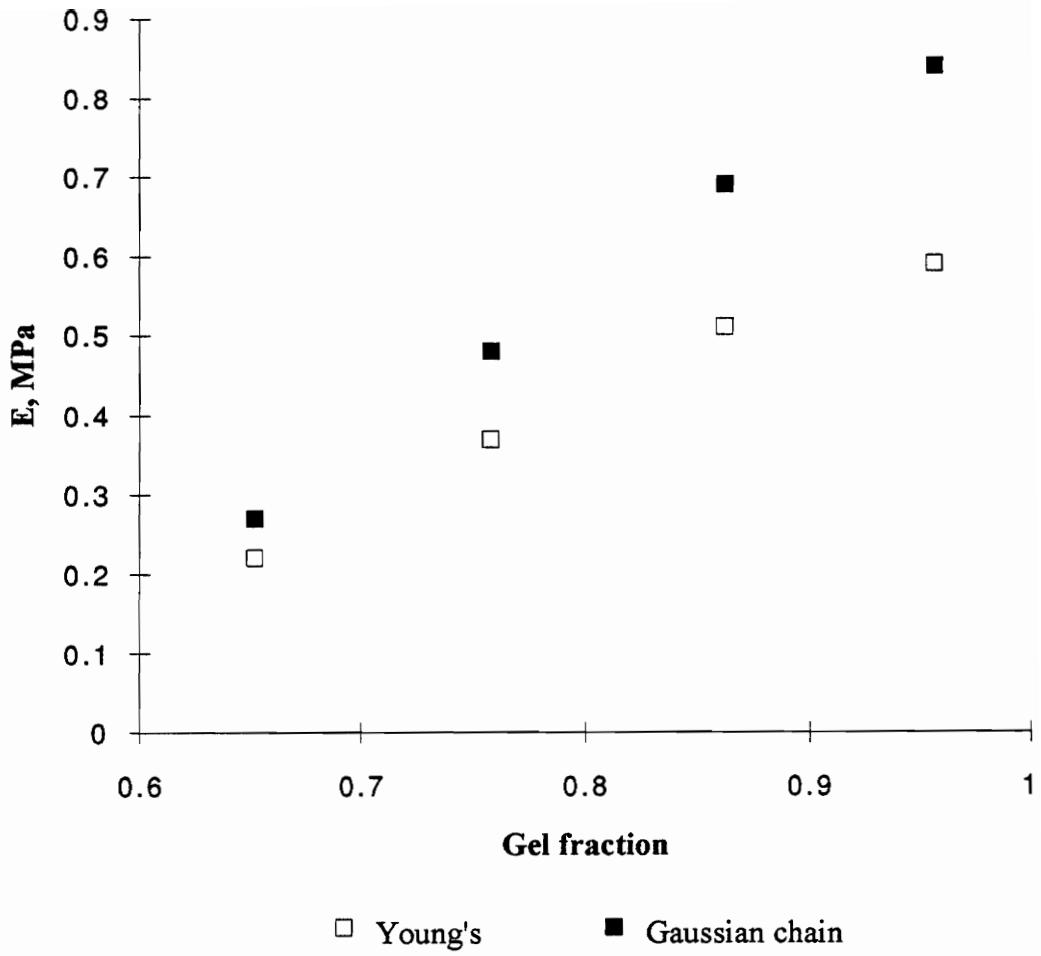


Figure 4.5. Modulus vs. gel fraction under equilibrium conditions.

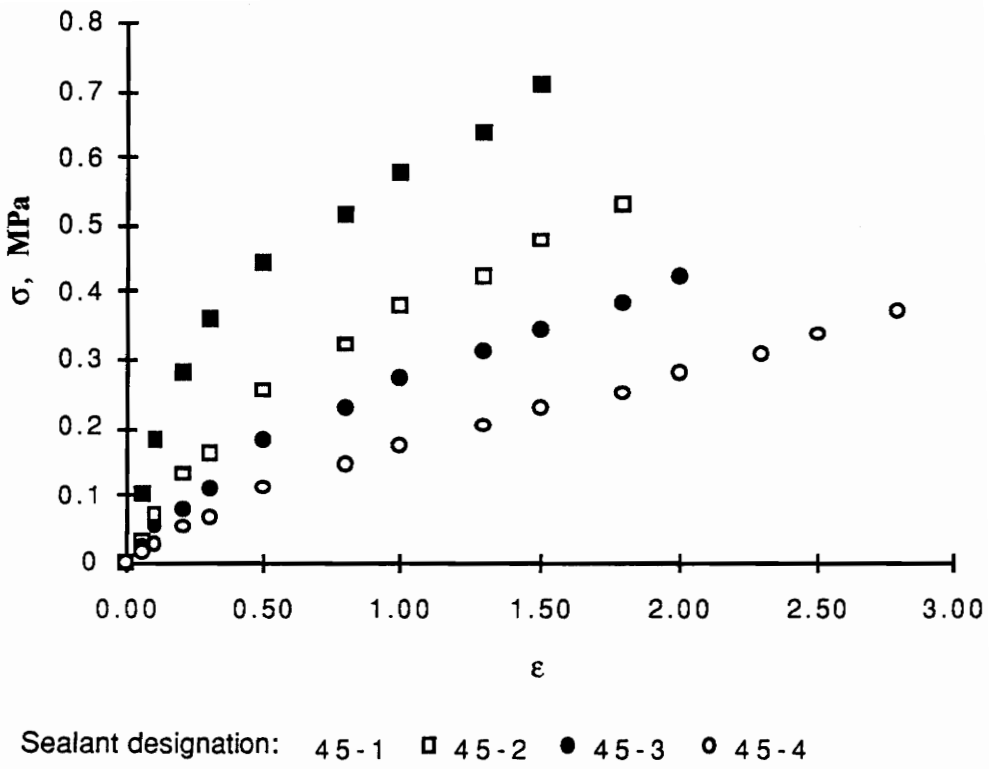


Figure 4.6. Stress vs. strain at 0.33 s^{-1} strain rate.

Table 4.3 Stress vs. strain summary for 0.33 s^{-1} strain rate.

Sealant designation	Strain to break	Stress to break, MPa	Modulus, MPa		Energy to break, GJ/m^3
			Young's	Gaussian chain elastomer	
45-1	1.5	0.71	1.16	1.26	1.25
45-2	1.8	0.53	0.55	0.72	2.02
45-3	2	0.47	0.37	0.51	1.91
45-4	2.8	0.37	0.21	0.3	1.91

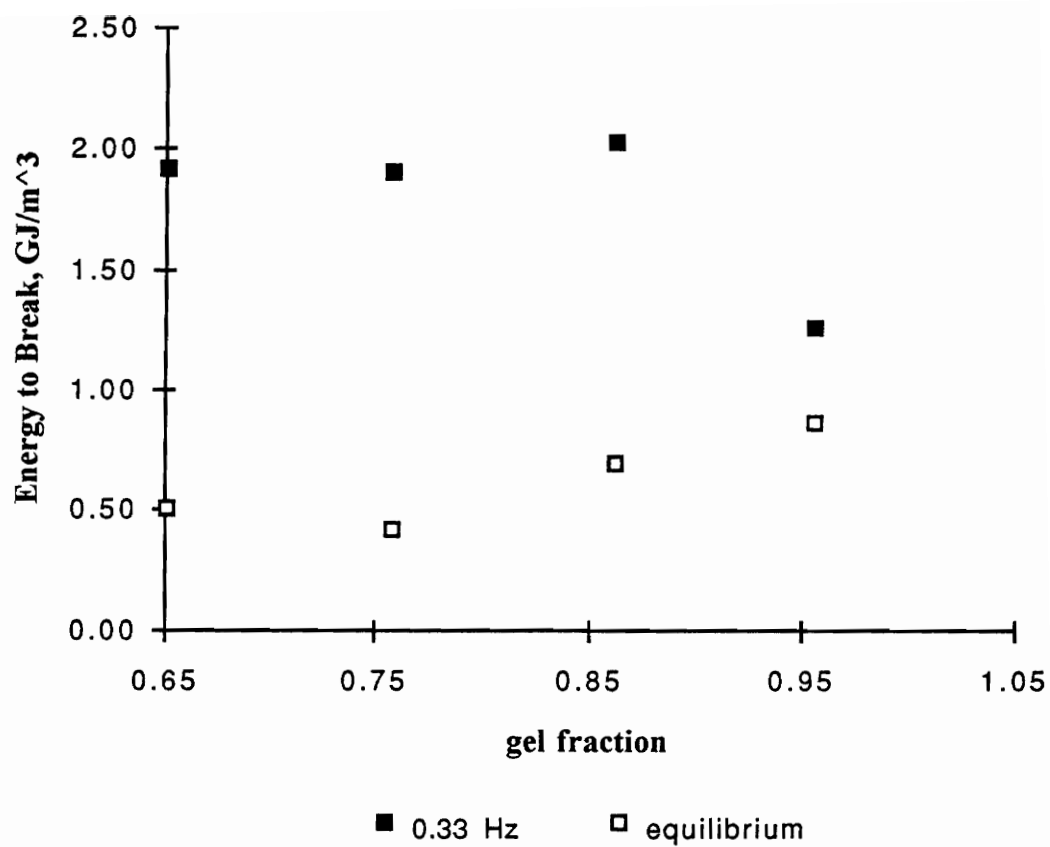


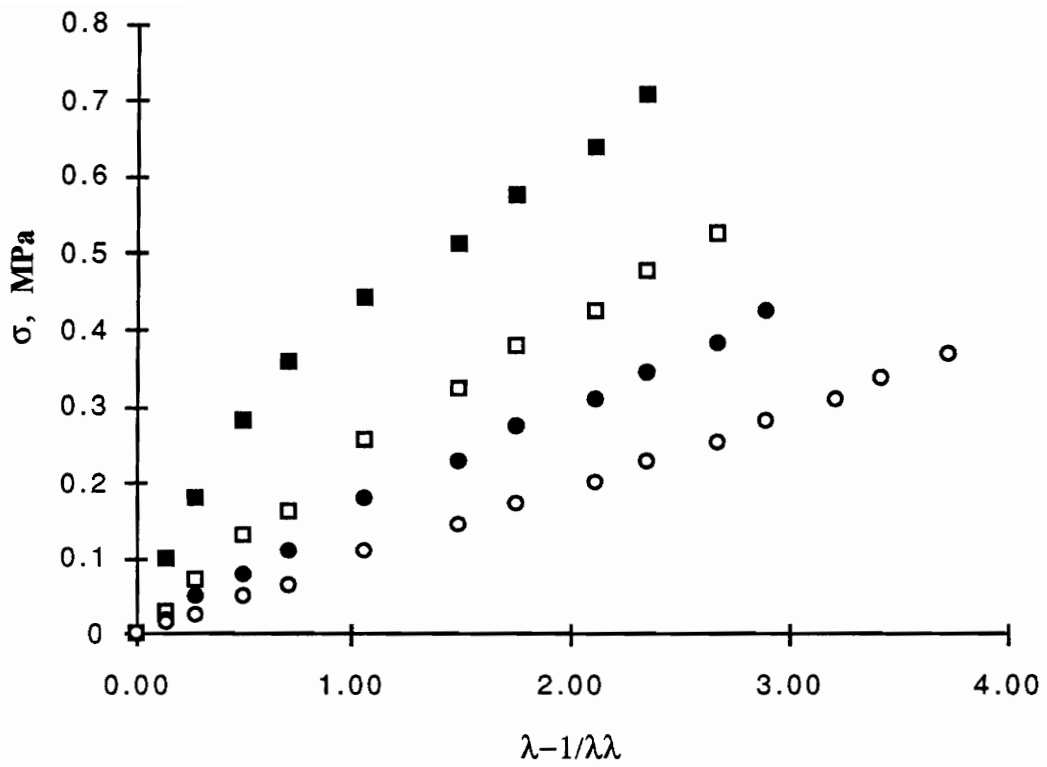
Figure 4.7. Energy to break for equilibrium and 0.33 s⁻¹ strain rate vs. gel fraction.

gelled sealant has the lowest energy to break. For the 0.33 s^{-1} data, the material response included the viscous response of the sealant. Reducing the gel fraction increased the magnitude of the viscous component of the material response. This indicates that the material response of the sealant is governed by the gel fraction for very slow strain rates and by the non-reacted polymer fraction when the strain rate is high.

The stress vs. strain curves for the ideal elastomer analysis at 0.33 s^{-1} strain rate can be found in Figure 4.8. The ideal elastomer model and Young's model are compared to the equilibrium data as a function of gel fraction in Figure 4.9. In all cases, the modulus increased as the gel fraction increased. The models tend to diverge as the gel fraction increased.

4.2 Peel Adhesion

The independent variables for the peel test study were peeling rate, fiberglass cloth embedded depth, sealant modulus, and substrate type. The dependent variables studied were peel force and failure mode. Three pulls of each sample condition were averaged as described in section 3.5.1. The strain energy release rate was calculated according to equation 3.6. A log-log plot of the strain energy release rate against the peeling rate resulted in straight lines for each thickness and modulus condition. The effect of thickness can be corrected by plotting the strain rate instead of the peeling rate. This is analogous to measuring strain rate instead of cross head speed for a uniaxial tension experiment. The strain rate can be estimated by the following equation:⁴



Sealant designation: ■ 45-1 □ 45-2 ● 45-3 ○ 45-4

Figure 4.8. Stress vs. strain for Gaussian chain elastomer model at strain rate of 0.33 s^{-1} .

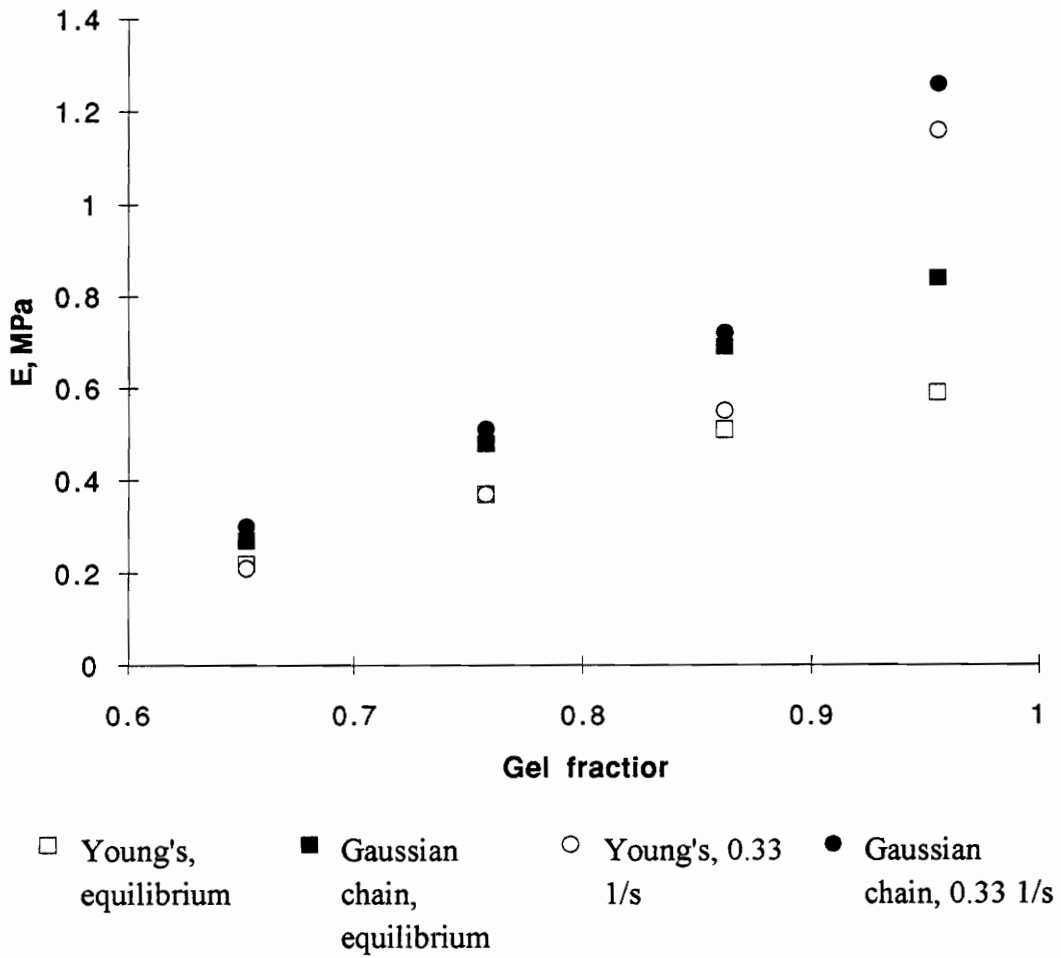


Figure 4.9. Modulus for Gaussian chain elastomer model and Young's modulus vs. gel fraction under equilibrium conditions and for strain rate of 0.33 1/s.

$$\dot{\epsilon} = \frac{\dot{a}}{b} \quad (4.3)$$

where $\dot{\epsilon}$ is the strain rate and \dot{a} is the peeling rate. The gauge length is assumed to be the same as the strained thickness, b , defined in section 3.5.1. At constant peeling rate, the strain rate increases as the strained thickness decreases. A linear fit of the data results in the following equation for fracture energy, \mathcal{G} :

$$\mathcal{G} = k\dot{\epsilon}^n \quad (4.4)$$

where k is a constant related to the thermodynamic work of adhesion and n is a constant which is related to rate dependent dissipation. Immediately it is seen that increasing the strained thickness will result in a lower effective strain rate and lower the strain energy release rate as previously reported by Gutowski, Russell and Cerra.⁵

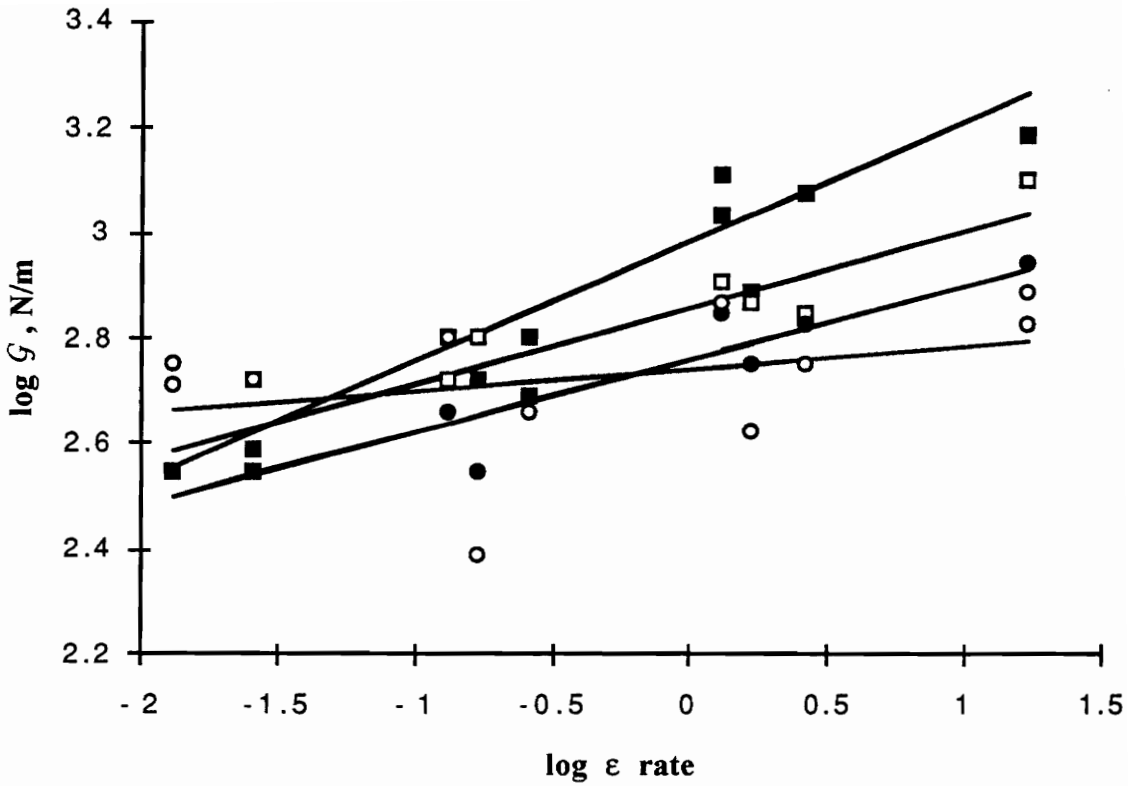
4.2.1 Glass Substrate

All the specimens with the exception of one, failed cohesively in the strained sealant region as seen in Table 4.4. The calculated fracture energies are an average of three samples. The log fracture energy is plotted against the log strain rate in Figure 4.10. The data can be fit to a straight line for each sealant formulation. The regression data is found in Table 4.5. Increasing the gel fraction decreased the exponent, n , and decreased the intercept, k .

The decrease in “ n ” indicates a reduction in rate dependence. The rate dependent portion of the material response is mainly the viscous portion. Therefore, increasing the gel fraction reduced the rate dependence of the fracture energy as seen in Figure 4.11.

Table 4.4 Summary of adhesion test results for sealant on glass and aluminum.

peeling rate (mm/s)	sealant Modulus (MPa)	constrained thickness (mm)	aluminum substrate		glass substrate	
			fracture energy (N/m)	failure mode 0=adh. 1=coh.	fracture energy (N/m)	failure mode 0=adh. 1=coh.
0.084	0.21	0.5	35	0.0	525	1.0
0.084	0.21	3.2	35	0.0	385	1.0
0.084	0.21	3.2	35	0.0	350	1.0
0.084	0.21	6.4	245	1.0	350	1.0
0.840	0.21	0.5	280	0.5	771	1.0
0.840	0.21	3.2	350	0.5	630	1.0
0.840	0.21	6.4	701	1.0	630	1.0
8.400	0.21	0.5	1751	1.0	1541	1.0
8.400	0.21	3.2	1576	1.0	1191	1.0
8.400	0.21	6.4	1296	1.0	1086	1.0
8.400	0.21	6.4	1136	1.0	1289	1.0
0.084	0.37	0.5	140	0.0	630	1.0
0.084	0.37	3.2	105	0.0	525	1.0
0.084	0.37	6.4	350	0.0	350	1.0
0.840	0.37	0.5	210	0.0	736	1.0
0.840	0.37	3.2	53	0.0	490	1.0
0.840	0.37	6.4	175	0.0	525	1.0
8.400	0.37	0.5	701	0.5	1261	1.0
8.400	0.37	3.2	806	0.5	701	1.0
8.400	0.37	6.4	841	1.0	806	1.0
0.084	0.55	0.5	105	0.0	350	0.5
0.084	0.55	3.2	53	0.0	350	1.0
0.084	0.55	6.4	350	0.0	350	1.0
0.840	0.55	0.5	70	0.0	560	1.0
0.840	0.55	3.2	35	0.0	490	1.0
0.840	0.55	6.4	455	1.0	455	1.0
8.400	0.55	0.5	280	0.5	876	1.0
8.400	0.55	3.2	175	0.0	665	1.0
8.400	0.55	6.4	701	1.0	701	1.0
0.084	1.16	0.5	53	0.0	245	0.0
0.084	1.16	3.2	70	0.0	525	1.0
0.084	1.16	6.4	385	0.0	560	1.0
0.084	1.16	6.4	352	0.0	509	1.0
0.840	1.16	0.5	70	0.0	420	1.0
0.840	1.16	3.2	53	0.0	455	1.0
0.840	1.16	6.4	455	1.0	630	1.0
8.400	1.16	0.5	140	0.0	665	1.0
8.400	1.16	0.5	175	0.0	771	1.0
8.400	1.16	3.2	210	0.5	560	1.0
8.400	1.16	6.4	560	1.0	736	1.0



Sealant designation: ■ 45-1 □ 45-2 ● 45-3
 ○ 45-4 ——— calc.

Figure 4.10. Log of fracture energy vs. Log of strain rate for sealant adhesion to glass.

Table 4.5 Regression data for glass adhesion.

Sealant Designation	Gel Fraction	Young's Modulus, MPa	Energy to break, GJ/m ³	k	n
45-1	0.956	1.16	1.25	552(0.044)	0.043(0.038)
45-2	0.862	0.55	2.02	577(0.020)	0.138(0.019)
45-3	0.758	0.37	1.91	723(0.024)	0.145(0.024)
45-4	0.652	0.21	1.91	896(0.024)	0.229(0.023)

* numbers in parenthesis are standard error of estimate.

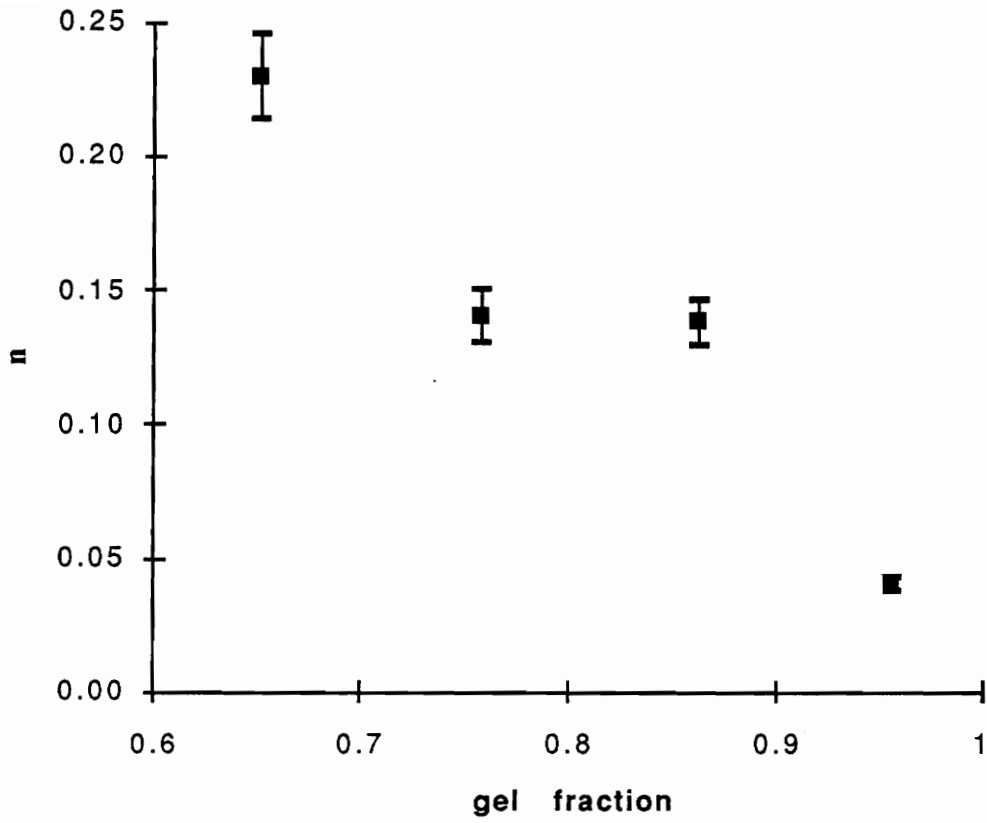


Figure 4.11. Correspondence of n with gel fraction for glass fracture data. 95% confidence limits included.

The constant n can be loosely correlated to the energy to break. This is consistent with the fact that the energy to break and the constant n are both related to the amount of dissipation which is occurring during the experiment. The fact that the level of dissipation is increasing precludes the use of equation 2.3.

The constant k also increased with decreasing modulus. However, this may not indicate an increase in the threshold or intrinsic fracture energy. In fact, the fracture energy for the high modulus sealant was greater at low strain rates than the fracture energy for the lower modulus sealant. This suggests that the intrinsic fracture energy of the high modulus sealant may be greater than that of the low modulus sealant. The high rate data suggests the opposite trend just as seen for the strain energy to break data. This is an excellent example of the problems associated with measuring fracture energy at only one rate.

4.2.2 Aluminum Substrate

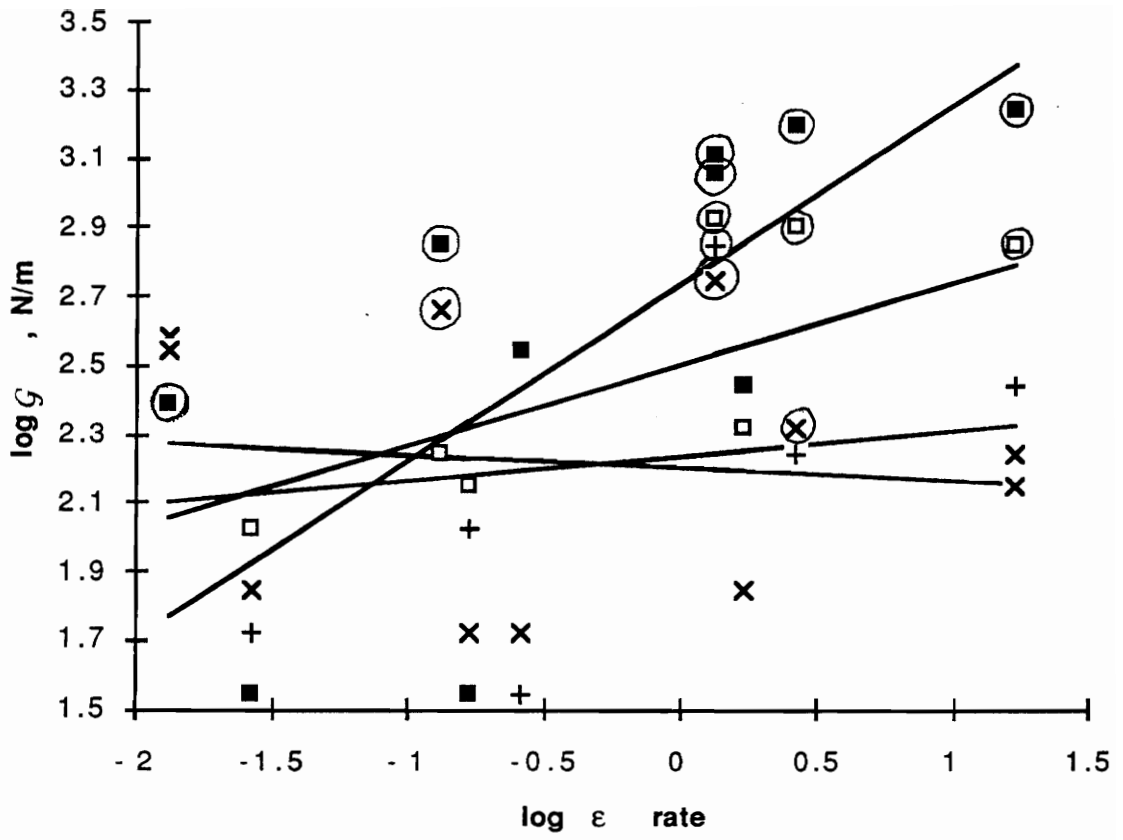
The aluminum data is much more difficult to interpret than the results for the glass substrate. Peel strength was strongly influenced by the failure mode. For the aluminum adherend, the failure mode switched between adhesive and cohesive at various points within the experiment design space as seen in Table 4.4. For purposes of comparison, the aluminum data was analyzed according to equation 4.3. The regression analysis was poor which is expected because the assumptions inherent in equation 4.2 are no longer valid. The dissipation due to straining of the sealant will be lower when the

failure mode is adhesive. This occurs because the crack propagates before the sealant is strained to break. The log fracture energy vs. log strain rate can be found in Figure 4.12. The highest strain energy release rates can be correlated directly with cohesive failure. In addition, the trends of modulus and strain rate were similar to that of the glass data as seen in Table 4.6. compared to Table 4.5.

Wide variations in peeling angle can be sighted as an additional source of variation between the experimental data and the calculated data from equation 4.4. Changes in the stiffness of the peeling member can occur due to changes in the thickness and modulus of the member. Such changes in stiffness result in changes in the bending moment. The peeling angle was never measured during the test. However, visual examination during the peel test indicated that the angle could be nearly 180° or as low as 45° depending on the test conditions and failure mode. Gent and Kaang have suggested using a lower peeling angle to minimize the bending moment during peeling.⁶ However, the angle should not be so low as to strain the bending member axially. Therefore, a 45° peel angle was suggested as a good compromise.

4.2.3 Failure Mode Changes

The aluminum test specimens failed adhesively or cohesively depending on the test conditions. As seen in Figure 4.13, cohesive failure occurred more frequently when the sealant modulus has decreased, the peeling rate was increased or when the peeling



Sealant designation: ■ 45-1 □ 45-2 + 45-3
 × 45-4 — calc.

Figure 4.12. Log of fracture energy vs. Log of strain rate for sealant adhesion to aluminum. Circles indicate cohesive failure. Otherwise mixed mode or adhesive failure occurred.

Table 4.6 Regression data for aluminum adhesion.

Sealant Designation	Gel Fraction	Young's Modulus, MPa	Energy to break, GJ/m ³	k	n
45-1	0.956	1.16	1.25	159(0.13)	-0.04(0.11)
45-2	0.862	0.55	2.02	173(0.17)	0.07(0.17)
45-3	0.758	0.37	1.91	320(0.14)	0.24(0.18)
45-4	0.652	0.21	1.91	550(0.16)	0.52(0.15)

* numbers in parenthesis are standard error of estimate.

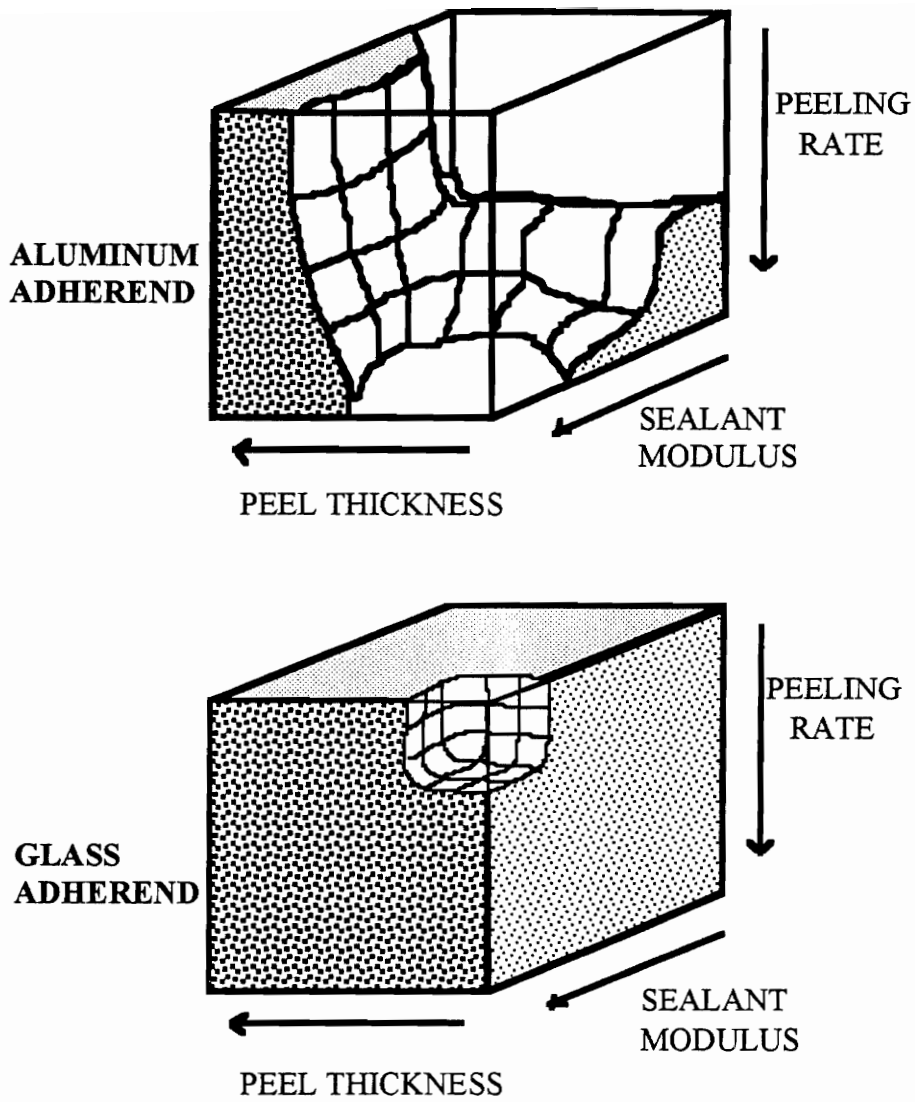


Figure 4.13 Region of cohesive failure for glass and aluminum. Void areas represent adhesive failure.

thickness was increased. Adhesive failure resulted when the stress was concentrated near the interphase. This occurred when the strained thickness is small. In addition, slow strain rates allowed the sealant to relax and transfer the stress to the interphase.

The same trends are also seen for the glass data. However, the total occurrence of cohesive failure has much higher for the glass substrate indicating better adhesion at the interface of the glass substrate than at the interface of the aluminum substrate. This can be explained by the different surface chemistry which is possible on the glass surface as compared to the aluminum surface. The glass surface contains hydroxyl groups which can participate in the condensation reaction of the sealant when it cures. A similar reaction can occur in the aluminum hydroxide layer on the aluminum substrate. However, the resulting bond may not be as stable.

4.3 Summary

The adhesion of a model sealant formulation to glass and aluminum was tested using the 180° peel test. The glass test specimens failed cohesively through the sealant for all but one condition. The fracture energy has related to the test geometry, peeling rate, and sealant modulus. For instances of cohesive failure, a power law model for fracture energy applied. The peeling rate of the crack was not used. Instead, the strain rate of the sealant was used to correct for the changes in sealant thickness. As the modulus of the sealant decreased, the rate dependence increased. This suggested an increase in the amount of dissipation in the sealant as the amount of unreacted polymer

has increased. In general, the fracture energy increased for the sealants with higher levels of dissipation. However, fracture energy measurements taken at lower strain rates suggested that the higher modulus sealant may have better adhesion than the lower modulus sealant.

The aluminum test specimens failed adhesively or cohesively depending on the test conditions. Cohesive failure yielded a high fracture energy. Cohesive failure occurred more frequently when the sealant modulus was decreased, the peeling rate was increased, or when the peeling thickness was increased. Adhesive failure resulted when the stress was concentrated near the interphase. This occurred when the strained thickness was small. In addition, slow strain rates allowed the sealant to relax and transfer the stress to the interphase. The glass data followed the same trends. However, the total occurrence of cohesive failure was much higher for the glass substrate indicating better adhesion at the interface of the glass substrate than at the interface of the aluminum substrate.

The above results highlight some important deficiencies in the ASTM peel test method. Peel testing at only one rate can not adequately compare one sealant to another.

4.4 References

¹ W. Noll, *Chemistry and Technology of Silicones*, Academic, New York, (1984).

² P. J. Flory, *Principles of Polymer Chemistry*, Cornell University Press, Ithica, New York (1953).

³ L. R. G. Treloar, *The Physics of Rubber Elasticity*, 3rd ed., Clarendon, Oxford (1975).

⁴ A. N. Gent and R. P. Petrich, *Proceedings of the Royal Society*, **A310**, 433 (1969).

⁵ W. S. Gutowski, L. Russell, and A. Cerra, "New Tests for Adhesion of Silicone Sealants," *Science and Technology of Building Seals, Sealants, Glazing and Waterproofing: Second Volume, ASTM STP 1142*, ed. J. M. Klosowski, American Society for Testing and Materials, Philadelphia, Pennsylvania, (1992).

⁶ A. N. Gent and S. Y. Kaang, *J. Adhesion*, **24**, 173 (1987).

V. Results and Discussion:

45° Peel Adhesion of Silicone Sealant to Aluminum and Glass under Wet and Dry conditions

The variability of the 180° peel test was demonstrated in the previous section. In the 180° peel test, the peeling angle changes when tested at different rates or under different failure modes. Gent and Kaang have suggested that a 45° peel test would have less variability in peeling angle.¹ In addition, the bending moment for the 45° peel test would be lower.

The 180° peel test, as conducted in the ASTM method C-794, tends to yield cohesive failure. Reducing the peel rate and reducing the peeling thickness can increase the likelihood of failure near the interphase. Under long term durability conditions, the sealant joint often fails near the interphase. Therefore, short term experiments need to produce failure near the interphase in order to correlate with long term conditions.

In this study, the 45° peel test was used to measure the fracture energy of high modulus and low modulus sealants to glass and aluminum over a wide range of peeling rates. The specimens were tested in ambient laboratory air and under water at room temperature. The rate dependence of the fracture energy of the sealant to the two substrates for failure occurring very near the interface was obtained.

5.1 Sealant Characterization

The sealant formulations used for this experiment are referenced 45-1 and 45-4 and are the same formulations from the previous section which were detailed in section 4.1. Formulation 45-1 is the high modulus formulation and 45-4 is the low modulus formulation.

5.2 Initial Surface Analysis by ESCA

After curing for 21 days at ambient conditions, the air exposed surface of the sealant was analyzed with ESCA. The results of the analysis can be found in Table 5.1. Although the sealant contained tin in the formulation, the level of tin was too small to be detected on the surface of the sealant. Carbon, silicon and oxygen were observed in the expected quantities for the silicone formulation.

The glass and aluminum samples were rinsed in chloroethane followed by acetone. After cleaning, the samples were analyzed by ESCA within 15 minutes after cleaning. Table 5.1 contains the results of the ESCA analysis. Significant amounts of carbon were still found on the surfaces of both substrates. The carbon came from organic contamination which was incompletely removed during the solvent rinse.

The glass surface also contained a significant amount of tin. The tin contamination occurred during the glass manufacturing process. As noted above, the level of tin in the sealant was too small to be detected by the ESCA technique. Thus, the tin can be utilized as a tag element to distinguish between the silicon present in the glass and in the sealant.

Table 5.1 ESCA analysis of cured sealant, solvent cleaned aluminum and solvent cleaned glass.

Electron	Sealant cured 21 days in air, 15° take-off angle	Sealant cured 21 days in air, 45° take-off angle	Sealant cured 21 days in air, 90° take off angle	Glass surface, solvent cleaned, 45° take-off angle	Aluminum surface, solvent cleaned, 45° take-off angle
C 1s	51.3	51.9	49.5	28.1	15.7
O 1s	22.3	21.6	23.9	46	54.9
Si 2p _{3/2}	26.3	26.5	26.5	19.5	
Sn 3d _{5/2}				1.2	
Zn 2p _{3/2}					0.6
Na 1s				3.5	
N 1s					1.0
P 2p _{3/2}					1.9
S 2p _{3/2}					3.1
Au 4f _{7/2}	0.1	0.1	0.1	1.2	
Al 2p _{3/2}				alloy	2.9
				oxide	22.9
				oxide	4.2
			thickness, nm		

The aluminum substrate contained two peaks for the Al 2p photopeak. The two peaks at 71.7 and 74.7 eV and can be assigned to the aluminum oxide and aluminum alloy respectively. Equation 3.2 can be used to ratio the intensity of the two peaks and the thickness of the oxide layer can be determined in this way. For the cleaned aluminum sample, the oxide thickness was calculated to be 4.2 nm.

5.3 Fracture Energy Measurement

The fracture energy of the sealant to the glass and aluminum substrates was measured using the 45° peel test as outlined in section 3.5.2. The dry peel testing was conducted at ambient air temperature of 21°C. The wet peel testing was conducted with the peel specimens submerged in a water bath at ambient temperature during the peeling test. The samples were tested without being aged in water. The logarithm of the fracture energy vs. the logarithm of the crack speed can be found in Figure 5.1.

5.3.1 Fracture Energy of Sealant on Glass

Sealant adhered well to cleaned glass. This is consistent with the chemical bonding and wetting theories for adhesion as described in section 2.3. For the dry peeling samples, the failure mode was cohesive in the sealant for all testing speeds. The fracture energy was similar for both the low modulus and the high modulus sealant when peeled under dry conditions as seen in Figure 5.1.

The wet peel samples failed both cohesively within the sealant and adhesively near the interphase depending on the peel rate. Adhesive failure only occurred when the

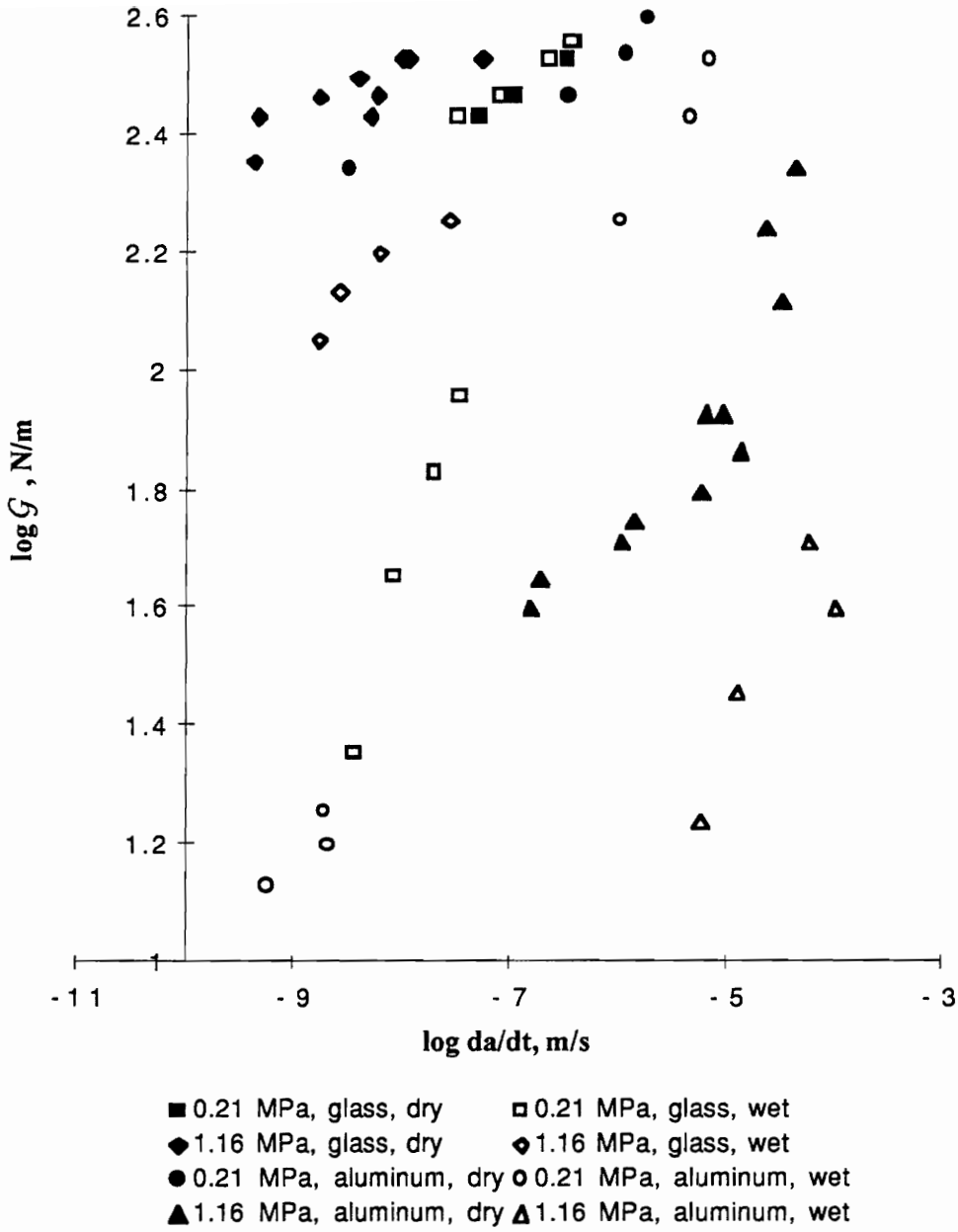


Figure 5.1 Log of fracture energy vs. log of peel rate for sealant on glass and aluminum.

peeling rate was less than 10^{-7} m/s. This suggests that a minimum amount of time was needed for the water to weaken the crack tip. This phenomenon was also observed by Schultz and Carré.² The high modulus sealant had a higher fracture energy than the low modulus sealant when failure was near the interphase. When failure was cohesive in the sealant, the two different sealants had similar fracture energies.

5.3.2 Fracture Energy of Sealant on Aluminum

The sealant displayed a wide range of fracture energy when peeled from the aluminum substrate as seen in Figure 5.1. The high modulus sealant failed very near the interphase for all the peeling rates measured both wet and dry. The cohesive strength of the high modulus sealant was evidently higher than the strength of the interphase between the aluminum oxide and the sealant. Therefore, failure occurred near the interphase even at high rates under dry conditions. The low modulus sealant failed cohesively in the sealant when peeled under dry conditions for all peeling rates. When the low modulus sealant was peeled under water, the failure mode was cohesive in the sealant for peel rates above 10^{-7} m/s. For peel rates below this speed, the low modulus sealant failed very near the interphase. The cohesive strength of the low modulus sealant was evidently higher than the interphase when the sealant was wet.

The rate of peeling determines the amount of time that the crack tip is exposed to water. The water may need a minimum amount of time to penetrate; otherwise, the crack tip behaves as if it is dry. Therefore, the failure mode is rate dependent. This conclusion

also agrees with the glass data which indicates the same failure mode rate dependence for the high and the low modulus sealant.

The fracture energy was very similar for all the sealants and substrate combinations when the failure mode was cohesive in the sealant. Cohesive failure does not distinguish between the two very different substrates and peeling conditions which is not a surprising conclusion.

5.4 Fracture Surface Analysis by ESCA

After peeling the sealant from the various substrates, the surfaces of the fracture were visually examined. If cohesive failure in the sealant was obvious, then no further analysis was necessary. If no trace of sealant was observed on the surface of the aluminum or glass, then the sample was analyzed with ESCA. For the ESCA analysis, two pieces of the sample were cut. One was tested immediately and the second was washed in hexane using an ultrasonic bath for 10 minutes to remove any silicone oil from the sample. Then the hexane washed sample was analyzed with ESCA.

5.4.1 Analysis of Glass Fracture Surface

The ESCA results are summarized in Table 5.2 for the glass peel specimens which were peeled under water only since no near interphase failure occurred for the dry samples. The important feature here was the presence of tin as mentioned above in section 5.2. No tin was detected on the surfaces which were not hexane washed at take-off angles of 15 or 45 degrees. This suggests that the silicone on this failure surface came

Table 5.2 ESCA analysis of glass fracture surfaces.

Electron	Glass surface after peeling in water with no hexane cleaning			Glass surface after peeling in water followed by hexane cleaning		
	Take-off Angle			Take-off Angle		
	15°	45°	90°	15°	45°	90°
C 1s	53.1	40.2	45.5	42.8	41.6	41.8
O 1s	25.8	30.5	28.9	21.8	31.8	30.7
Si 2p _{3/2}	18.3	21.9	22.2	32.8	24.9	25.6
Sn 3d _{5/2}	0.0	0.0	0.2	0.0	0.1	0.3
Na 1s	1.8	2.4	2.7	1.5	1.0	1.3
Au 4f _{7/2}	0.9	0.5	0.4	1.2	0.6	0.4

from the sealant and not from the glass. But, tin was observed on the glass when the take-off angle was 90 degrees. This suggests that the sealant layer is less than 5 nm thick otherwise the tin signal would not be detected at any take-off angle

ESCA results for the glass surface peeled then washed in hexane are also contained in Table 5.2. No tin was observed at a take-off angle of 15 degrees. The tin signal now shows up at both 45 degrees and 90 degrees. This suggests that the sealant layer is still present. But, some of the sealant was removed by the hexane wash. The fact that not all of the sealant was removed suggests that the sealant layer is chemisorbed to the surface not physisorbed.³

5.4.2 Analysis of Aluminum Fracture Surface

As seen in Table 5.3, all the fracture surfaces which visually appeared to be clean aluminum substrates contain silicon on the surface in significant amounts. The aluminum peel tests conducted under dry conditions did not indicate the presence of the aluminum alloy at the 15 degree take-off angle. The alloy signal was observed at the 45 degree take-off angle. This suggests that a thin layer of sealant was on the aluminum and can be no thicker than 5 nm. Otherwise, the alloy peak would be completely gone. Further, the oxide thickness was determined to be about 3 nm. Subtracting this from the previous estimate of the sealant thickness resulted in a layer which is less than 1 or 2 nm thick.

After washing the surface of the aluminum which was dry peeled, the alloy signal increased and the silicon signal was reduced. This suggests that some of the sealant was

Table 5.3 ESCA Analysis of Aluminum Fracture Surfaces

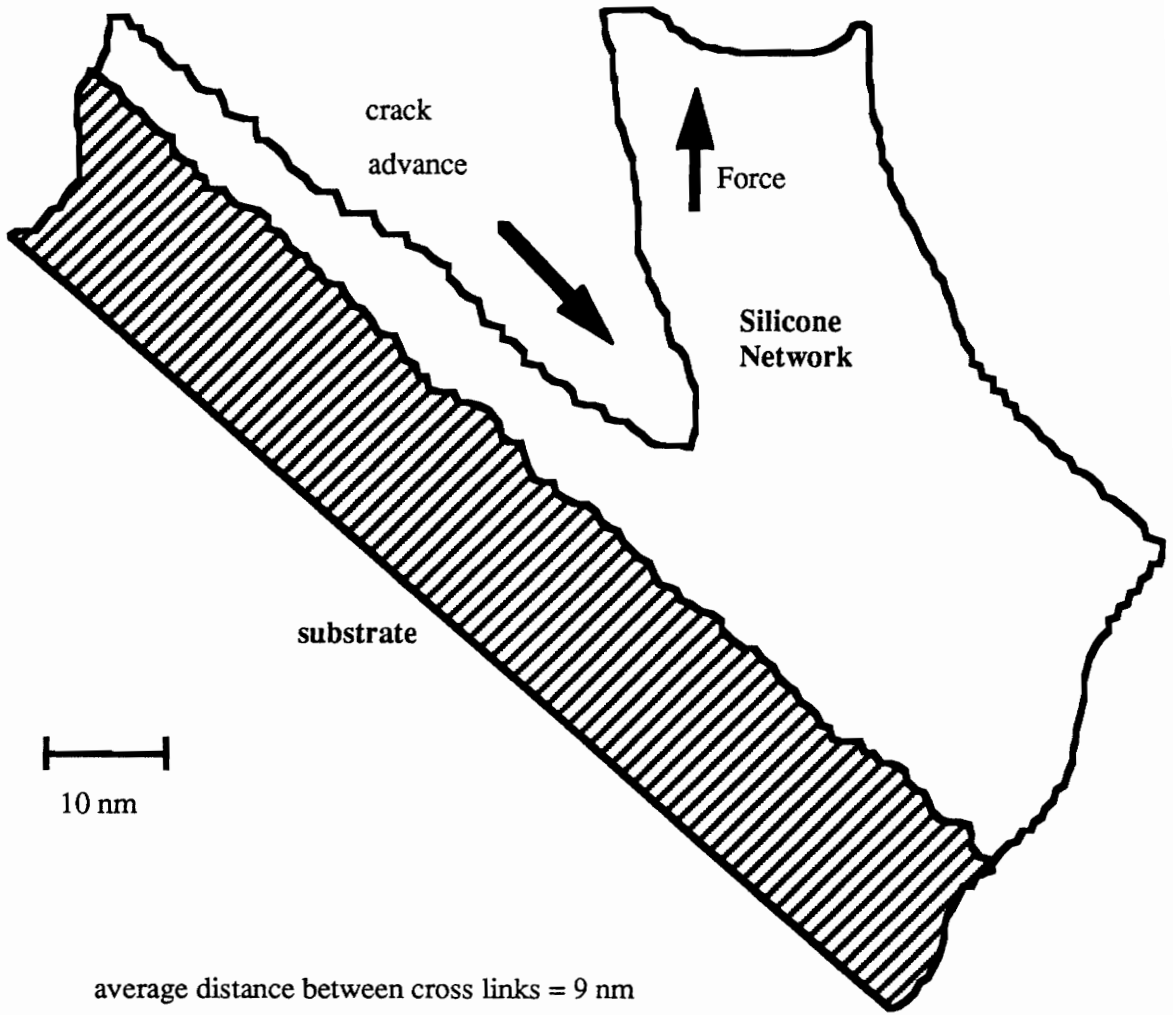
Electron	Aluminum surface after dry peeling with no hexane wash			Aluminum surface after dry peeling and washing with hexane.			Aluminum surface after peeling in water followed by hexane wash		
	Take-off Angle			Take-off Angle			Take-off Angle		
	15°	45°	90°	15°	45°	90°	15°	45°	90°
C 1s	51.8	50.4	46	60.7	56.7	57.1	50.1	47.6	35.6
O 1s	25.2	27.9	31.4	25.2	26.2	27.5	24.8	28.4	34.8
Si 2p _{3/2}	20.4	17.1	13.3	9.3	9.0	9.0	18.3	13.2	11.3
N 1s	1.2	1.3	2.0	1.0	2.0	1.3	1.2	1.9	1.5
Au 4f _{7/2}	0.0	0.0	0.0	0.0	0.0	0.0	1.2	1.2	1.4
Al 2p _{3/2}									
oxide	1.4	2.3	4.9	3.8	5.0	4.5	3.7	5.9	9.9
alloy	0.0	1.0	2.5	0.0	0.8	1.0	0.7	1.8	5.6
oxide									
thickness,									
nm	N/A	2.4	3.2	N/A	3.8	4.6	1.4	2.9	3.0

removed. However, significant levels of sealant were still on the surface of the aluminum even after hexane washing. This suggests some form of primary bonding has occurred between the sealant and the aluminum oxide.

The fracture surface of aluminum after peeling under water and followed by a hexane wash yielded a similar level of sealant. However, the aluminum alloy peak was present even at the 15 degree take off angle. This suggests that the sealant thickness is lower than on the other aluminum peel specimens analyzed. It is suggested that the apparent contradiction can be explained by the formation of a rather rough or patchy sealant layer. The ESCA analysis is an average of the sample surface comprising a circle 100 microns in diameter. Therefore, ESCA does not resolve surface topology information on a scale smaller than this size.

5.5 Model of Fracture Surface

From the visual and ESCA analysis of the fracture surfaces, the following model of the fracture is proposed in Figure 5.3. It should be noted that the above model suggests the formation of a smooth layer of polymer on the surface of the substrate for instances of near interfacial failure. This is most likely erroneous by indirect observations. First, it is noted that the level of sealant on the surface of the aluminum increased even when the aluminum alloy appeared closer to the surface of the fracture. Secondly, the average end to end distance between polymer cross-links is about 9 nm. For a film to exist which is less than this thickness, polymer cross-links will need to be



average distance between cross links = 9 nm

calculated using characteristic ratio = 5.2

Figure 5.3 Model of peel failure occurring near the interphase in the sealant/aluminum specimen.

broken. Such a result would lead to a much higher fracture energy than was measured.

The fracture energy would need to be similar to the fracture energy of bulk sealant. If the failure mode was mixed with some percentage of the surface being cohesive in the sealant, and some portion being interfacial at the oxide surface then the above data would not be contradictory. It is proposed that the layer of sealant left on the surface is rough and parts of the surface may be only aluminum oxide and other parts may be patches of sealant greater than 4 nm thick.

5.6 Summary

The fracture energy of sealant on glass and aluminum was studied for a high modulus sealant and a low modulus sealant under wet and dry conditions. The high modulus sealant yielded cohesive failure on glass when peeled under dry conditions or when peeled under wet conditions at a peel rate above 10^{-7} m/s. The high modulus sealant failed very near the interphase for the aluminum substrate under all peel conditions. The low modulus sealant failed cohesively on glass or aluminum when peeled under dry conditions. The low modulus sealant failed very near the interphase on glass or aluminum when the peeling rate was less than 10^{-7} m/s.

In general the sealant had better adhesion to the glass than to the aluminum. The lower modulus sealant failed with cohesive failure in the sealant more frequently than the high modulus sealant.

When the failure was cohesive in the sealant, the fracture energy was very similar

for all sealants and substrate conditions.

Visual observation of failure at the aluminum or glass surface can lead to erroneous conclusions. In all cases of visually interfacial failure, ESCA analysis indicated the presence of sealant on the surface. The level of sealant on the surface after peeling was reduced by hexane washing but not eliminated. This suggests that the sealant may be chemically bound to the surface of the glass or aluminum.

5.7 References

- ¹ A. N. Gent and S. Y. Kaang, *J. Adhesion*, **24**, 173 (1987)
- ² A. Carré and J. Schultz, *Journal of Adhesion*, **18**, 171 (1984).
- ³ H. F. Webster and J. P. Wightman, *Langmuir*, **7**, 3099 (1991)

VI. Results and Discussion:

Effect of Surface Contamination and Roughness on 45° Peel Adhesion of Silicone Sealant to Stainless Steel under Dry and Wet Conditions

In the previous chapter, it was shown that fracture which appears interfacial by visual observation can still contain significant amounts of silicone on the surface of the substrate as measured by electron spectroscopy for chemical analysis (ESCA). However, ESCA obtains data over a relatively large surface area and averages the results. Very small scale changes in the surface, i.e., patchiness in the atomic concentration can not be resolved using ESCA. Therefore, the topology of the silicone on the surface was not determined. In this chapter, ESCA results are combined with atomic force microscopy (AFM) to resolve the atomic concentration and changes in roughness on the nm scale. Relatively smooth well characterized stainless steel surfaces were used.

The fracture energy between stainless steel and polydimethylsiloxane (PDMS) sealant was measured using a 45° peel test under dry and wet conditions. Different surface treatments were done in order to produce different levels of contamination and roughness. A silicone sealant was used to probe the fracture energy at the surface of the steel substrate. After peeling the samples, the steel substrates were analyzed using ESCA and AFM in order to provide chemical and topographical information of the failure surface. The fracture energy was related to the level of contamination and roughness on the surface of the stainless steel.

6.1 Initial Surface Analysis

The surface of the stainless steel was analyzed with ESCA and AFM techniques to develop a base line for later comparison to the fracture surfaces. All measurements were conducted within 15 minutes after surface treatment.

6.1.1 Stainless Steel Surface

6.1.1.1 ESCA Analysis

The ESCA analysis of the steel samples, given in Table 6.1, indicated the presence of significant amounts of carbon, oxygen, chromium, iron, and nickel. Carbon came from the organic contaminant layer and was significantly reduced by the argon plasma treatment as seen in Figure 6.1. The small difference found between the "Bright Anneal" and the "Mirror Finish" sample can be due to the roughness that possibly affected the adsorption of contamination. Oxygen came mainly from the oxide/hydroxide passive layer on the steel and has also associated with carbon in the organic contaminant layer for the water rinsed samples.¹ Chromium and iron were combined with oxygen in the passive film and also came from the metal underneath for the argon plasma treated samples. The "Bright Anneal" lead to an enrichment in chromium in the passive film compared to the polished sample. Nickel came from the metal as this element is usually not present in the passive film.

6.1.1.2 AFM Images

Surface images for the "Mirror Finish" surface were obtained with the AFM for

Table 6.1 Surface composition of "bright anneal" and "mirror finish" stainless steel for different cleaning treatments.

Surf. treatment Clean. treatment	304 B.A.		304 M.F.	
	water rinse	plasma	water rinse	plasma
C % at	68.0	18.5	85.5	28.5
O % at	25.0	56.0	13.0	52.5
Cr % at	3.0	8.5	0.5	3.0
Fe % at	4.0	16.5	1.0	15.5
Ni % at	nd ^a	0.5	nd ^a	0.5
d _c (nm)	3.0	0.8	4.0	1.1

^and = none detected.

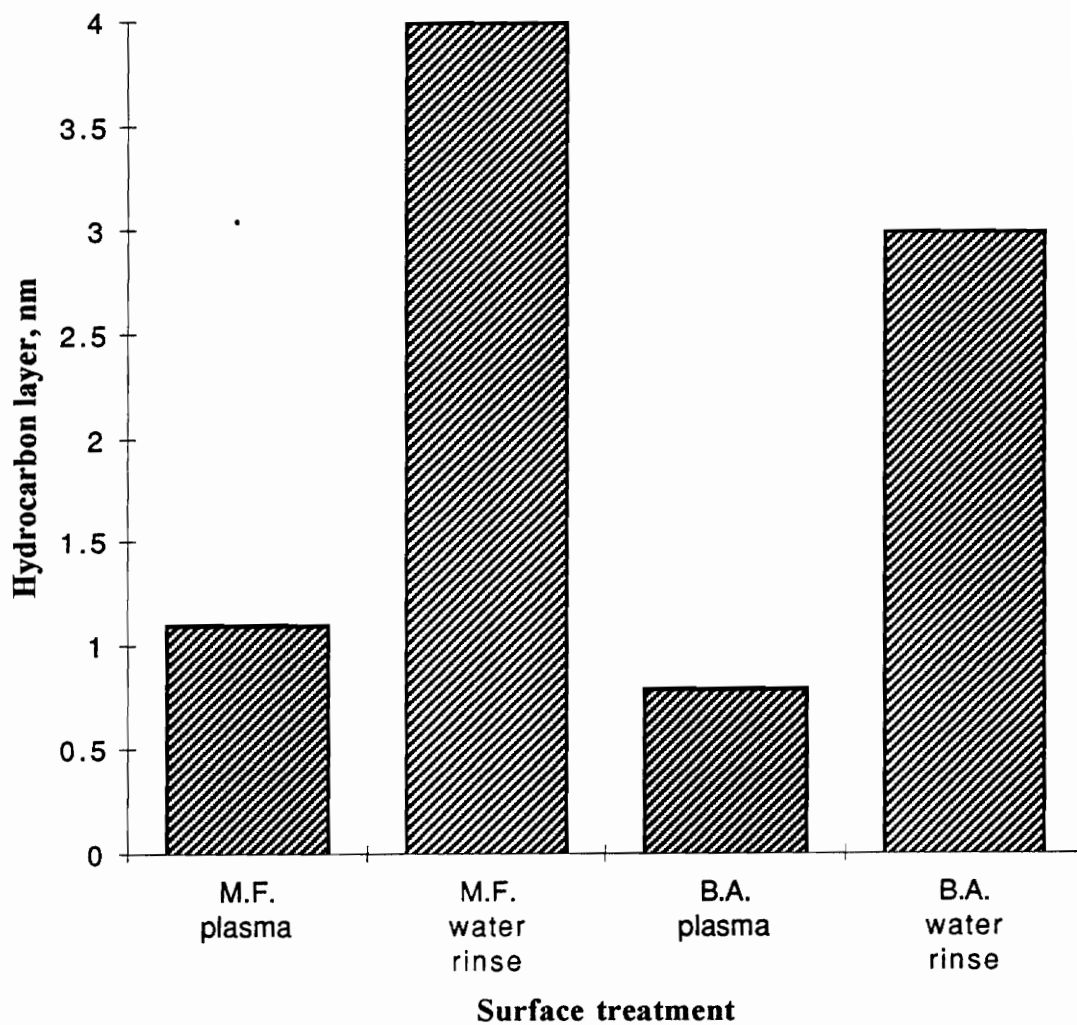


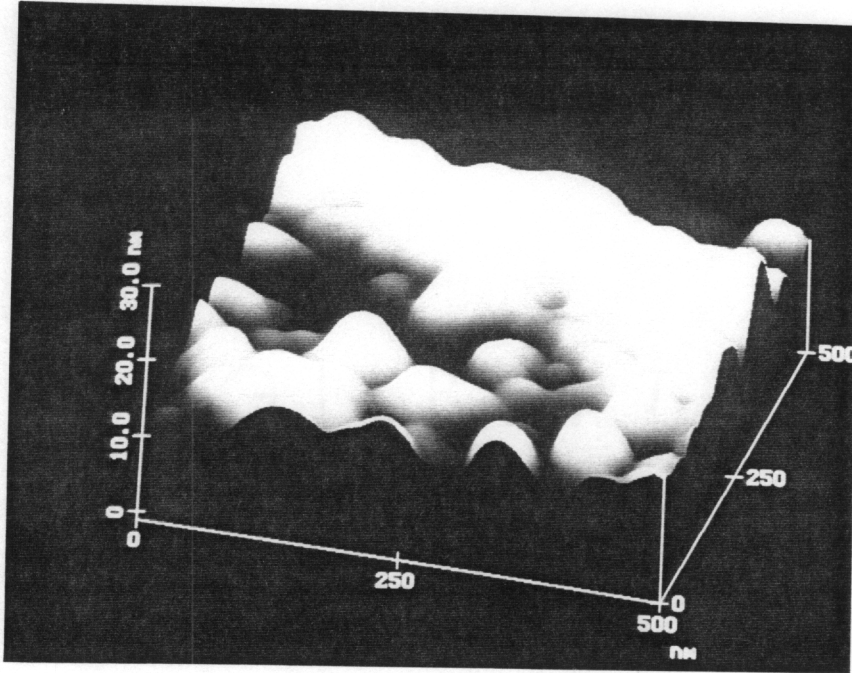
Figure 6.1 Organic contaminant layer thickness (nm) for different surface treatments.

the water rinsed and argon plasma treated samples and compared in Figure 6.2. For both surfaces, several images were recorded at different locations in order to verify the reproducibility of the observed features. The only difference between the water rinsed and argon plasma treated samples was the elimination of the hydrocarbon contamination; therefore, it is suggested that the bumps of the water rinsed surface are due to the hydrocarbon contamination. A profile analysis indicated that the bumps have a height around 10 nm and a diameter around 100 nm. In order to characterize the patchiness of that contamination, the average difference in height (R_z) between the five highest peaks and five lowest valleys relative to the mean plane and the mean surface roughness (R_a) relative to the center plane were determined. Values of R_a were calculated using equation 6.1,

$$R_a = \frac{1}{L_x \cdot L_y} \int_0^{L_y} \int_0^{L_x} |f(x,y)| dx dy \quad (6.1)$$

where $f(x,y)$ is the profile of the surface relative to the center plane and L_x and L_y are the dimensions of the surface .

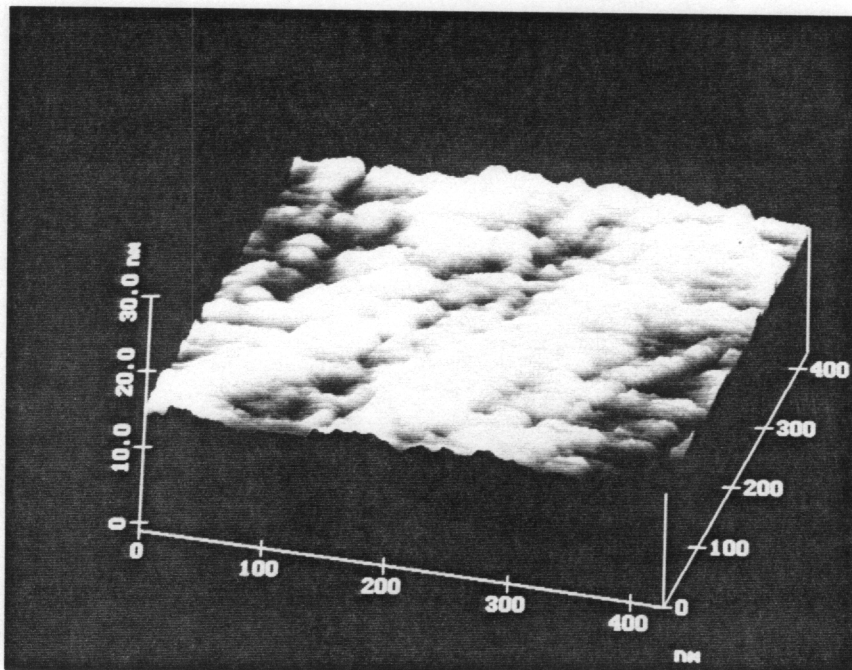
An R_a value of 3.3 nm was obtained for the "water" surface and an R_a value of 0.75 nm for the argon plasma treated surface, corresponding to the smoothest surface studied. Assuming that the contamination is not covering all the surface, i.e., the deepest profile points belong to the oxide surface, the mean value R_a can be taken as the mean thickness of the contamination layer. The values of 4 nm and 1.1 nm for contamination



**Water
Rinsed**

$R_a \approx 3.3 \text{ nm}$

$R_z \approx 11.2 \text{ nm}$



**Argon
Plasma**

$R_a \approx 0.75 \text{ nm}$

$R_z \approx 1.1 \text{ nm}$

Figure 6.2. AFM images for the water rinsed and argon plasma cleaned "Mirror Finish" samples.

thickness shown in Table 6.1 from ESCA measurements are in good agreement with the AFM results. This agreement also supports the suggestion that AFM images of the surface detect the organic contamination.

In Figure 6.3, the "Bright Anneal" stainless steel surface exhibits a much higher roughness. This highly oriented roughness results from the cold rolling process. In this case, it is impossible to observe the contamination. Therefore, AFM was not conducted on the argon plasma cleaned "Bright Anneal" stainless steel surface. On the other hand, the surface energy of the "Bright Anneal" sample was measured in previous work and values of 39 and 98 mJ/m² were found respectively for the water rinsed and argon plasma treated surfaces.¹ The higher surface energy value was obtained with the argon plasma treatment primarily due to an increase in the polar component.

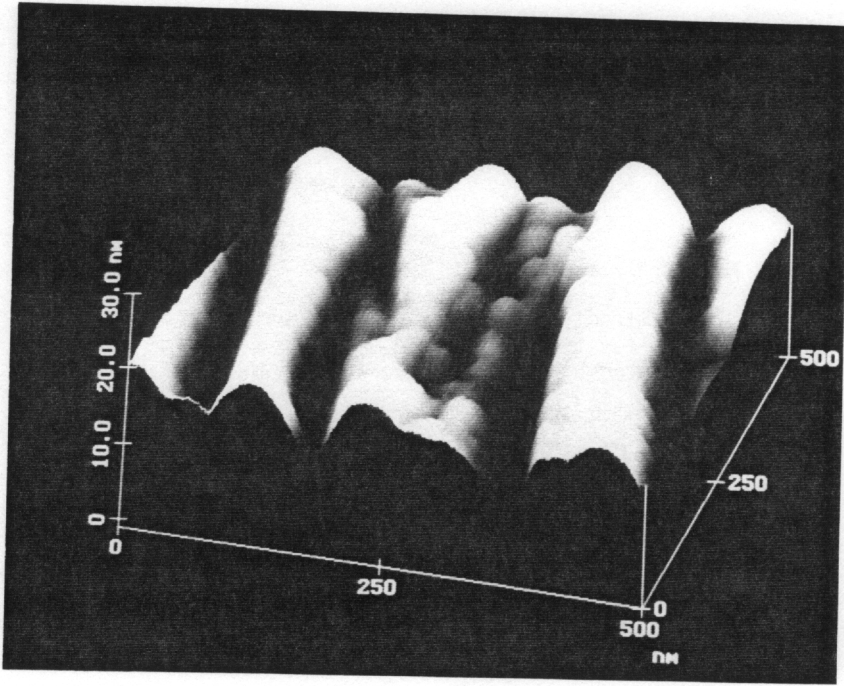
6.1.2 Silicone Surface

6.1.2.1 ESCA Analysis

The theoretical chemical composition of the sealant was compared to the measured chemical composition from ESCA data in Table 6.2. The silicone surface was measured after curing in air for two weeks. The experimental values are in good agreement with the predicted composition. However, a slight increase in carbon concentration was measured.

6.1.2.2 AFM Images

Attempts to analyze the surface of the silicone with atomic force microscopy



**Water
Rinsed**

$R_a \approx 5.3 \text{ nm}$

$R_z \approx 17.0 \text{ nm}$

Figure 6.3 AFM image for the "Bright Anneal" stainless steel sample after the water rinsing.

Table 6.2 Atomic composition of cured sealant.

Element	C% at	O% at	Si% at
Calculated	50.0	25.0	25.0
Measured	50.8	25.0	24.2

were unsuccessful using the contact mode. Only fuzzy images were obtained. Better results might be obtained with a non-contact mode AFM; but, these studies were not conducted.

6.2 Adhesive Strength

The adhesive strength of the sealant on the various stainless steel surfaces was measured using the 45° peel test as outlined in section 3.5.2. The fracture energy was measured over several decades of crack speed. The specimens were tested in either ambient air or while submersed in deionized water at ambient temperature .

A plot of the logarithm of the fracture energy vs. the logarithm of the crack growth rate for all the substrates can be found in Figure 6.4. One curve was included for bulk fracture data obtained by measuring the peel strength of the sealant to a cleaned glass substrate; 100% cohesive failure in the center of the sealant occurred for this condition. The shapes of the curves are in good agreement with viscoelastic theory.² A quadratic equation was used to obtain good fits to the data shown in Figure 6.4. Only changes in the constant c_1 were used to account for changes in the vertical displacement between fracture energy measured on different surfaces. The regression data can be found in Table 6.3. The slopes represent the time dependent portion of the fracture energy. The fact that the slopes are basically the same indicates that equation 2.3 may be used. A plot of the log of the fracture energy vs. the log of the crack speed after vertical shifting of the

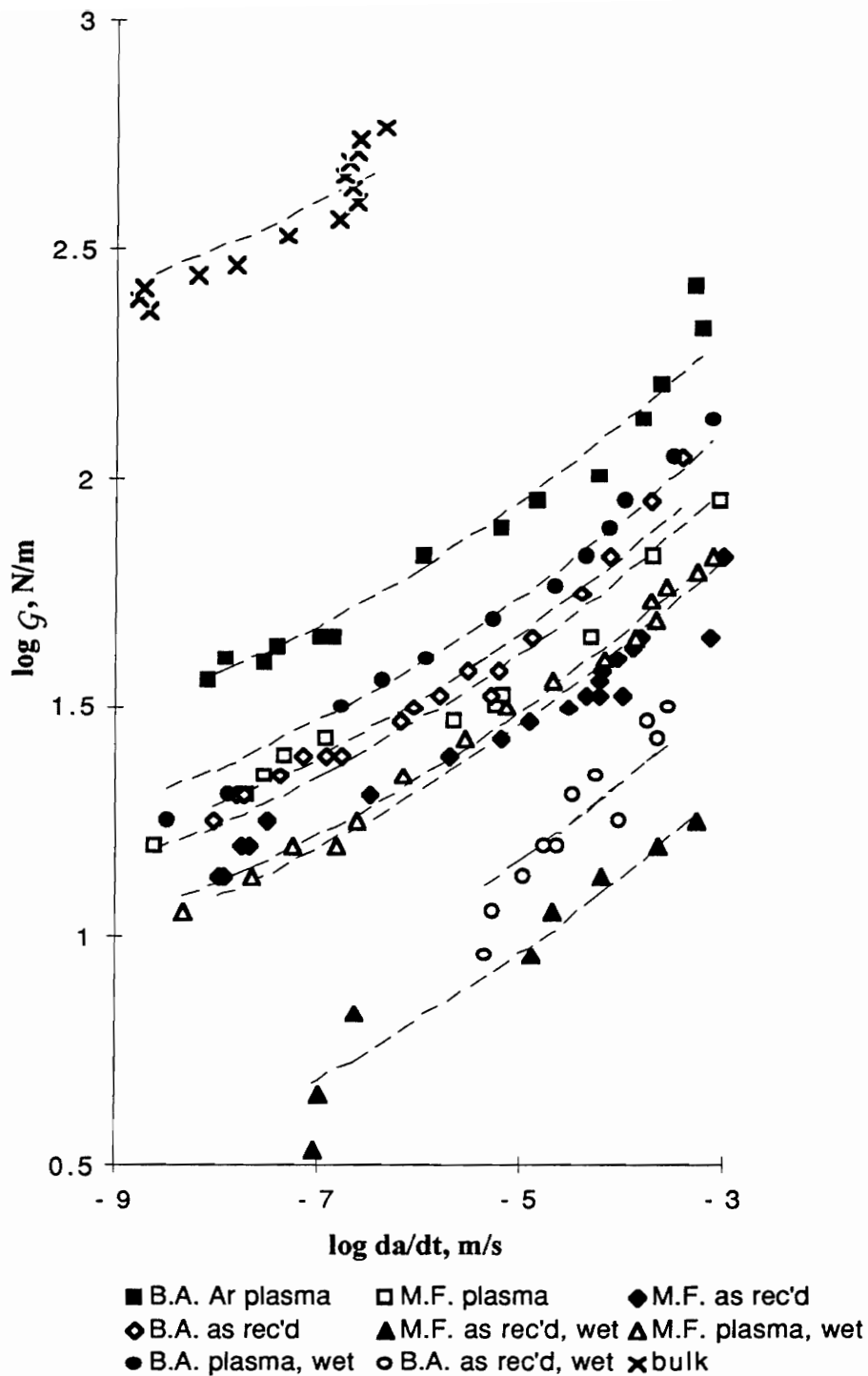


Figure 6. 4 Fracture energy G (N/m) as a function of the peeling rate for all samples.

Table 6.3 Regression analysis for fracture energy curves in Figure 6.4.

Surface/peel condition	vertical shift in log fracture energy vs. log da/dt			
	vertical shift	root mean squared error	95% confidence limit	
			lower	upper
M.F. plasma, dry peel	0.000	0.059	-0.178	0.178
B.A. plasma, dry peel	-0.334	0.053	-0.493	-0.175
M.F. water rinse, dry peel	0.153	0.062	-0.033	0.339
B.A. water rinse, dry peel	-0.045	0.053	-0.204	0.113
M.F. water rinse, wet peel	0.660	0.069	0.452	0.867
M.F. plasma, wet peel	0.125	0.024	0.053	0.197
B.A. plasma, wet peel	-0.125	0.073	-0.343	0.094
B.A. water rinse, wet peel	0.450	0.073	0.232	0.668
bulk, dry peel	-1.260	0.057	-1.431	-1.089

Surface/peel condition	relative threshold fracture energy			
	relative threshold fracture energy	root mean squared error	95% confidence limit	
			lower	upper
M.F. plasma, dry peel	1.000	0.872	1.508	0.663
B.A. plasma, dry peel	2.157	0.885	3.109	1.497
M.F. water rinse, dry peel	0.703	0.867	1.079	0.458
B.A. water rinse, dry peel	1.110	0.886	1.598	0.772
M.F. water rinse, wet peel	0.219	0.853	0.353	0.136
M.F. plasma, wet peel	0.750	0.947	0.884	0.636
B.A. plasma, wet peel	1.333	0.846	2.202	0.806
B.A. water rinse, wet peel	0.355	0.846	0.586	0.215
bulk, dry peel	18.182	0.877	26.950	12.266

	c1	c2	c3
coefficients of quadratic equation	2.69456	0.27159	0.01123

curves is found in Figure 6.5. The goodness of fit indicates that the rate dependent portion of the fracture energy is nearly equivalent for all the surfaces tested. The relative vertical displacements quantified in Table 6.3 represent differences in the threshold fracture energy, G_0 . The relative G_0 was plotted with respect to the surface treatment and peel. Figure 6.6a contains relative G_0 including data for the bulk fracture. The bulk fracture energy is about 20 times that of the rest of the conditions all of which underwent failure near the interface of the steel. To facilitate comparison of the various steel surfaces, Figure 6.6b contains the same data as 6.6a without the bulk data. The data indicates significant differences for the various steel surfaces and peeling conditions. The largest relative G_0 was obtained for the plasma cleaned Bright Anneal steel peeled under dry conditions. The plasma cleaned Bright Anneal surface had the lowest level of contamination and highest surface roughness. The lowest relative G_0 was the Mirror Finish water rinsed and peeled under wet conditions. The Mirror Finish water rinsed surface had the highest level of contamination and smoothest oxide layer.

6.3 Analysis of Fracture Surfaces

After peeling the sealant from the steel substrates, visual examination suggested interfacial failure occurred. No trace of silicone could be seen on the surface of the steel. This observation suggests that any silicone on the surface must be less than a micron thick.

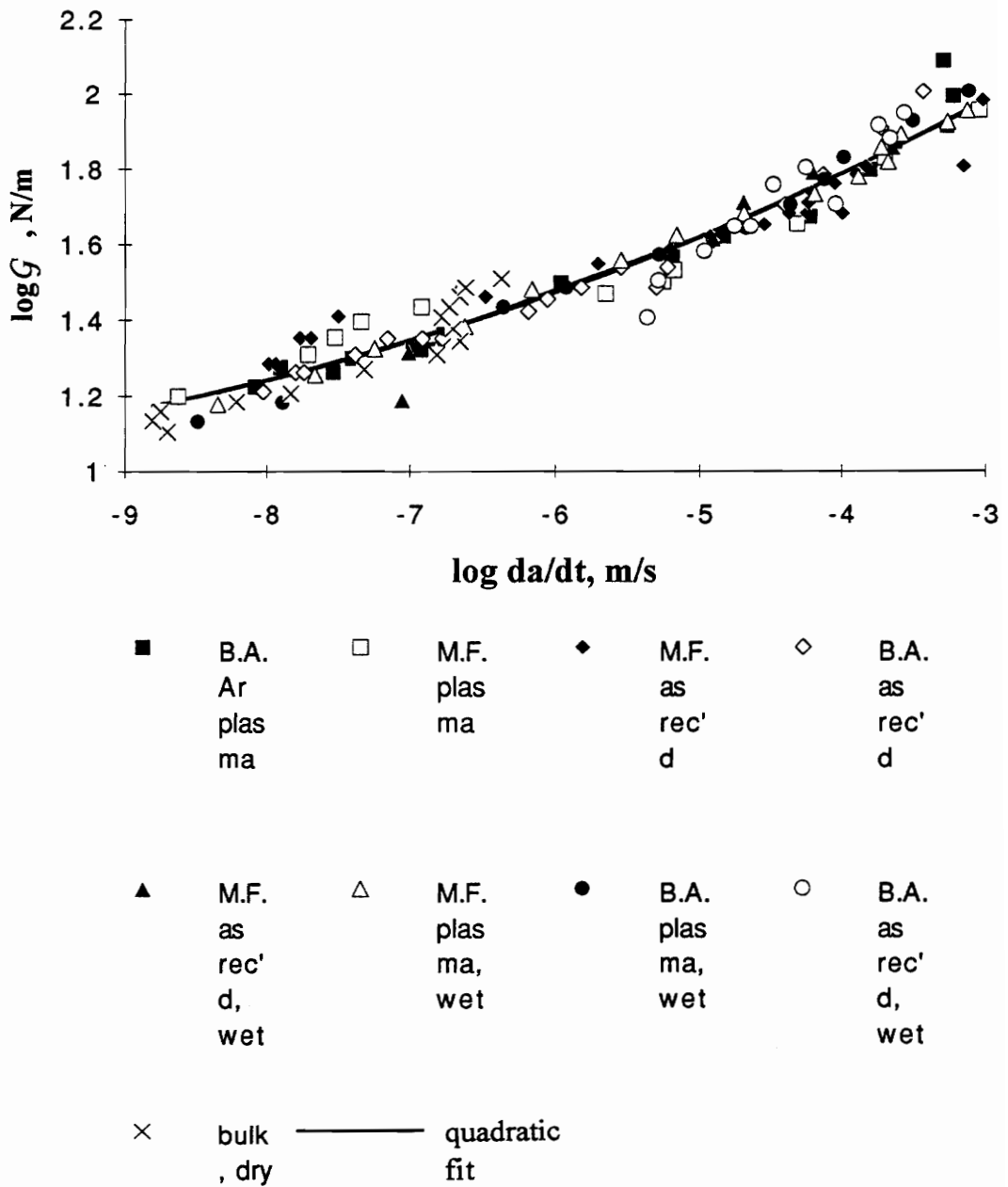
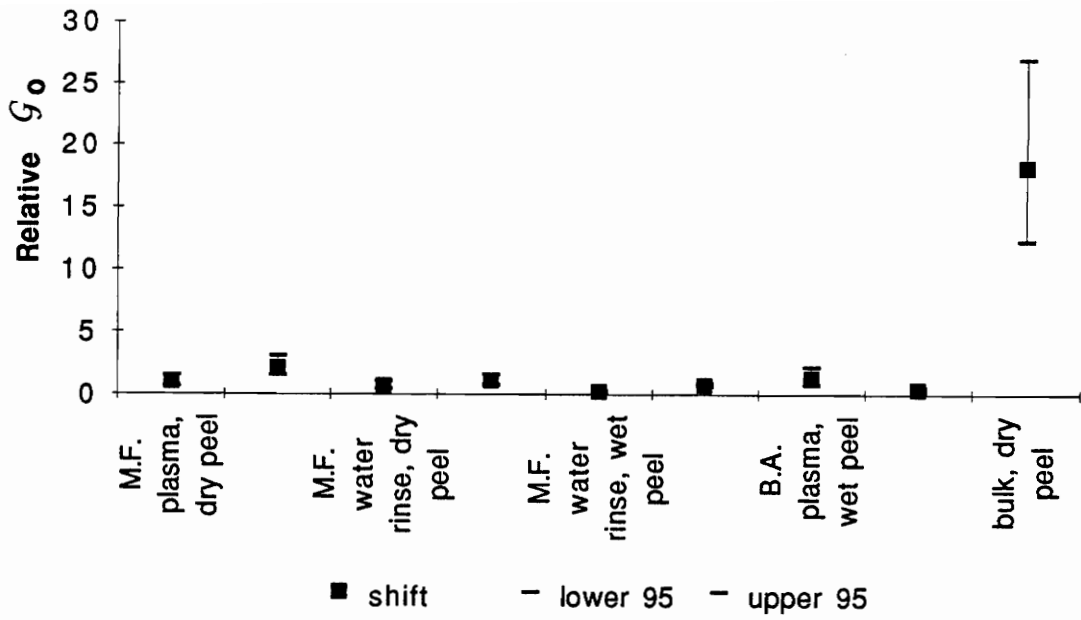
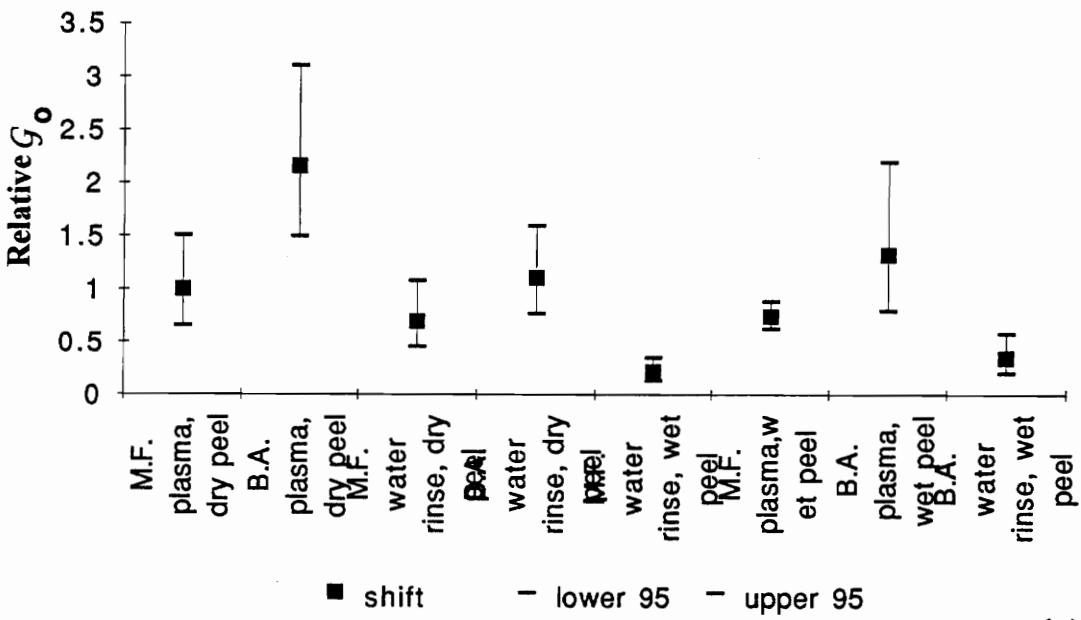


Figure 6.5 Fracture energy vs. crack rate after vertical shifting to determine relative vertical displacements.



a.)



b.)

Figure 6.6 a) Relative G_0 vs. surface treatment and peeling condition. b) Bulk data not included.

6.3.1 Stainless Steel Surface

6.3.1.1 ESCA Analysis

The ESCA analysis of the steel samples after peeling in air and in water are given in Tables 6.4 and 6.5 respectively. The observation of significant amounts of silicon was due to the presence of silicone on the metal substrates although the sealant appeared visually to have pulled away from the stainless steel surface. The steel surfaces were analyzed after cleaning with hexane in an ultrasonic bath. Significant amounts of silicone was still present on the steel after washing with hexane. As hexane is a good solvent for the polymer, the amount of silicon measured on the surface after such a cleaning indicates that molecules of the PDMS were chemisorbed on the surface.³

After peeling the samples under water, some zinc was measured on steel surface. This is due to contamination attributed to the resistance heater which was submerged in the deionized water. The surface of the heater was galvanized. In all cases, the silicone level was reduced when the peel test was conducted under water immersion as compared to dry peel testing.

6.3.1.2 AFM Images

The AFM images of the steel substrates after peel testing in air with no hexane wash are shown in Figure 6.7 for the "Mirror Finish" sample and in Figure 6.8 for the "Bright Anneal" sample. For the "Mirror Finish" sample an increase of the roughness (0.75 nm vs. 2.5 nm for the argon plasma treated surface) was observed after the peeling

Table 6.4 Surface composition of the interface failure of the stainless steel substrate after peeling in air and values of the PDMS layer thickness (d_{PDMS}).

Surf. treatment	304 B.A.				304 M.F.			
Clean.	water rinse		argon plasma		water rinse		argon plasma	
hexane wash	before	after	before	after	before	after	before	after
C % at	46.0	54.5	41.5	42.0	62.0	62.0	38.0	37.5
O % at	36.0	35.5	37.5	38.0	28.0	30.0	43.0	45.5
Cr % at	2.0	4.0	2.0	1.5	0.5	0.5	1.5	1.5
Fe % at	2.0	5.0	3.0	2.5	1.5	2.5	6.0	5.0
Si % at	14.0	1.0	16.0	15.5	8.0	5.0	11.5	10.5
d_{PDMS} (nm)	2.2	0.17	2.6	2.5	1.2	0.8	1.8	1.6

Table 6.5 Surface composition of the interface failure of the stainless steel substrate after peeling in water and values of the PDMS layer thickness (d_{PDMS}).

Surf. treatment	304 B.A.				304 M.F.			
	water rinse		argon plasma		water rinse		argon plasma	
hexane wash	before	after	before	after	before	after	before	after
C % at	36	39	41	37.5	60	51	37.5	36.5
O % at	50.5	49	43	49	31	38.5	43.5	45.5
Cr % at	nd ^a	nd ^a	nd ^a	nd ^a	1	2	0.5	1
Fe % at	nd ^a	nd ^a	nd ^a	nd ^a	2	3	2.5	3
Si % at	5	1	8.5	4.5	5	3	11.5	9
Zn % at	8.5	10	7.5	9	1	2.5	4.5	5
d_{PDMS} (nm)	0.80	0.17	1.3	0.7	0.80	0.50	1.8	1.4

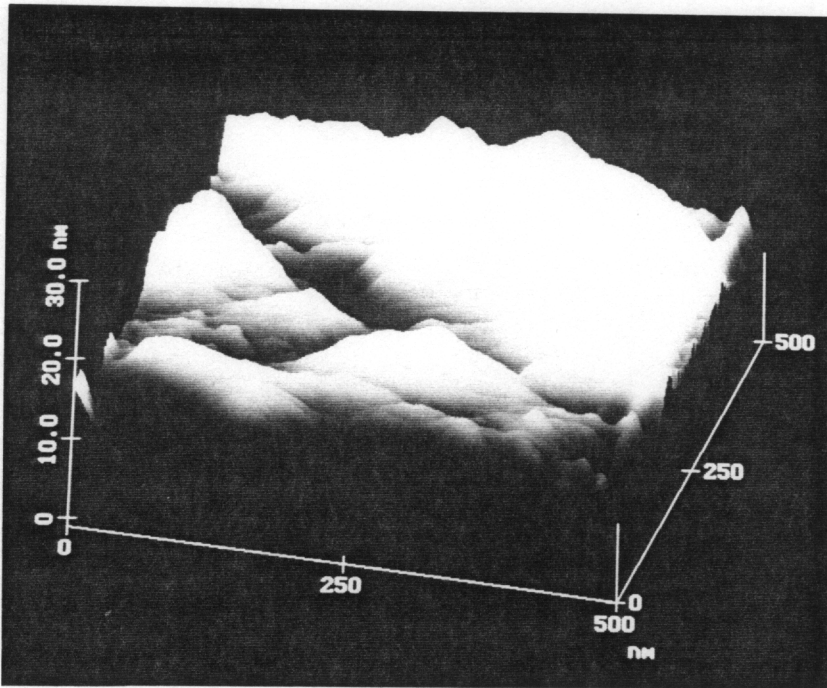
^and = none detected

and large strips are seen in the surface. These large strips can be attributed to the sealant as shown by the silicone content measured with ESCA and found in column 9 of Table 6.4. Although more silicon was found on the argon plasma cleaned surface than the water rinsed surface, the roughness on the water rinsed surface was larger possibly due to the contaminant layer thickness. ESCA results given in Table 6.5 indicated that much more carbon is found on the delaminated water rinsed surface than the cleaned surface although the estimated layer of PDMS is thinner on the non-cleaned surface. The fracture surfaces were protected from airborne contamination by placing them in a small sample container during the transfer to the ESCA instrument. Therefore, the hydrocarbon contamination can most likely be attributed to the original contamination on the stainless steel before the sealant was applied. This result suggests that the contamination was still present after peeling the sealant from the metal substrate.

The "Bright Anneal" sample that exhibited a rougher surface (see Figure 6.3) shows a very different failure surface. After peel testing, the roughness decreased and the images of Figure 6.8 suggest that the polymer has filled the "valleys" of the substrate seen in Figure 6.3.

6.3.2 ESCA of Silicone Surface

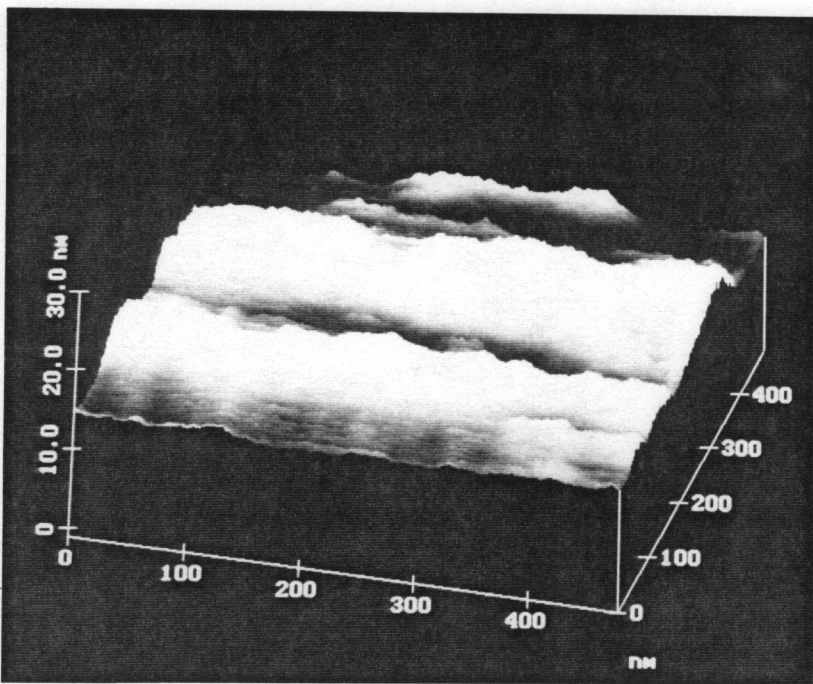
After peeling the sealant from the steel, the PDMS surface which was in contact with the steel was analyzed with ESCA. The ESCA analysis of all delaminated PDMS



**Water
Rinsed**

$R_a \approx 5.8 \text{ nm}$

$R_z \approx 9.2 \text{ nm}$

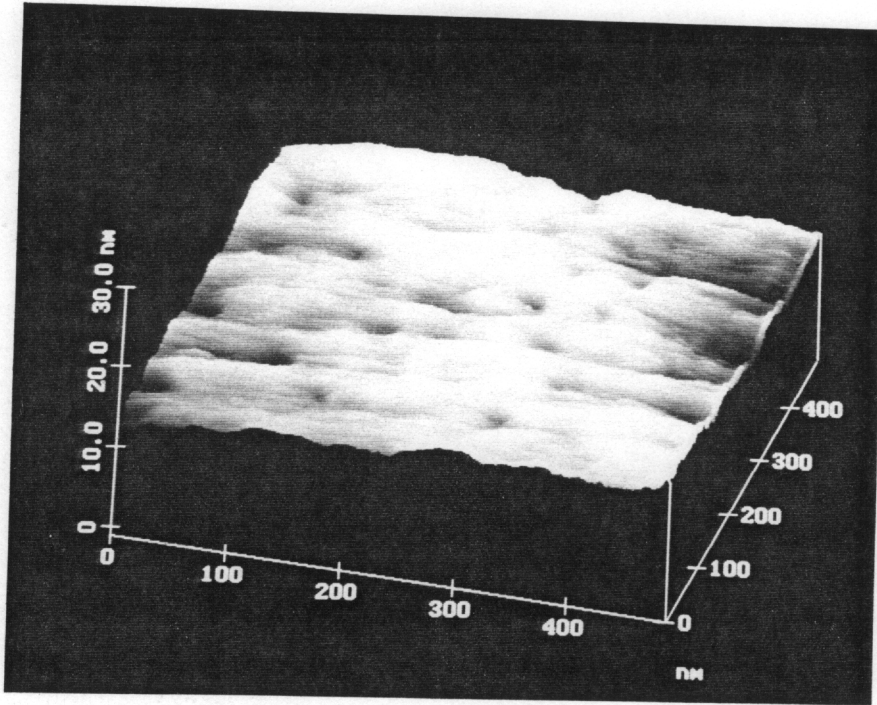


**Argon
Plasma**

$R_a \approx 2.5 \text{ nm}$

$R_z \approx 6.0 \text{ nm}$

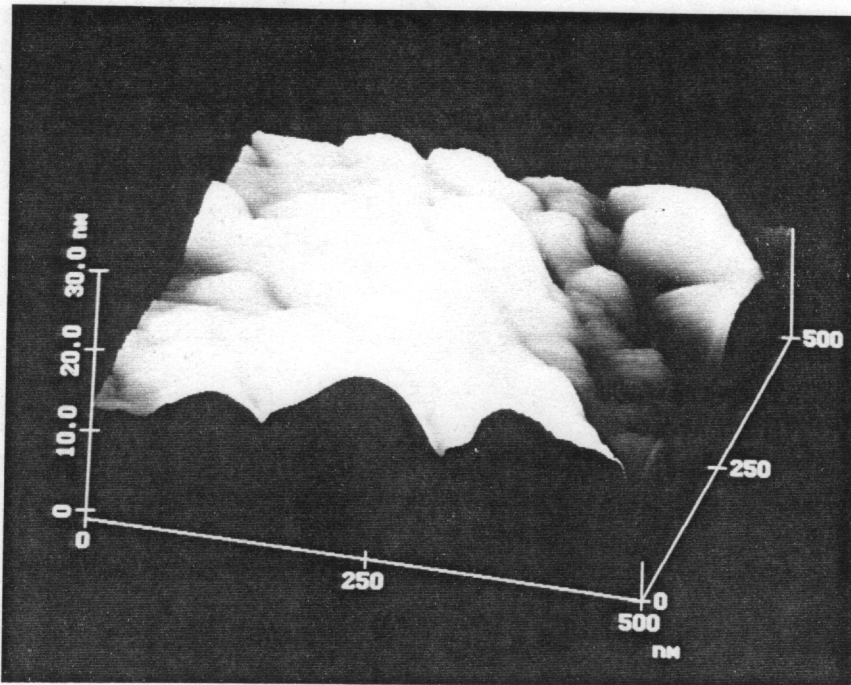
Figure 6.7 AFM images for the water rinsed and argon plasma cleaned "Mirror Finish" samples.



**Water
Rinsed**

$R_a \approx 1.0 \text{ nm}$

$R_z \approx 3.8 \text{ nm}$



**Argon
Plasma**

$R_a \approx 0.7 \text{ nm}$

$R_z \approx 2.5 \text{ nm}$

Figure 6.8 AFM images for the water rinsed and argon plasma cleaned "Bright Anneal" stainless steel sample after peeling in air.

samples showed no significant difference in atomic concentration. From the ESCA standpoint, they are all very pure PDMS surfaces with no significant variations from what is expected for bulk PDMS. However, the ESCA does not have the resolution necessary to distinguish between cross-linker resin and cured polymer. Therefore, migration of cross-linker to the interphase may occur but cannot be detected.

6.3.3 Contamination

The relative change in threshold fracture energy is plotted in Figure 6.9 as a function of the contaminant layer thickness measured with ESCA before bonding the steel substrates with the silicone elastomer. AFM images showed that contamination is patchy, but average thickness values of the carbon contamination was used to simplify discussion. For all the samples, contamination resulted in a lower fracture energy. This result can be understood from the different analyses of the substrate before and after peeling. First, it was shown that the silicone adhesive used did not displace the organic contamination present on the substrate before bonding. As the surface energy was strongly reduced by this contamination, it will be difficult for the adhesive to achieve complete surface wetting. Another point concerns the ESCA analysis of the delaminated surfaces after a cleaning in hexane. The contaminant layer inhibited primary bonding (ionic or covalent) between the silanol terminated polymer chain and the oxide/hydroxide metal surface. This intervening layer eliminated the possibility for developing the maximum attractive forces between the oxide and the adhesive and only weak boundary layer failure

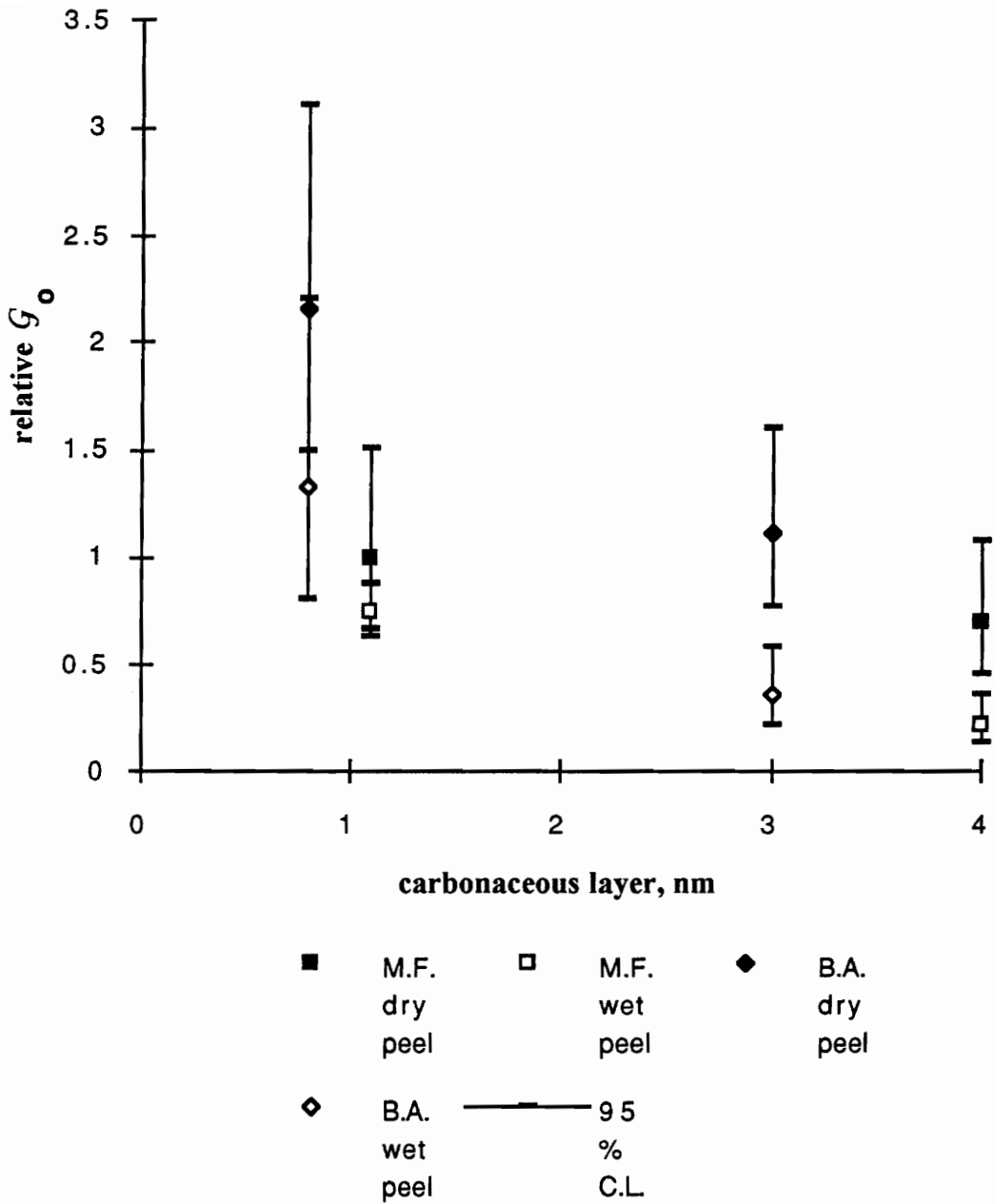


Figure 6.9. Relative vertical shift in threshold fracture energy as a function of carbonaceous layer contamination thickness.

sites will result if adhesive detachment is attempted in the presence of such contaminated layers.

The percentage of silicone removed on the substrates by hexane cleaning is given in Figure 6.10 as a function of the thickness of the carbonaceous contamination layer. The amount of PDMS that remained on the steel surfaces after peel testing was easier to remove when the contamination was present meaning that the carbonaceous layer inhibited strong bonding between the oxide and the sealant. This resulted is strong evidence that the silicone cannot displace the carbonaceous layer from the surface of the stainless steel.

6.3.4 Roughness

For all the dry peeled specimens, more silicon (see Table 6.4) was measured on the surface of the rougher sample (Bright Anneal compared to Mirror Finish) after peeling. The Bright Anneal AFM images in Figure 6.3 and 6.8 suggest that the fracture occurred above the roughness; and that the roughness can prevent the polymer from being totally peeled out from the substrate. As a result, a higher fracture energy was measured on the Bright Anneal. The decrease in the adhesive bonding seen in Fig. 6.9 due to the contamination is more pronounced for the rougher (Bright Anneal) than the smoother (Mirror Finishing) substrate. The positive influence of the roughness was decreased when contamination was present on the surface. In columns 2 and 3 of Table 6.4, a strong decrease in the silicon content after hexane cleaning is observed for the Bright Anneal

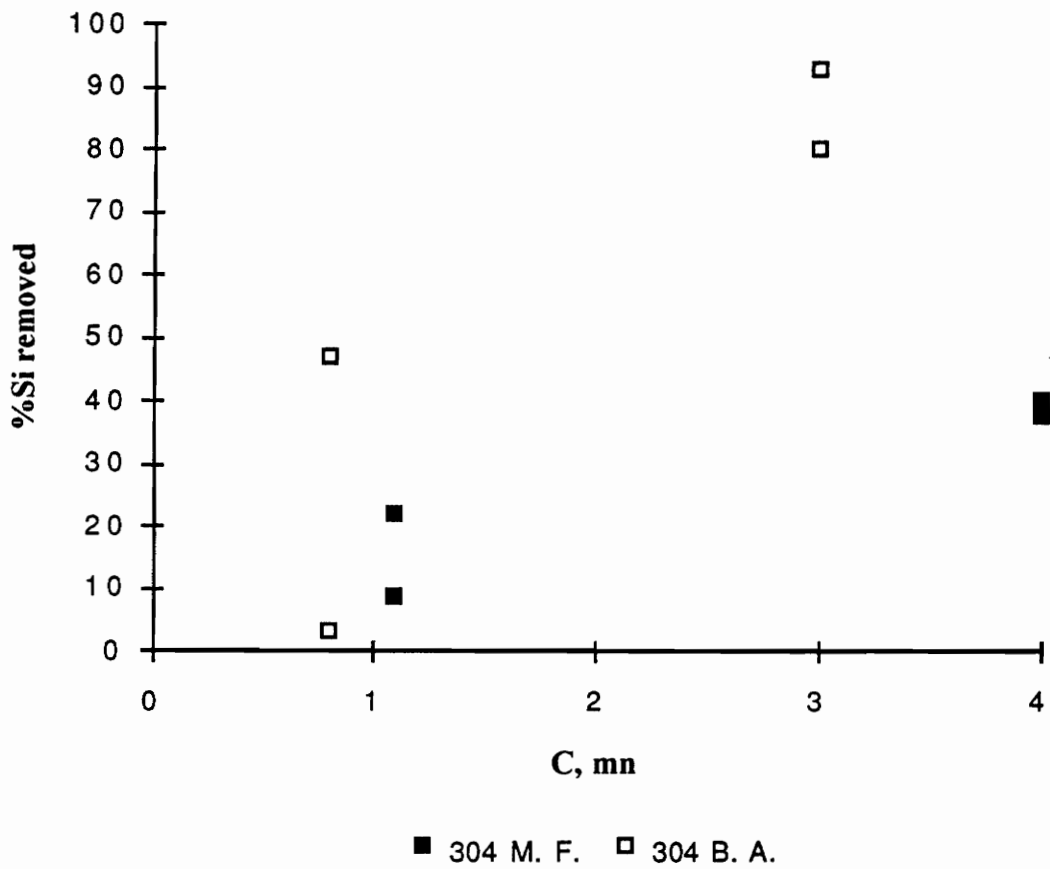


Figure 6.10. Atomic percent Si removed after cleaning in hexane as a function of the carbonaceous contaminant layer.

(i.e. the rough and dirtier surface) sample indicating a weak bond between the oxide and the silicone.

6.3.5 Water immersion

The effect of water was to decrease the fracture energy measured on all the samples. Peeling in water changes the interfacial energy and can decrease the thermodynamic work of adhesion.⁴ In the present work, ESCA measurements show that the silicone content was always less after peeling the samples in water than in air. Peeling in water not only changed the thermodynamic work of adhesion but also affected the surface in a chemical way. Different mechanisms have been described to explain how water can degrade adhesion.^{5,6,7} As the passive layer should not be significantly affected by the water, the decrease of the peel strength in water was possibly due to a detachment of the organic adhesive at the interface. The relative decrease in the silicone content measured on the steel surface after peeling in water compared to air is shown in Figure 6.11. The relative decrease in silicone after peeling in water was greater for the Mirror Finished (smooth surface) stainless steel than the decrease indicated for the Bright Anneal stainless steel (rough surface). This result suggests that roughness improves resistance to water deterioration at the sealant/metal oxide interphase.

6.4 Model of Failure Surface

The fracture energy measured for all the different samples is plotted as a function of the PDMS left on the surface after peeling but before hexane washing in Figure 6.12.

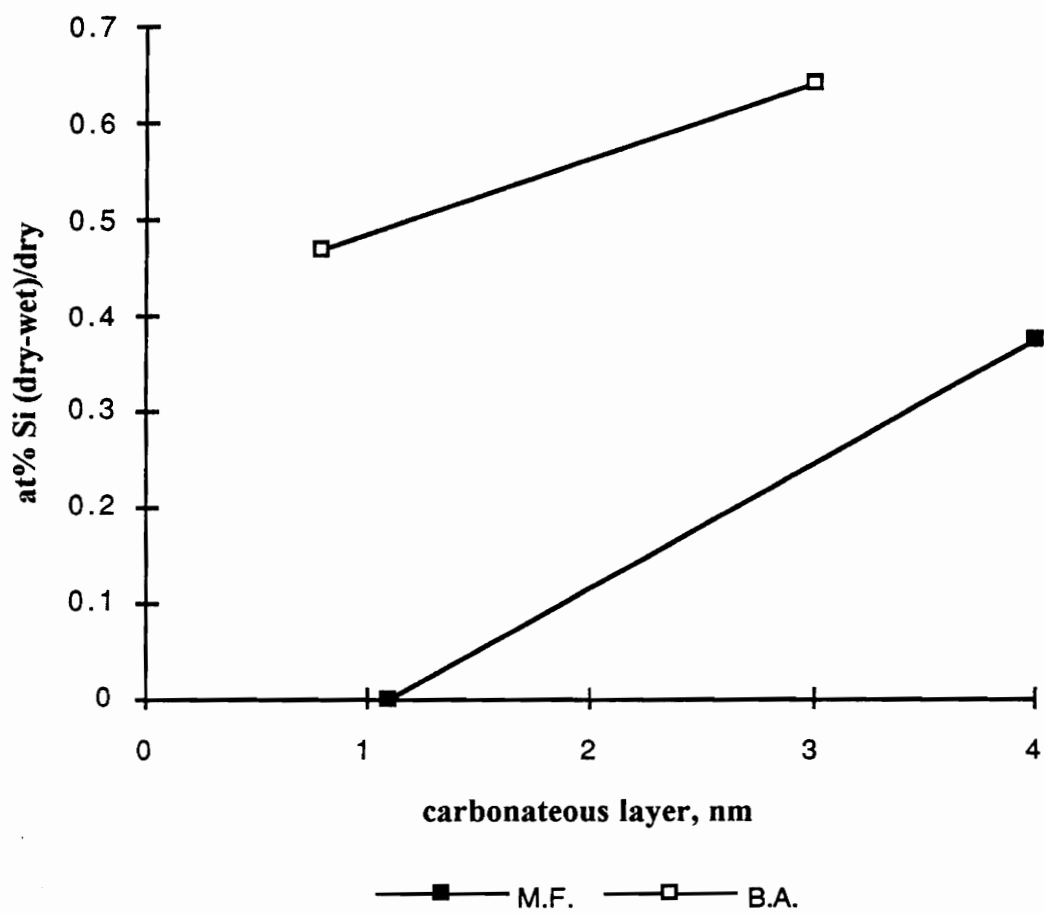


Figure 6.11. Decrease in atomic percent silicon after debonding in water vs. air.

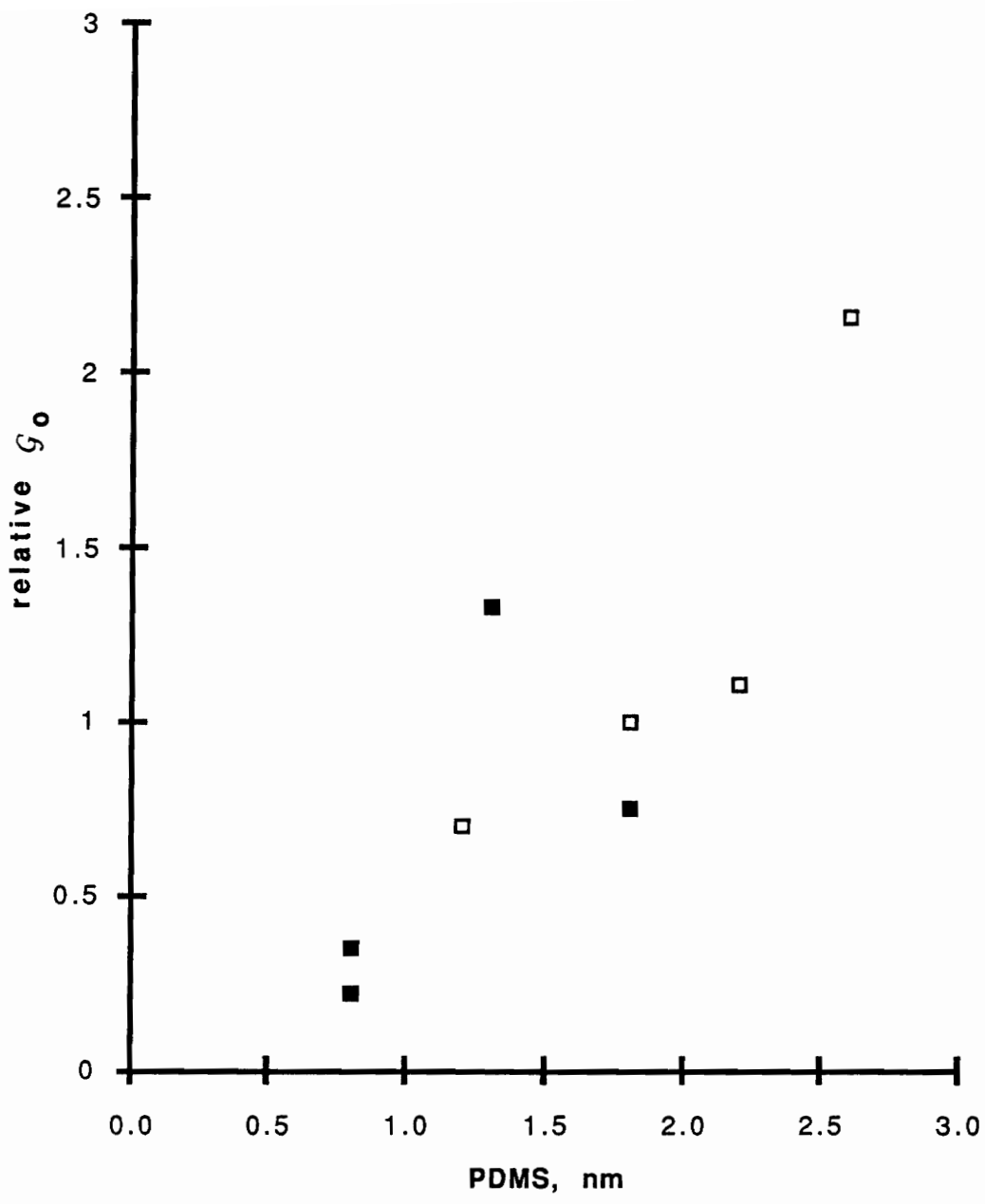


Figure 6.12 Fracture energy (N/m) as a function of the PDMS film thickness left on the surface after peeling.

The silicone thickness was calculated by using equation 3.4 and assuming a smooth layer. This assumption is not totally correct as seen in the AFM image in Figure 6.7. The fracture energy was proportional to the level of silicone left on the surface of the steel (see Fig. 6.12). This increase of the PDMS left on the substrate is like going from a pure interfacial failure to a cohesive one. The threshold fracture energy for a cohesive failure in the same sealant was measured by the 45 ° peel test method using cleaned glass as the substrate and a relative G_0 , 18.2, was found (see Fig. 6.6a). This value is in good agreement with the bulk fracture energy reported by Gent.⁸ A linear relationship between the fracture energy and the amount of PDMS left on the surface after peeling is assumed. The amount of PDMS on the surface corresponding to a relative G_0 of 18.2 can be extrapolated from Figure 6.13. A value of 24 nm is obtained for a smooth layer.

As seen in Fig. 6.7b the sealant may be removed in strips. If the cross-link density is assumed to be the same for the interphase as found in the bulk, the distance between cross-links can be estimated to be about 9 nm which corresponds well with the height of the strips in Fig. 6.7. This is very close to the minimum distance needed to yield cohesive failure as calculated from Fig. 6.13. It is suggested then that failure occurred either at the interphase in the carbonaceous contamination layer or at the distance of one to four PDMS cross links above the interface. The increase in atomic

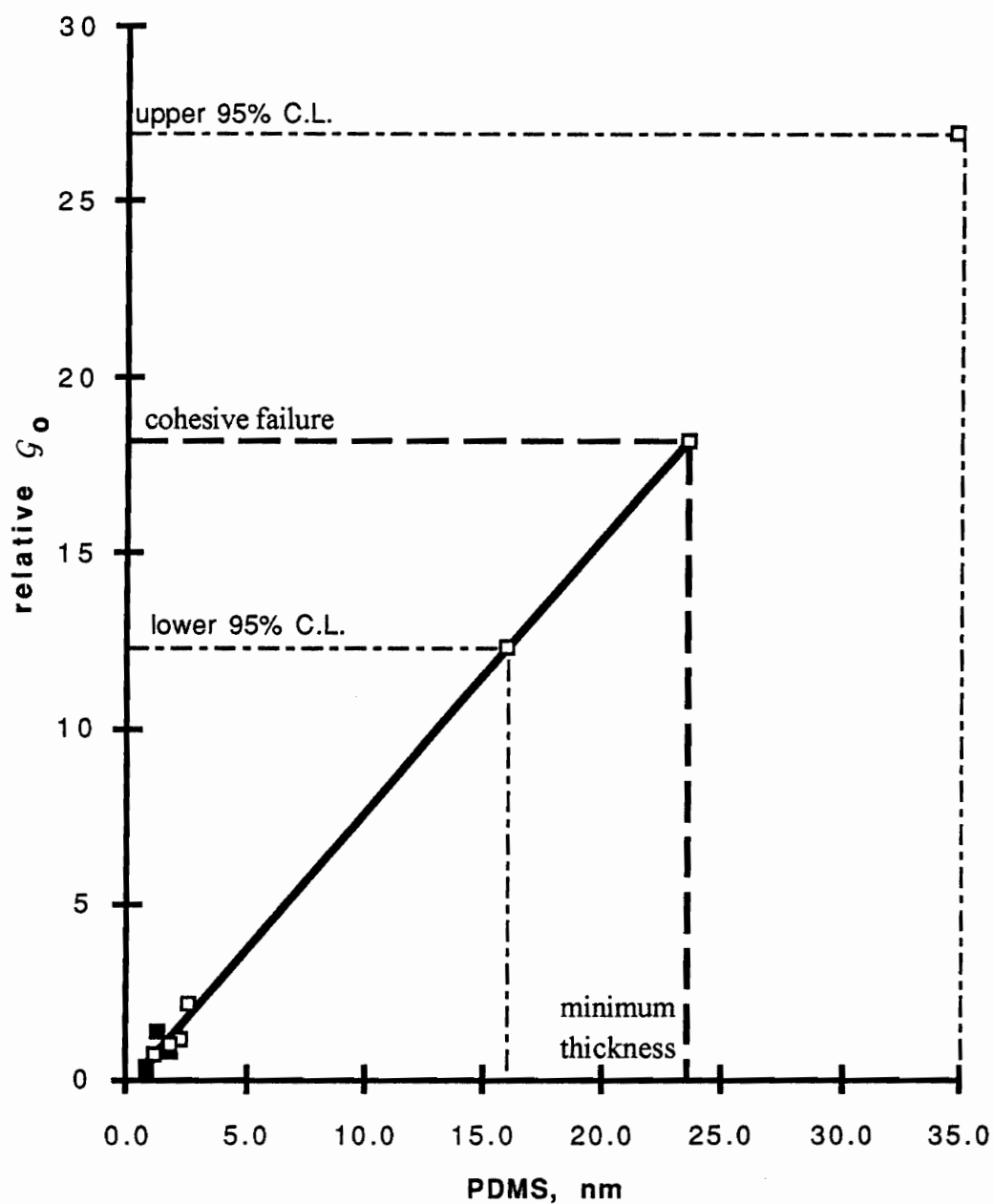


Figure 6.13 Fracture energy (N/m) as a function of the PDMS film thickness left on the surface after peeling. Extrapolation to 100% cohesive failure.

concentration of silicone may indicate the presence of more strips left on the surface not necessarily an increase in the thickness of PDMS left on the surface. Total coverage of the surface with these strips would be equivalent to cohesive failure.

6.5 Summary

ESCA and AFM have been combined to identify the topography and elemental composition of the fracture surface of silicone sealant on stainless steel. The interfacial failure surface for PDMS on stainless steel was within 10 nm of the surface. When the fracture occurred in this interphase, the fracture energy was proportional to the amount of distance between two cross links.

Carbonaceous contamination was not displaced by the sealant from the stainless steel substrate. Contamination inhibited primary bonding (ionic or covalent) and resulted in a lower fracture energy.

Roughness increased the fracture energy; and this effect was more pronounced when the surfaces were cleaner. In other words, the improvement in adhesion due to roughness was not as significant without the presence of good interfacial contact between the sealant and the stainless steel.

Water lowered the fracture energy especially for the dirtier surfaces. Roughness reduced the effect of the water damage but doesn't eliminate it.

6.6 References

¹M. Mantel and J. P. Wightman, *Surface and Interface Analysis*, **21**, 595 (1994).

² D. Maugis, *Journal of Adhesion*, **1**(2), 105 (1987).

³ H. F. Webster and J. P. Wightman, *Langmuir*, **7**, 3099 (1991).

⁴ A. N. Gent, J. Schultz, *Journal of Adhesion*, **3**, 281-294 (1972)

⁵ W. D. Bascom, *Journal of Adhesion* **2**, 161 (1970)

⁶ R. A. Gledhill and A. J. Kinloch, *Journal of Adhesion* **6**, 315 (1974)

⁷ R. A. Gledhill and A. J. Kinloch and S. J. Shaw, *Journal of Adhesion* **11**, 3 (1980)

⁸ Gent, A. N., Liu, G., *Journal of Adhesion*, **38**, 79 (1992)

VII. Results and Discussion:

45 ° Peel Adhesion Doubly Shifted Master Curves for Silicone Sealant Adhesion to Aluminum by varying Temperature and % Relative Humidity

Relative humidity and temperature are important variables which can influence the fracture energy and failure mode for the sealant bond to aluminum. The relative humidity and temperature were systematically adjusted and the fracture energy and crack speed were measured for each condition. The sealant was a high modulus formulation designed to increase the likelihood of interfacial failure. The relationship between relative humidity, temperature, fracture energy and crack tip speed was determined and rate equations developed by the method of reduced variables as described in section 2.4.

7.1 Sealant Modulus in Uniaxial Tension

A high modulus sealant was prepared for this study as outlined in section 3.1.1. The sealant formulation was designated 249-3. The level of fumed silica in the sealant formulation was increased to obtain the higher modulus. The modulus was measured under equilibrium conditions for comparison to the previous sealant formulations.

7.1.1 Equilibrium Conditions

The equilibrium modulus was measured as described in section 3.3.2.1. The stress vs. strain data can be found in Figure 7.1. The analysis of the data was identical to the methods used in section 4.1.2.1. The Gaussian chain elastomer model was used to plot the stress vs. a complex function of the strain in Figure 7.2. The strain energy to break, Young's modulus, Gaussian chain elastomer modulus, strain to break and stress to break are summarized in Table 7.1. The modulus was significantly higher than the previous sealants. The strain to break was much lower. The strain energy to break was also lower than previous formulations.

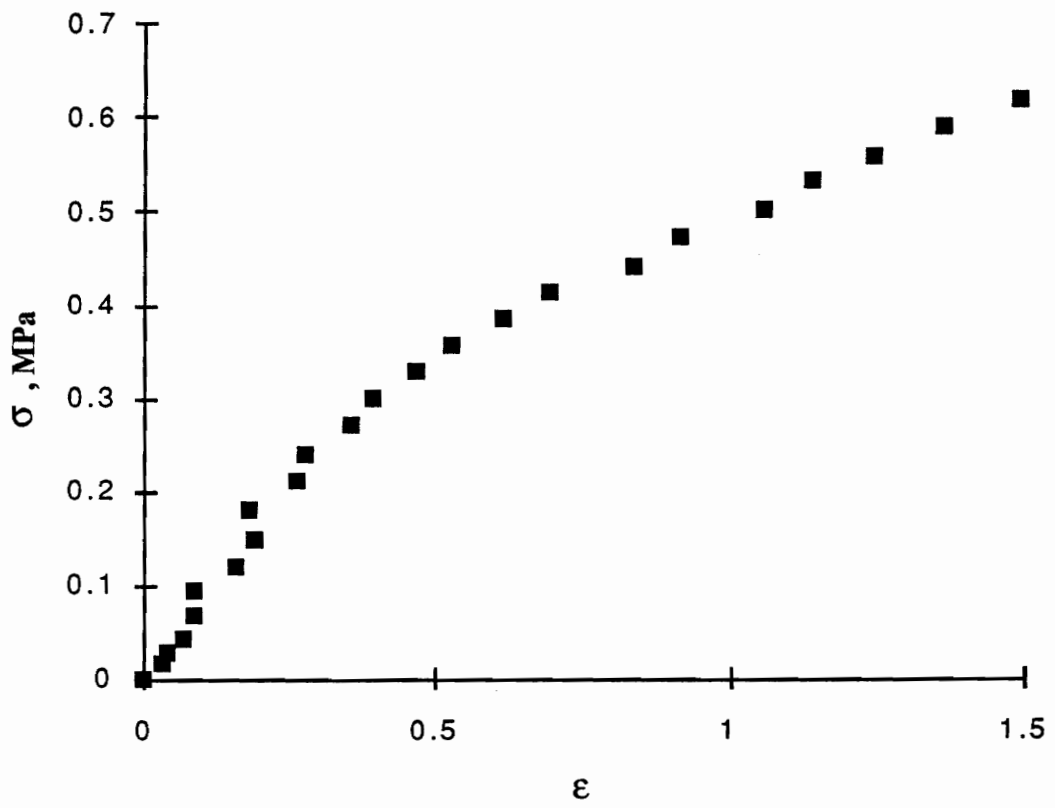


Figure 7.1 Stress vs. strain under equilibrium conditions for sealant formulation 249-3.

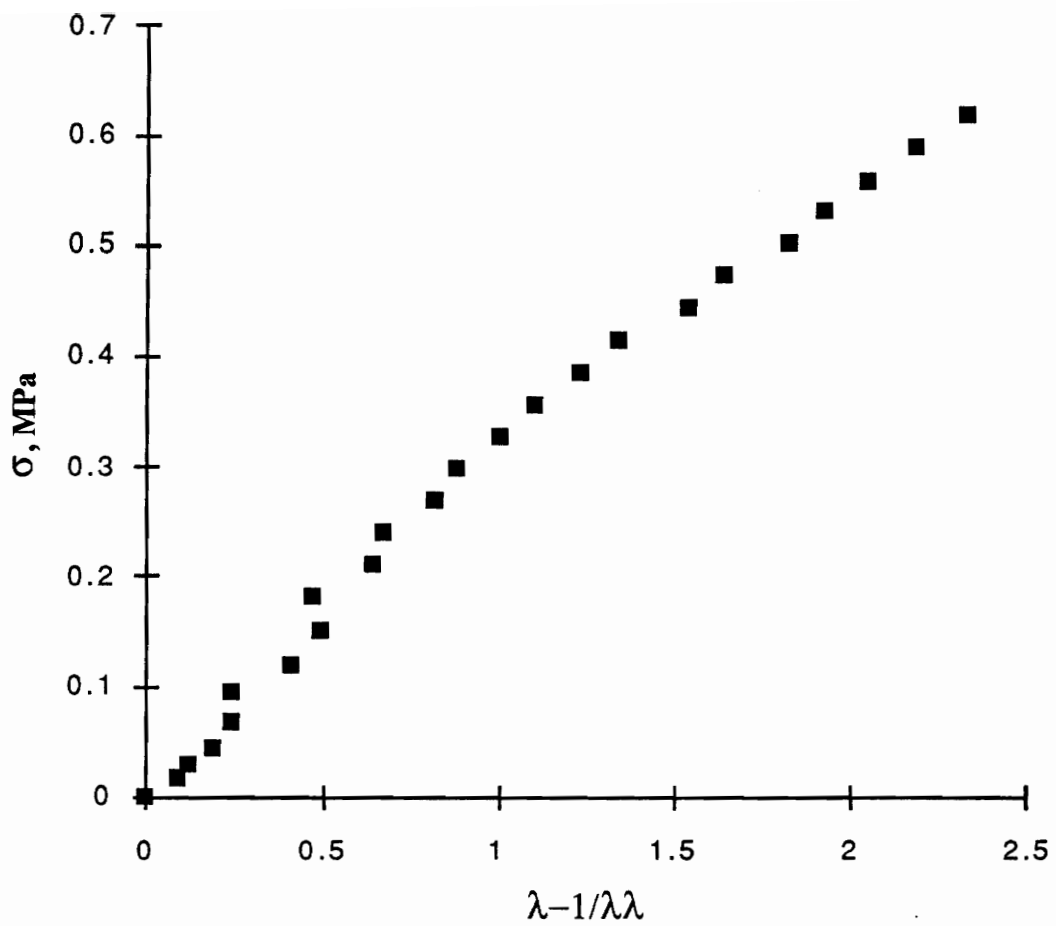


Figure 7.2 Stress vs. complex strain function for sealant 249-3 using the Gaussian elastomer model at equilibrium.

Table 7.1 Rubber properties obtained at equilibrium strain rate for sealant 249-3.

Sealant reference number	Stress at break, MPa	Strain at break	Young's Modulus, MPa	Gaussian Elastomer Modulus, MPa	Energy to Break, MJ/m ³
249-3	0.647	1.62	0.866	1.046	7.13

7.2 Aluminum Surface Analysis

The aluminum surface was cleaned and polished as described in section 3.2.1. After cleaning, the surfaces were examined with scanning electron spectroscopy and by ESCA to determine the relative roughness and atomic concentration on the surface.

7.2.1 Scanning Electron Microscopy

The SEM micrographs taken after polishing and cleaning can be seen in Figure 7.3. Long parallel grooves, approximately 3 microns in width and depth, are evident. The grooves were formed by the rotation of the polishing wheel. The direction of pull during the peeling test was parallel to the grooves.

7.2.2 ESCA

The results of ESCA analyses can be found in Table 7.2. The oxide thickness is the same as the solvent cleaned aluminum at about 4 nm. The carbon atomic concentration was slightly less than the solvent cleaned aluminum.

7.3 Fracture Energy Measurement

The fracture energy was measured as a function of crack speed according to the procedure outlined in section 3.5.2. The fracture measurements were first conducted at a constant temperature of 50 °C with varying levels of relative humidity then at a constant relative humidity of 49% with varying temperature levels. Measurements were duplicated at several intervals to insure the testing was repeatable.

The log of the fracture energy vs. the log of the crack speed is plotted in Figure 7.4. Increasing temperature or relative humidity (rh) increased the crack speed for a given fracture energy. The failure mode was very near the interphase of the aluminum oxide layer for all test conditions above 35% relative humidity. Fracture which was conducted below 35% relative humidity failed cohesively in the sealant independent of the

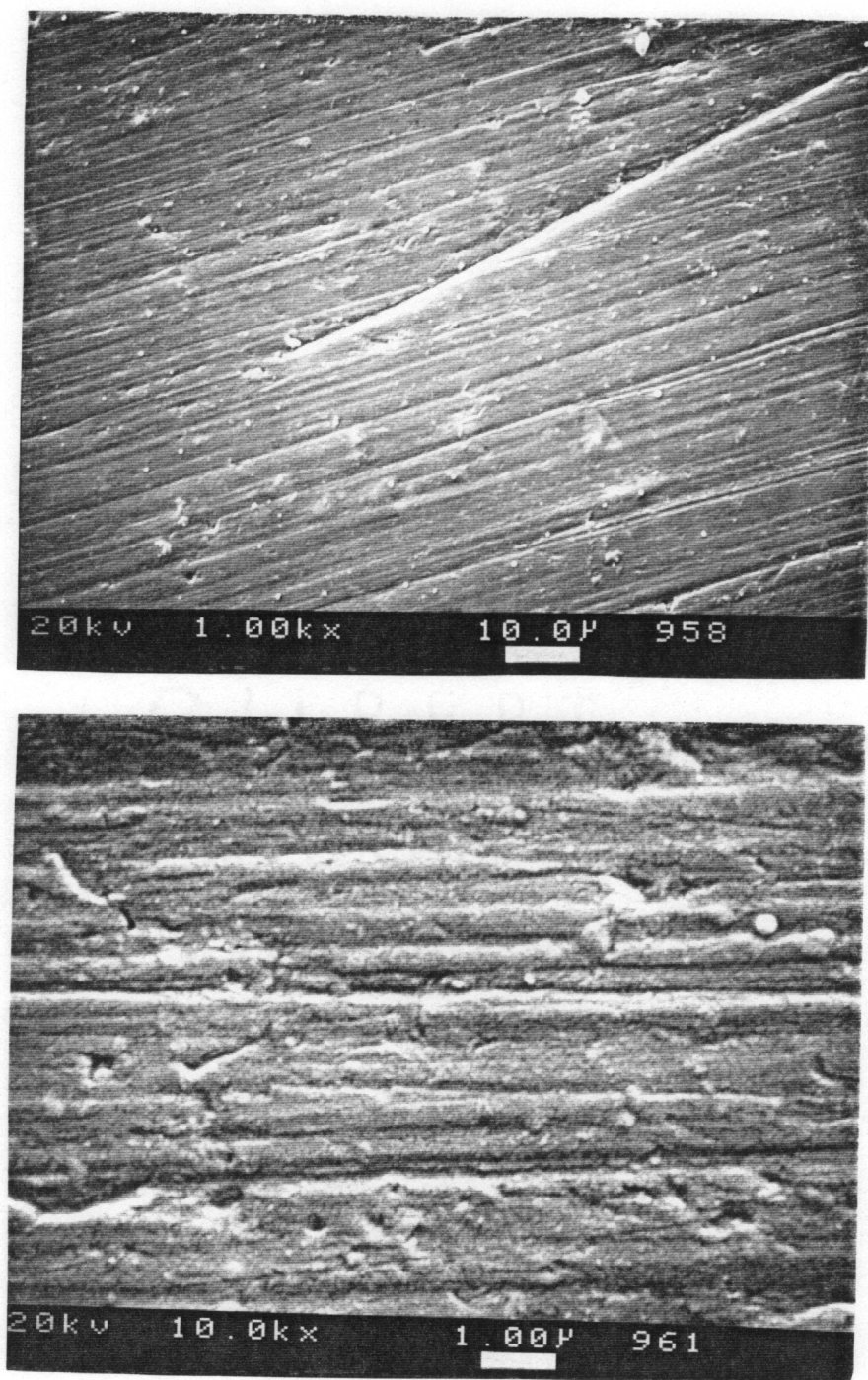


Figure 7.3 Scanning electron micrographs of polished and cleaned aluminum.

Table 7.2 ESCA results for polished and cleaned aluminum.

Electron		Atomic concentration, %
C 1s		32.8
O 1s		53.2
Al 2p _{3/2}	alloy	2.7
	oxide	20.1
Au 4f _{7/2}		1.2
oxide thickness, nm		4.1

Take-off angle of 45°

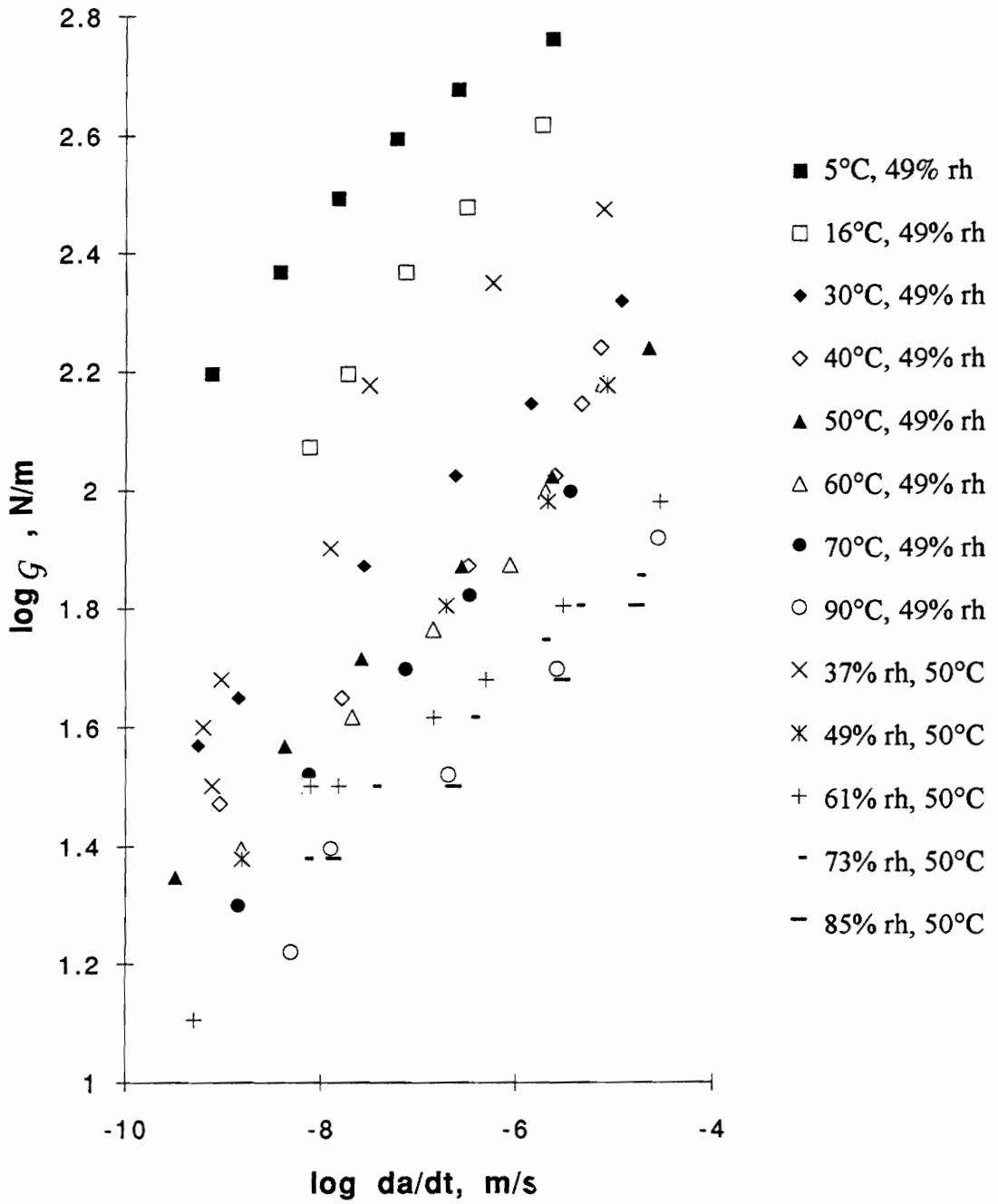


Figure 7.4 Logarithm of fracture energy vs. logarithm of crack speed.

temperature. Cohesive failure data was not studied in this work. The two duplicate curves, labeled “50°C and 49% relative humidity” and “49% relative humidity 50 °C” were in good agreement with only a slight deviation at the lower crack speeds.

7.4 Fracture Surface Analysis by SEM

Figure 7.5 contains the SEM photomicrographs of the aluminum fracture surface. The aluminum surface was identical to the surface of the polished and cleaned aluminum from Figure 7.3. Any differences between the two surfaces was too small to be resolved by the SEM instrument. It should be noted that the SEM used for this work was a relatively low resolution model as described in section 3.4.1. Clear photomicrographs could only be obtained at a magnification of 10000 times or less.

7.5 Fracture Surface Analysis by ESCA

As can be seen in Table 7.3, the surface of the aluminum contained 18.4 at % silicon. This is consistent with the ESCA data in Table 5.3. While the surface contained silicone sealant, the atomic concentration of silicon is less than the amount which would be detected if the surface was completely covered with sealant. Again, the failure was mixed mode with some interfacial failure between the sealant and the aluminum substrate and some cohesive failure occurring in the sealant.

7.6 Master Curve Plot

The reference condition of 50 °C and 49% relative humidity was used to compare all the other conditions. The fracture energy curves of Figure 7.4 were horizontally shifted to coincide with the 50 °C and 49% relative humidity curves. The resulting curve was fit with a linear equation during the shifting procedure, as outlined in 2.4, to obtain a smooth curve containing all the fracture data. Figure 7.6 contains the results of the above shifting procedure. The single curve represented in Figure 7.6 is the resulting master curve for the

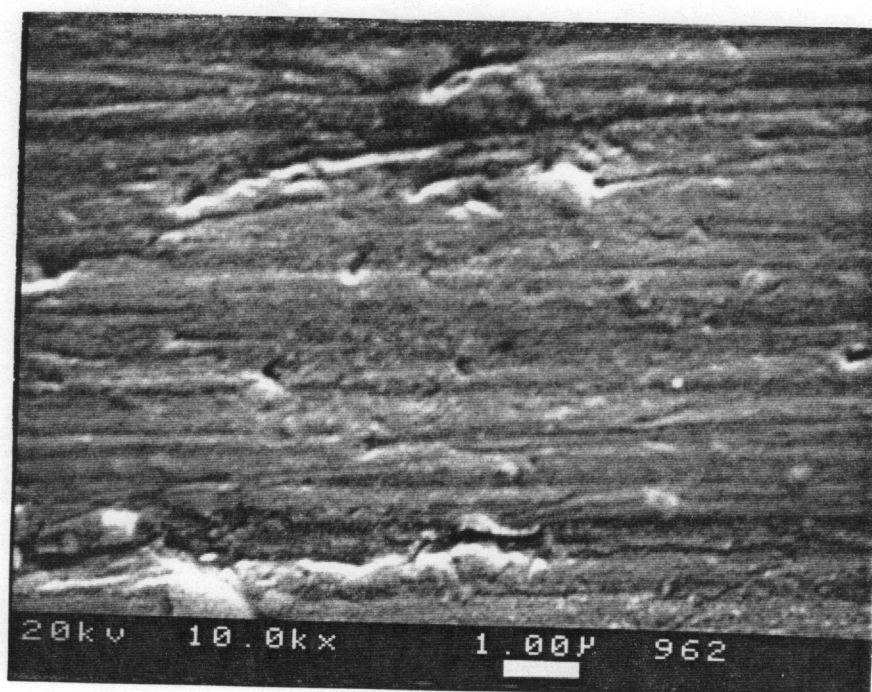
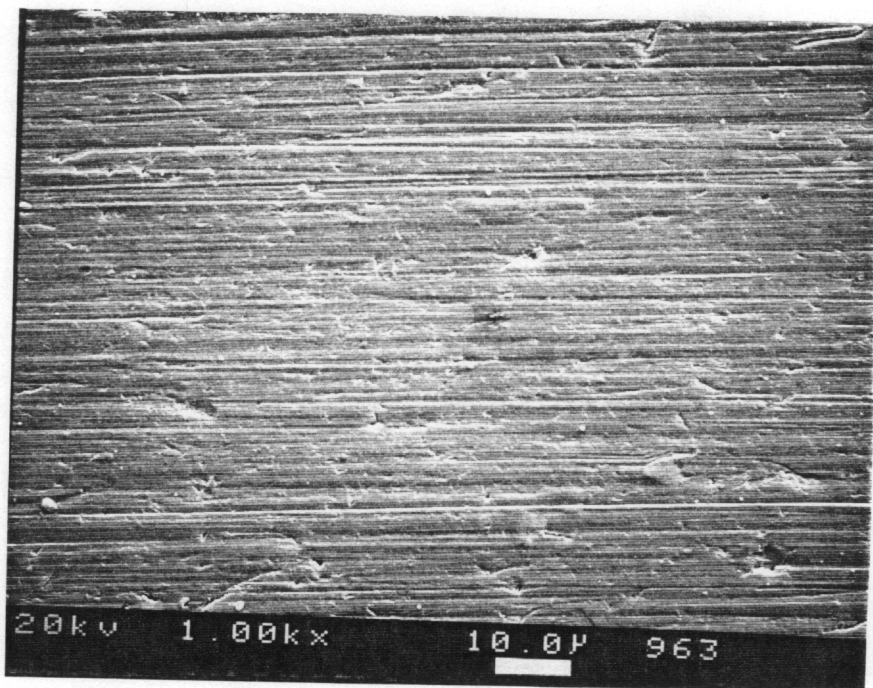


Figure 7.5 SEM image of aluminum fracture surface.

Table 7.3 ESCA results for aluminum fracture surface.

Electron		Atomic concentration, %
C 1s		38.5
O 1s		31.7
Al 2p _{3/2}	alloy	1.3
	oxide	8.5
Si 2p _{3/2}		18.4
Au 4f _{7/2}		1.6
oxide thickness, nm		4.1

Take-off angle of 45°

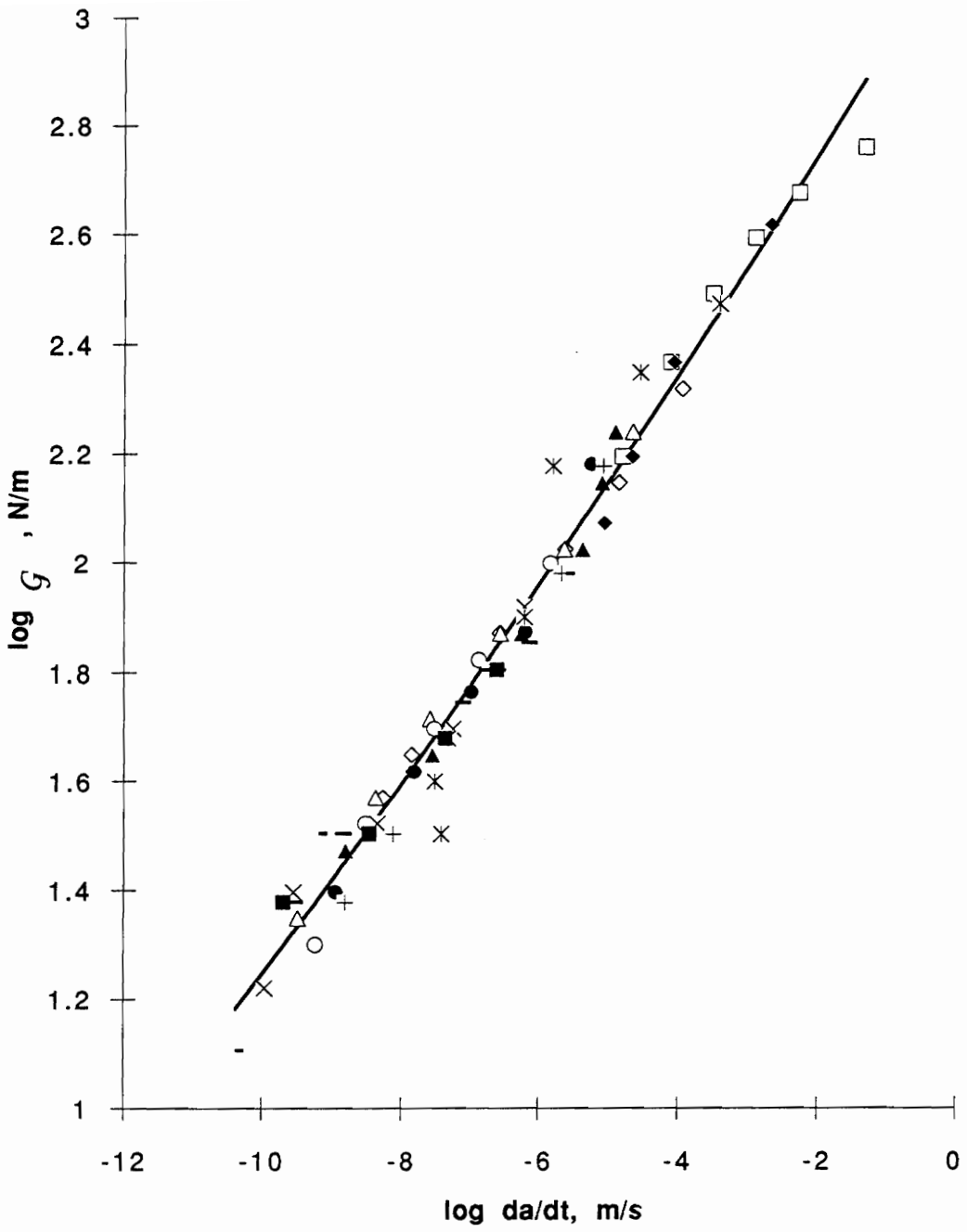


Figure 7.6. Master curve for 50 °C and 49% relative humidity.

reference temperature of 50 °C and 49% relative humidity. The master curve covers four more decades of crack growth than was obtained for any individual test condition.

7.7 Shift Factor Plots

For each condition of fracture testing, the amount of horizontal shifting which was necessary to match the reference condition is known as the shift factor. The shift factor used to account for changes in relative humidity was designated a_{rh} ; the shift factor for horizontal shifts due to changes in temperature was designated a_T . The shift factors along with the two coefficients for the fitting equation are summarized in Table 7.4. A plot of the shift factor vs. the testing condition can be found in Figure 7.7 and 7.8 for the relative humidity shift factors and the temperature shift factors respectively.

The shift factor plot for relative humidity is a smooth monotonic function to which a quadratic equation was fit. A smooth monotonic shift factor curve indicates no change has occurred in the mechanism of crack propagation over the range of relative humidity tested. The general shape of the shift factor plot is very similar to the WLF curves for viscoelastic processes.¹ This may be the result of plasticization of the crack tip by water ingress. Such an event could lead to a change in the free volume of the polymer. Changes in the polymer free volume directly affect the rate of motion of the polymers in a similar way as the temperature variable in the WLF theory.²

The shift factor plot for temperature also described a smooth monotonic function. However, the curve could not be related to the WLF theory. Attempts to linearize the WLF equation were not successful. This suggests that this shift variable is not governed by the relative speed of the molecular motions of the polymer. Therefore a chemical rate analysis was performed using the Arrhenius relationship. The resulting plot seen in Fig. 7.8 results in an activation energy for the fracture process of about 31.2 kcal/mol.

In Fig. 7.6 the master curve was shifted to 50 °C and 49% relative humidity. The

Table 7.4. Summary of shift factor data and linear equation coefficients.

Temperature, °C	% Relative Humidity	Log a_T
5	49	4.477
16	49	3.132
30	49	1.006
40	49	0.236
50	49	0.000
60	49	-0.147
70	49	-0.391
90	49	-1.626

Temperature, °C	% Relative Humidity	Log a_{rh}
50	37	1.691
50	49	0.000
50	61	-1.051
50	73	-1.364
50	85	-1.806

Linear fit to Fracture data.	
Coefficient 1	3.0651
Coefficient 2	0.184

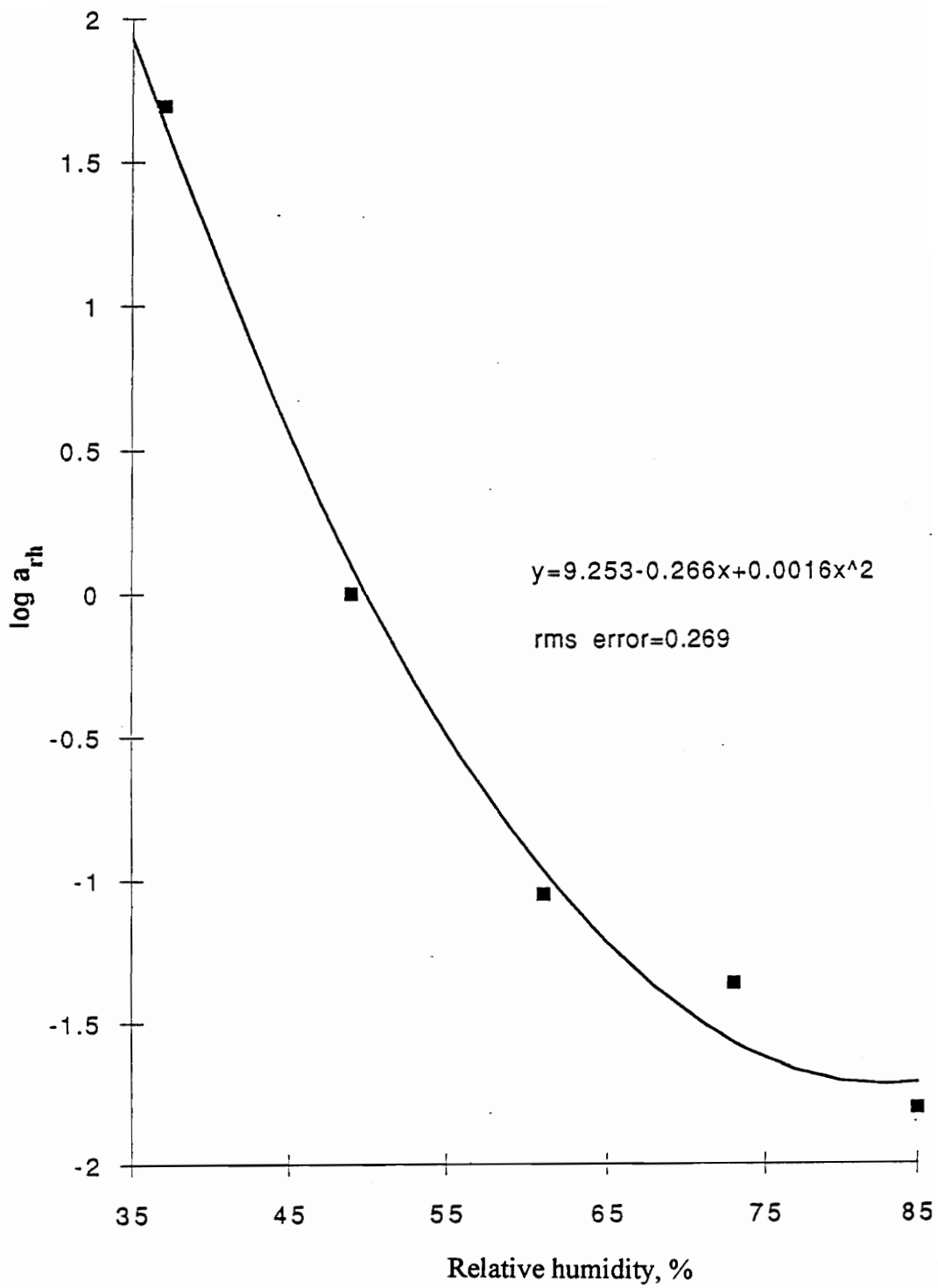


Figure 7.7 Shift factor plot for a_m .

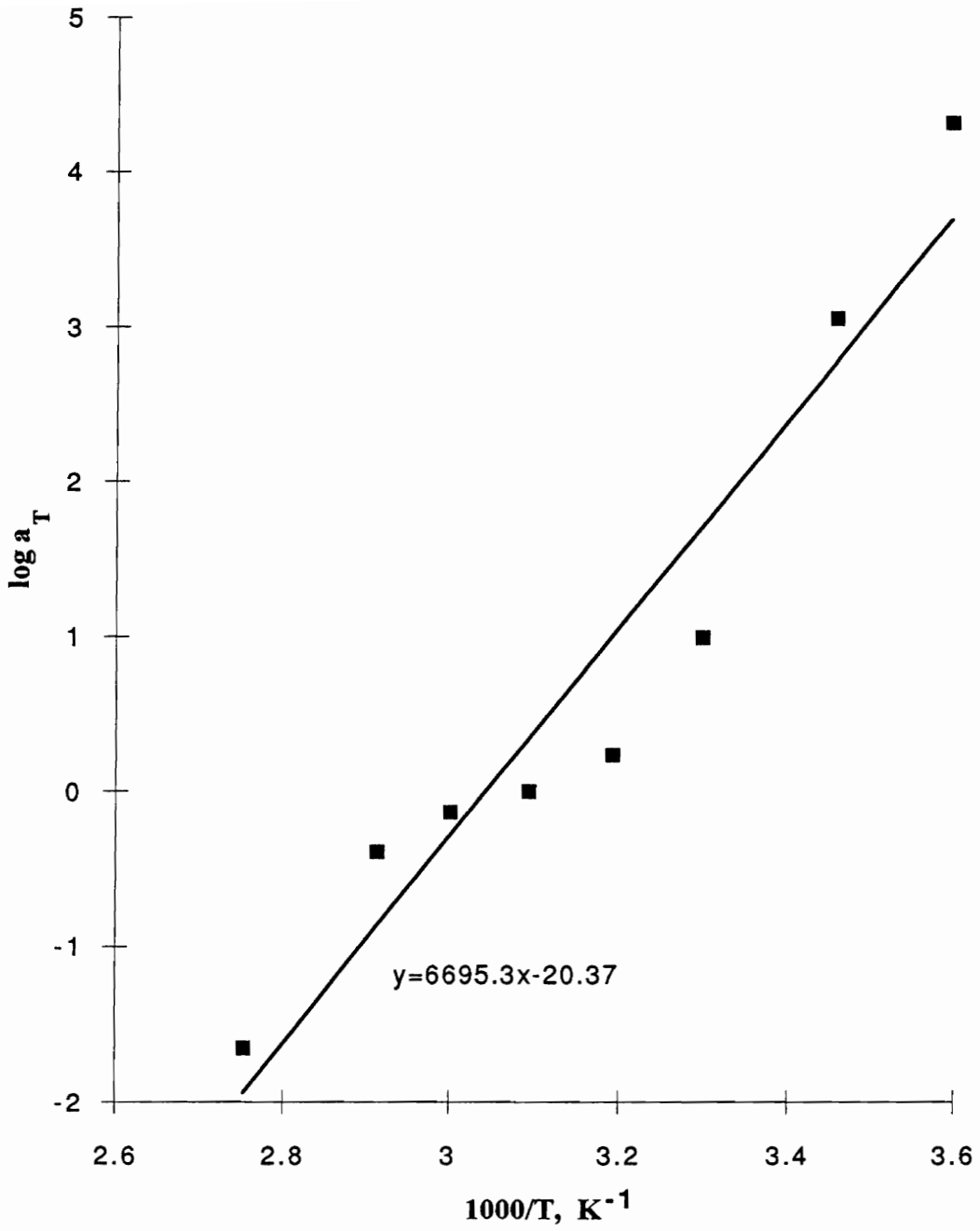


Figure 7.8 Shift factor plot for a_T using Arrhenius relationship.

same master curve can now be shifted using linear combinations of the two shift factor plots from Figs. 7.7 and 7.8. The shift factor for 5 °C and 37 % relative humidity is 6.168. The shift factor for the other extreme of 90 °C and 85 % relative humidity is -3.532. By applying these shift factors to the master curve of Fig. 7.6, two new master curves are obtained which define the outer limits of the experiment. Figure 7.9 contains plots of all three master curves. Twenty decades of crack rate can be measured. By using the appropriate shift factors, any crack speed within the twenty decades can be related to the relative humidity, temperature and fracture energy.

7.8 Crack Growth Rate Equation

The fracture energy master curve equation can be combined with equations for the two shift factor plots to yield an equation relating fracture energy to crack rate, temperature and relative humidity as follows:

$$\log G = \log k + n(\log \dot{a} + \log a_T + \log a_{rh}) \quad (7.1)$$

$$G = k(\dot{a} a_T a_{rh})^n \quad (7.2)$$

$$k = 10^{c_1} \text{ and } n=c_2 \text{ from the linear fit of the master curve}$$

where equation 7.2 is valid for 278.2 °K < T < 363.2 °K and 37% < rh < 85%. The lower limit on relative humidity was required to avoid a change in the failure mode. When the relative humidity was less than 35%, the failure mode was cohesive in the sealant. Equation 7.2 can be rearranged to solve for crack rate as a function of fracture energy, temperature and relative humidity as follows:

$$\dot{a} = \left(\frac{G}{k} \right)^{1/n} \frac{1}{a_T a_{rh}} \quad (7.3)$$

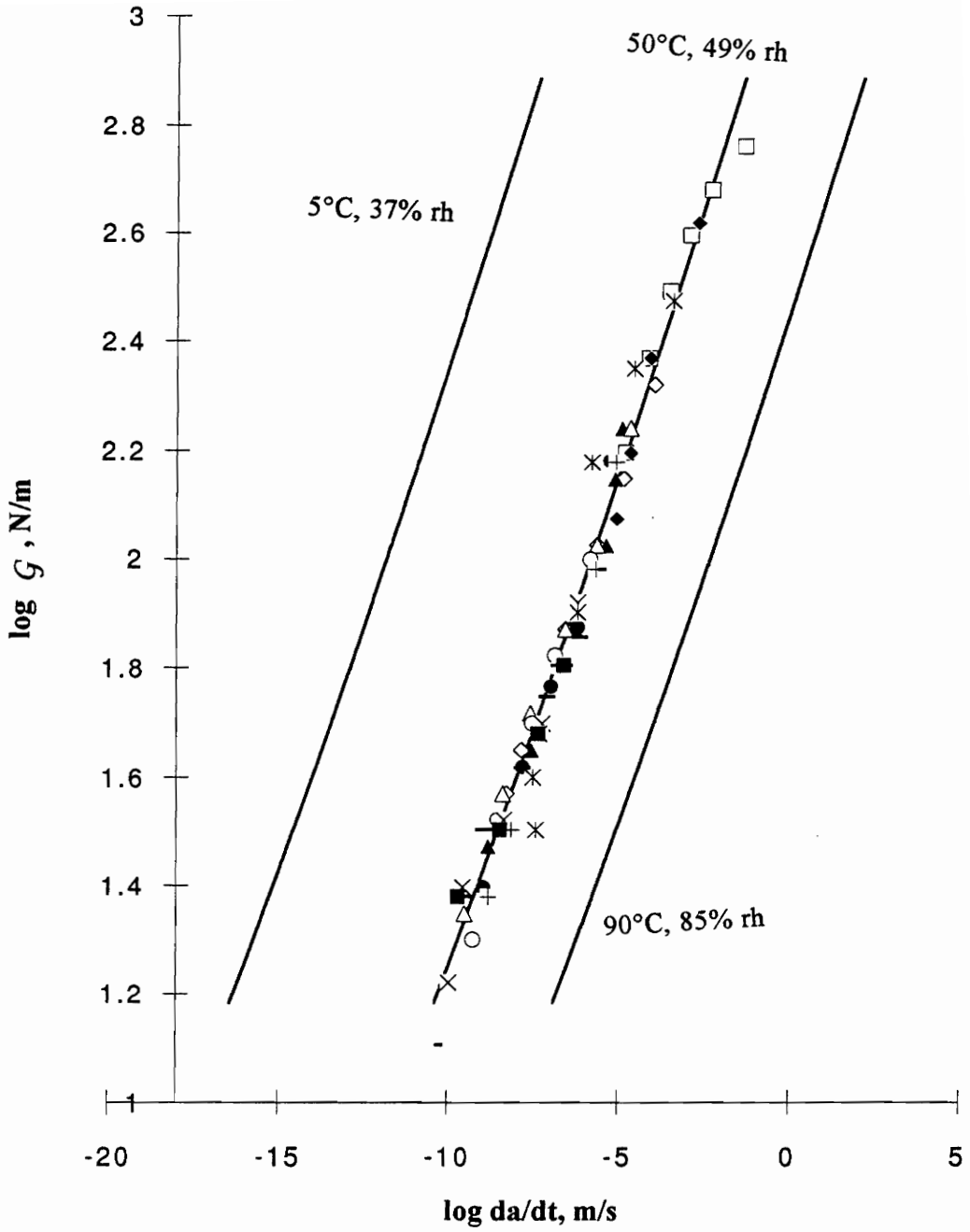


Figure 7.9. Master curves for logarithm of fracture energy vs. logarithm of crack rate extended to cover 20 decades of crack rate.

7.9 Summary

The failure mode for PDMS on aluminum changed from near the aluminum oxide layer to cohesive in the sealant when the relative humidity was less than 35%. This phenomenon was independent of the test temperature. For the failure near the aluminum oxide, a doubly shifted master curve was constructed for the PDMS aluminum joint using temperature and relative humidity as the shifting variables. The shift factor plots formed smooth monotonic functions indicating no change in mechanism for crack advancement. The temperature shift factor was not related to the WLF theory but worked well with an Arrhenius theory. The activation energy for the fracture process was calculated to be 31.2 kcal/mol. A doubly shifted master curve equation was developed which related crack speed to fracture energy, temperature and relative humidity.

In the next two sections, the above equation will be used to predict the crack rate for butt joints loaded in tension as a function of fracture energy, temperature and relative humidity.

7.10 References

¹M. L. Williams, R. F. Landel, and J. D. Ferry, *Journal of the American Chemical Society*, **77**, 3701 (1955).

²J. J. Aklonis and W. J. MacKnight, *Introduction to Polymer Viscoelasticity*, 2ed. pg. 50, John Wiley and Sons Inc., New York (1983).

VIII. Results and Discussion:

Application of Shifting Variables to the Silicone Sealant Butt Joint

The peel test has been ridiculed for its inability to yield results which can be correlated to real world applications. This is especially true when the test is conducted according to the usual standard methods described in section 2.6.1. In this study, the 45° peel data obtained in chapter VII will be correlated to fracture data obtained from a butt joint tested in uniaxial tension. As described in section 2.5.2 and Fig. 2.7c, the strain energy release rate for a butt joint in tension can be calculated from the size of the joint and the strain energy density. Therefore, the first experiment in this study was the measurement of the strain energy for the sealant at given displacements and temperatures. Relative humidity did not have an effect on the modulus of the sealant. Therefore it was not investigated in this study. After measuring the strain energy at different displacements and temperatures, the crack growth was measured under the same conditions to obtain a plot of strain energy release rate vs. crack growth. A good comparison between the butt joint data and the 45° peel data was obtained.

8.1 Equilibrium Stress vs. Displacement

Equilibrium stress vs. displacement measurements were conducted on formulation 245-3 as described in section 3.3.2.2. The butt joint was prepared using clean glass for the substrate to insure that the sealant would not pull away from the substrate during the test. The resulting stress vs. displacement isotherms can be seen in Figure 8.1. Each curve was nominally linear over the displacement interval studied. As expected from the theory of rubber elasticity, the modulus of the sealant, which is proportional to the slope of the lines in Figure 8.1, increased as the temperature increased. The curves of Figure 8.1 do not always go through the origin. Therefore, there was stress on the sealant even when

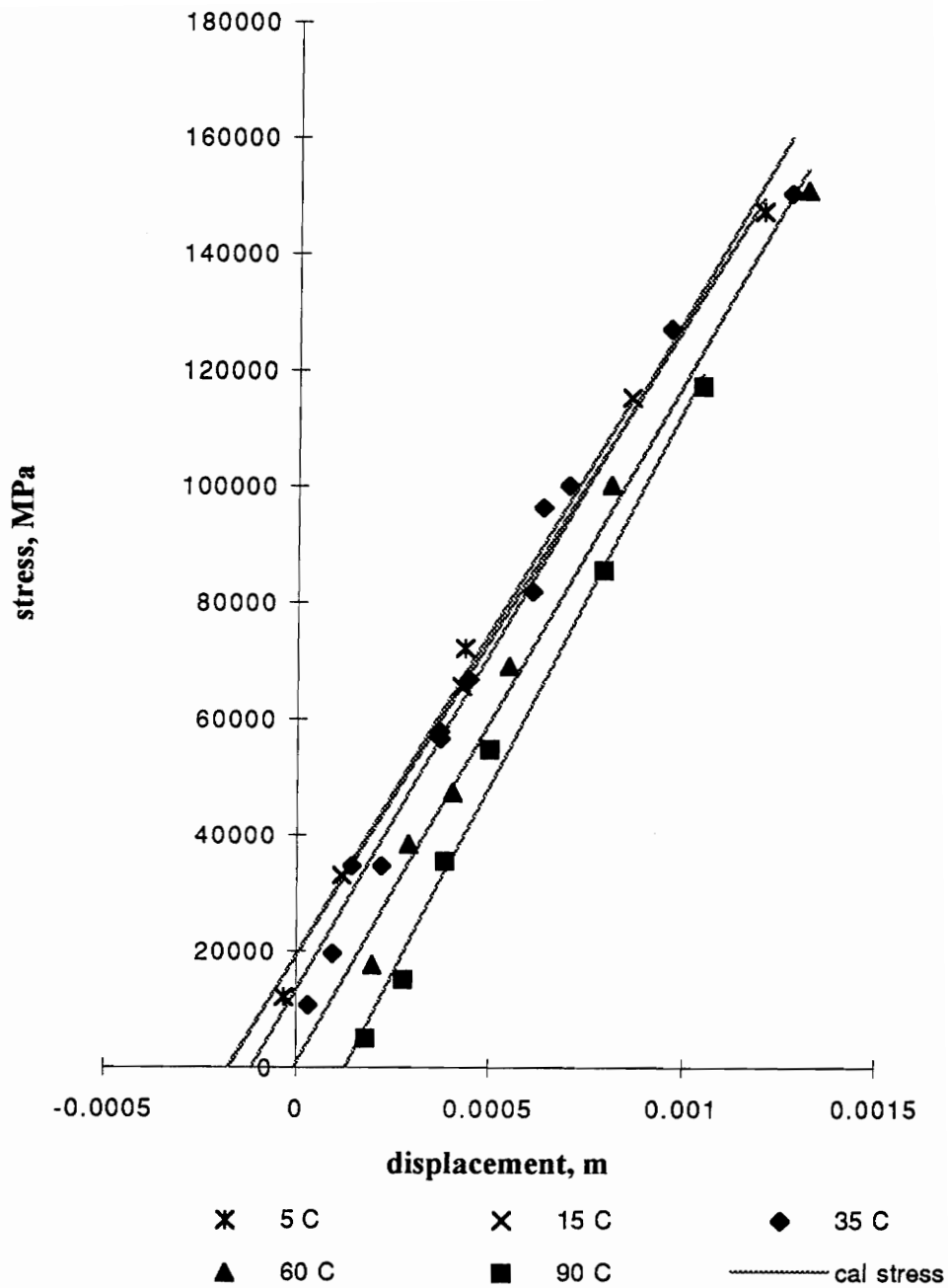


Figure 8.1 Stress vs. displacement for 249-3 sealant cured at 27 °C in butt joint configuration to glass substrates.

there was no displacement. This pre-stress can be the result of shrinkage during cure or thermal expansion after cure. The sealant was cured at approximately 27 °C. During the cure reaction, acetic acid is removed from the sealant. The loss of acetic acid results in shrinkage during cure. The shrinkage during cure results in a pre-stress in the sealant before any displacements are imposed. This can be seen by the positive intercept for the curves obtained at temperatures below 60 °C. However for the same small displacement, the load decreased when the temperature increased due to the thermal expansion of the sealant. Therefore, increasing the temperature above 60 °C places the sealant in a state of compression when the displacement of the sealant is small.

The area under the curve of the stress vs. displacement plot is the work required for a given displacement. This work is also known as the strain energy. Fitting a linear equation to the curves of Figure 8.1 and integrating results in the strain energy as a function of displacement as described in equations 8.1 and 8.2.

$$\sigma = mx + b \quad (8.1)$$

$$U = \int_{x_0}^x (mx + b) dx \quad (8.2)$$

where σ is the stress, x is the displacement in meters, m is the slope of the line, b is the intercept and U is the strain energy.

When the sealant joint failed, the strain energy was completely lost, therefore, x_0 is the value of x when the force equals zero. Thus, $x_0 = -b/m$ and G is now the strain energy release rate.

The temperature dependence of the strain energy release rate can be calculated by determining the temperature dependence of the stress vs. displacement. Figure 8.2a and b

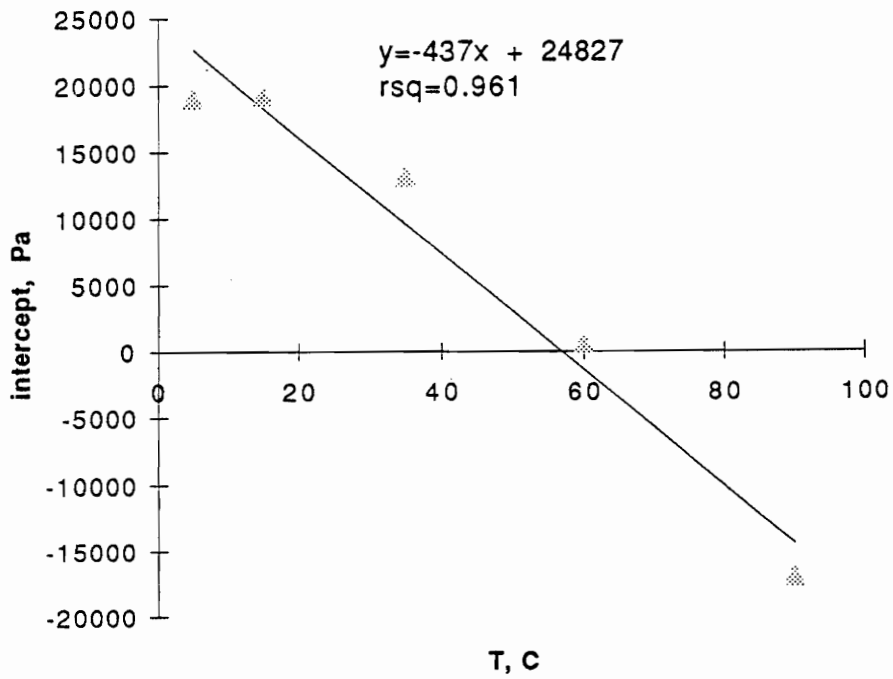
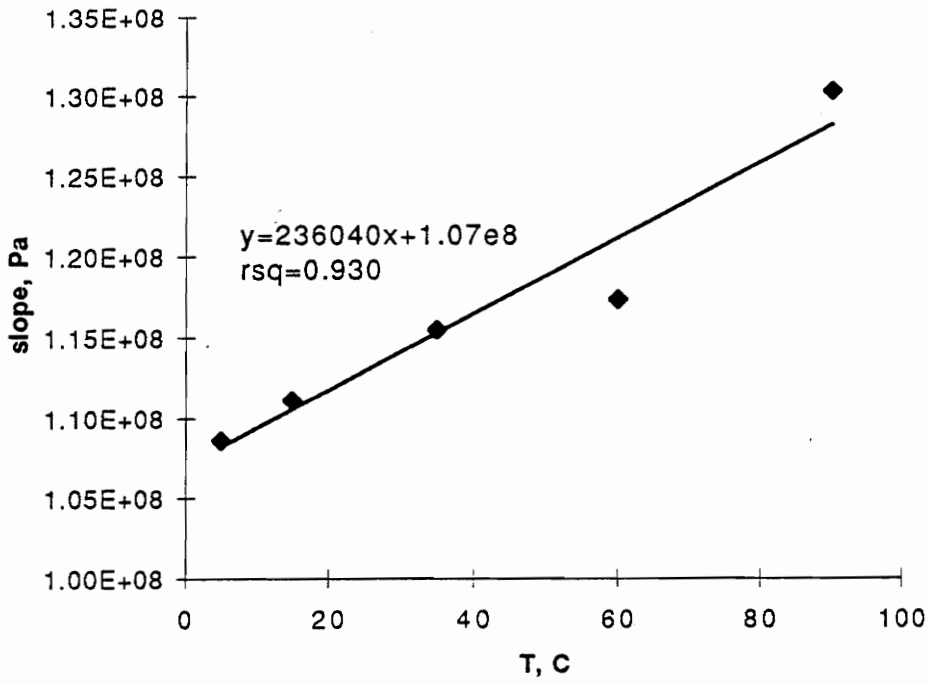


Figure 8.2. a) Slope, m , vs. temperature for regression data of Figure 8.1. b) Intercept, b , vs. temperature for regression data of Figure 8.1.

contains curves for m and b as a function of temperature, T . The curves were fit with linear equations.

$$m = 236040T + 1.07 \times 10^8 \quad (8.3)$$

$$b = -437T + 24827 \quad (8.4)$$

Equations 8.3 and 8.4 when combined with equation 8.2 define the strain energy release rate, G , as a function of displacement and temperature.

8.2 Fracture Energy vs. Crack Speed Measurement

Butt joints were prepared as described in section 3.5.4. Polished aluminum prepared in the same way as that described in Chapter VII was used for the substrates. The crack length was measured as a function of time at constant temperature, relative humidity and displacement. Figure 8.3 contains a plot of crack length vs time for several joint displacements. The crack growth was linear and appeared to be near the interface just as in Chapter VII. A summary of the crack growth data can be found in Table 8.1. The crack speed was obtained from the crack growth data. The strain energy release rate was calculated using equation 8.2 with the temperature dependent functions of equations 8.3 and 8.4. A plot of the logarithm of the strain energy release rate vs. the logarithm of the crack speed can be seen in Figure 8.4. A linear fit is obtained for the data. Only a small amount of data was obtained with the limited number of samples remaining after measuring the strain energy function.

8.3 Comparison to Peel Fracture Data

The data from the previous section was plotted on the same graph with data obtained from the 45° peel test conducted in Chapter VII and can be seen in Figure 8.5. The butt joint data indicates an 8% higher strain energy release rate than does the peel data for the same crack speed. In addition, scatter for the butt joint data is larger than for the peel test.

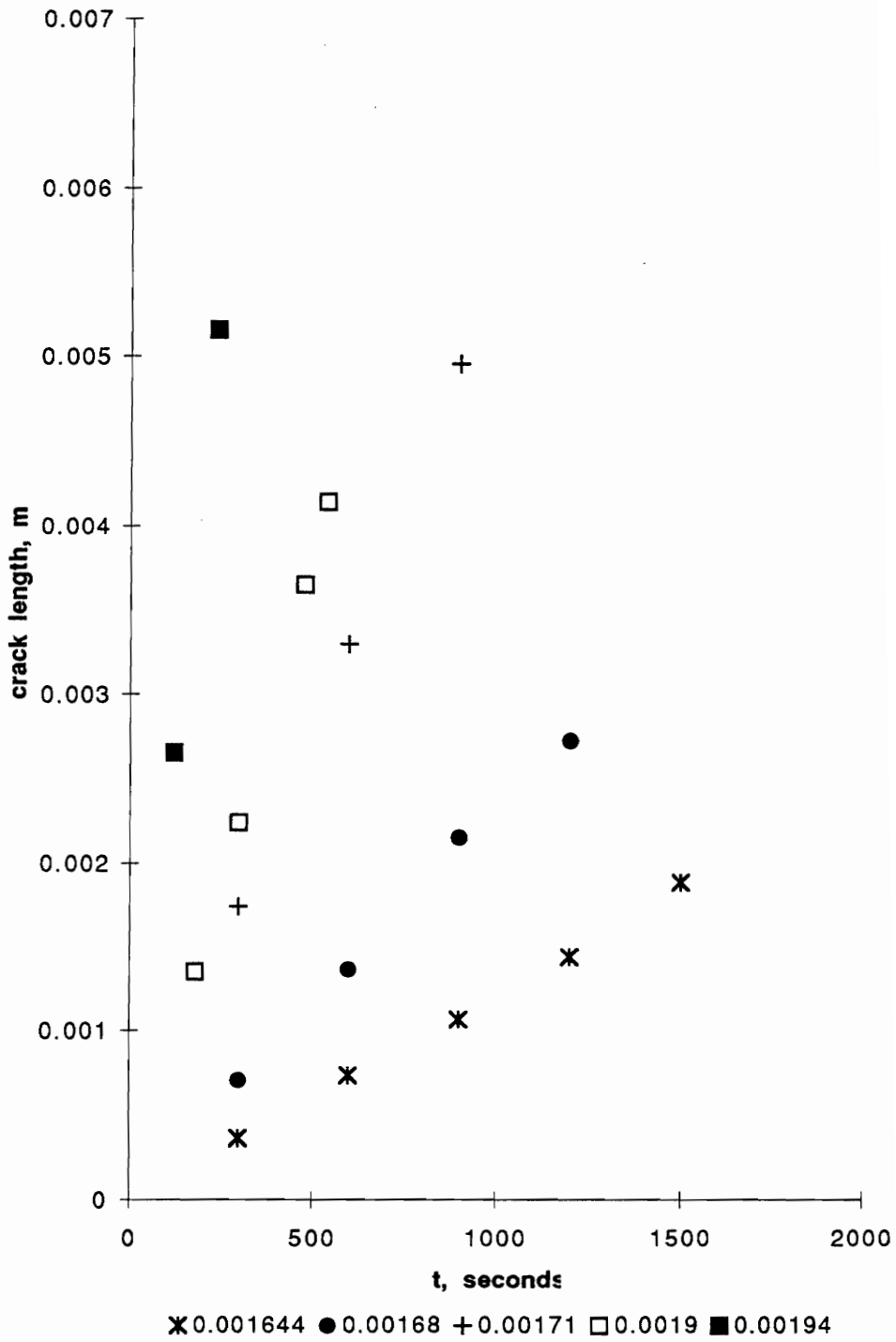


Figure 8.3. Crack length vs. time for sealant 249-3 in an aluminum butt joint.

Table 8.1 Summary of crack growth data for the pure shear butt joint tested at 49% relative humidity and 50 °C.

Logarithm		Logarithm		Logarithm	
Displacement	crack speed	Displacement	crack speed	Displacement	crack speed
mm	m/s	mm	m/s	mm	m/s
1.16	-6.64	1.40	-6.31	1.31	-6.22
Time, s	Crack Lenth,mm	Time, s	Crack Lenth,mm	Time, s	Crack Lenth,mm
10800	2.56	3600	1.92	3600	2.37
18000	4.13	7200	3.57	5400	3.47
25200	5.94	10800	5.54	7200	4.53
54000	12.57	14400	7.66	9000	5.93

Logarithm		Logarithm		Logarithm	
Displacement	crack speed	Displacement	crack speed	Displacement	crack speed
mm	m/s	mm	m/s	mm	m/s
1.40	-6.10	1.64	-5.94	1.68	-5.66
Time, s	Crack Lenth,mm	Time, s	Crack Lenth,mm	Time, s	Crack Lenth,mm
300	0.25	300	0.36	300	0.70
600	0.49	600	0.73	600	1.36
900	0.76	900	1.06	900	2.15
1200	0.98	1200	1.44	1200	2.72
		1500	1.88		

Logarithm		Logarithm		Logarithm	
Displacement	crack speed	Displacement	crack speed	Displacement	crack speed
mm	m/s	mm	m/s	mm	m/s
1.71	-5.27	1.90	-5.14	1.94	-4.69
Time, s	Crack Lenth,mm	Time, s	Crack Lenth,mm	Time, s	Crack Lenth,mm
300	1.74	180	1.35	120	2.65
600	3.30	300	2.24	240	5.16
900	4.95	480	3.65	360	7.78
		540	4.14		

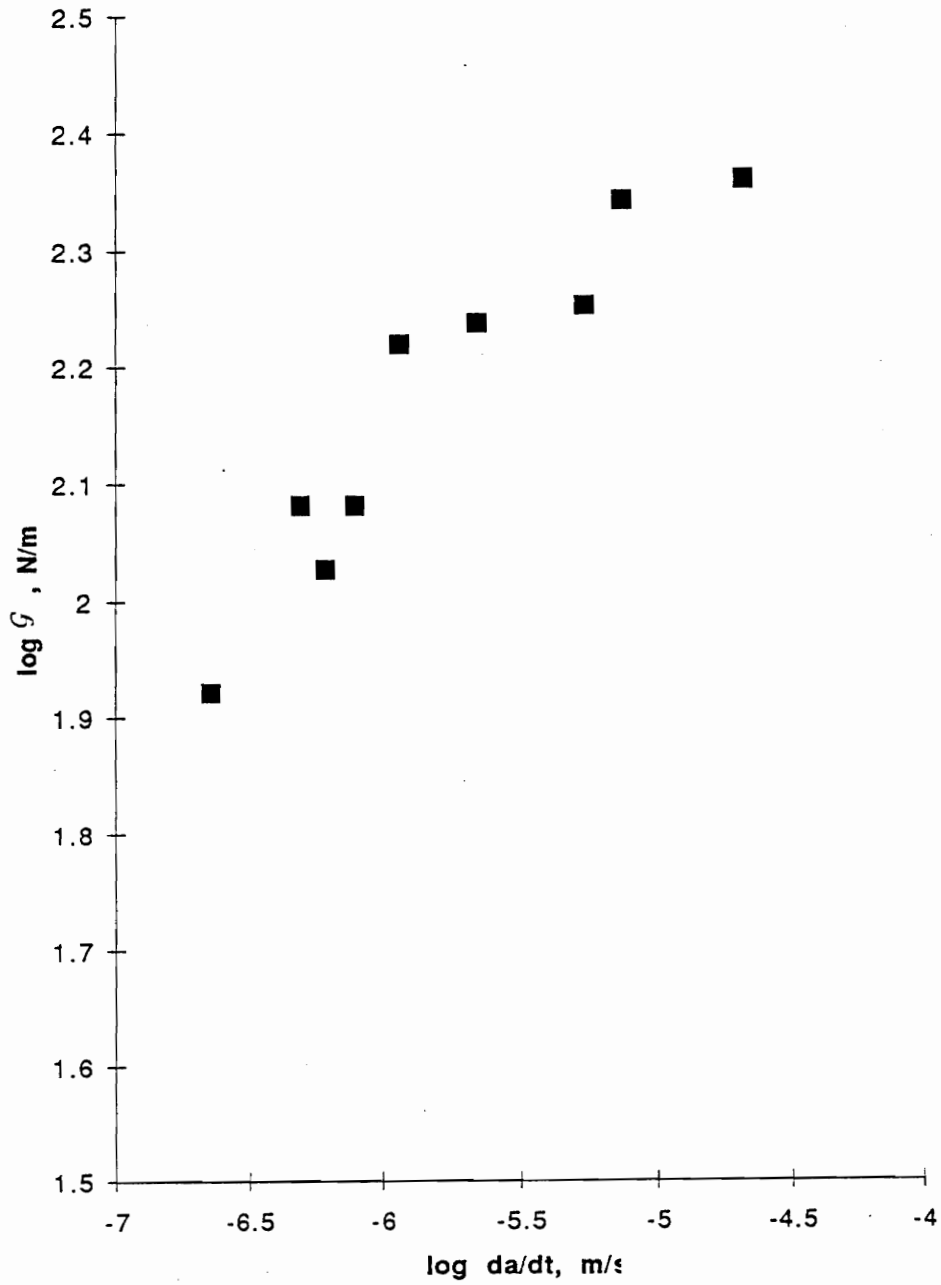


Figure 8.4 Logarithm of strain energy release rate, G , vs. logarithm of crack speed for aluminum butt joint.

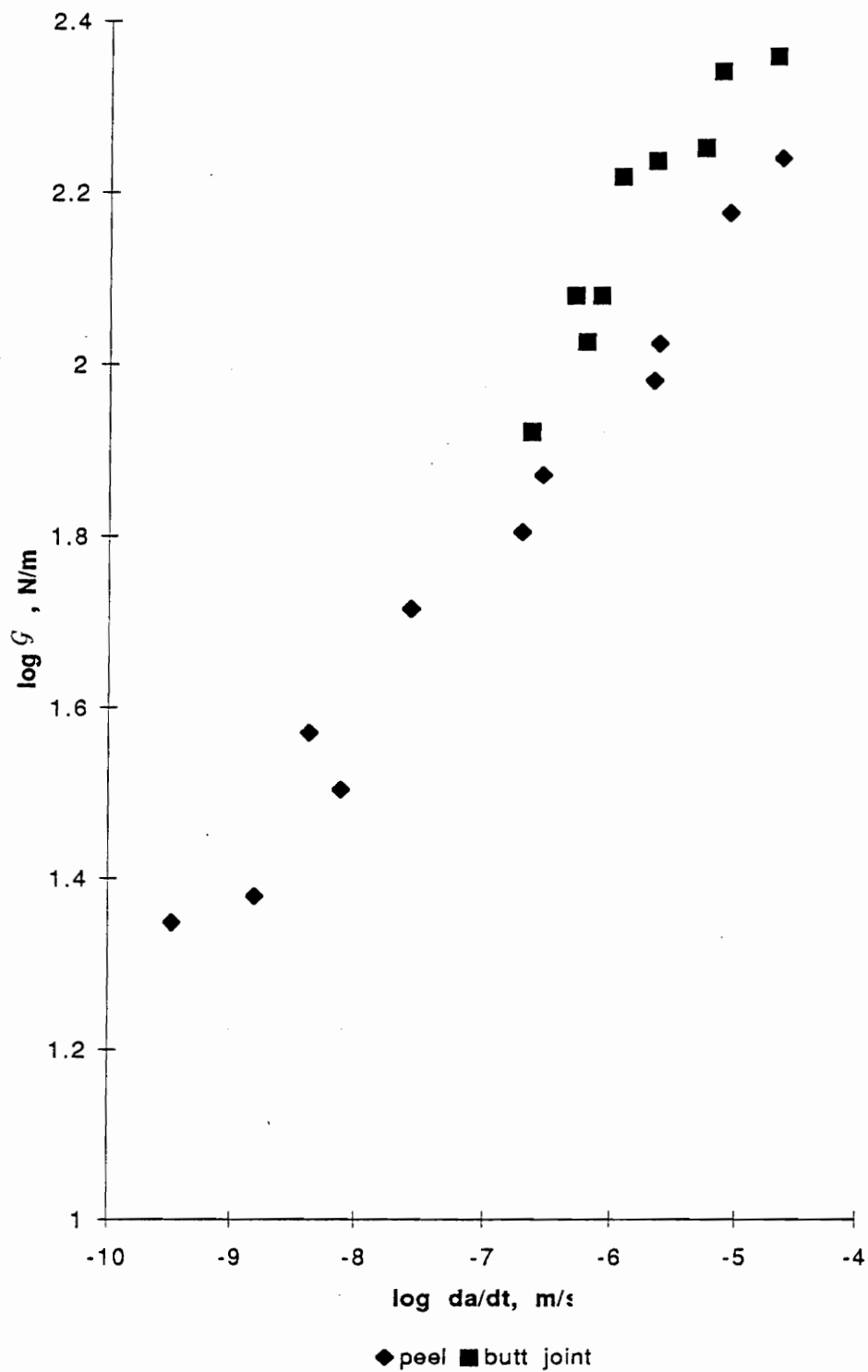


Figure 8.5 Comparison of fracture data for silicone aluminum butt joint and silicone aluminum 45° peel test.

The difference between the two tests may be caused by differences in the stress field at the crack tip. The peel test was conducted at an angle of 45° resulting in a mix of mode I and mode II as described in section 3.5.2. The butt joint was conducted in uniaxial tension on a wide yet thin sealant sample. As described in section 3.3.2.2, this is considered a state of pure shear or mode II. However, Gent *et al.* have studied the fracture energy of rubber using several mode mixes and concluded that the mode mix of the far field stress is not significant.¹ Instead, it was postulated that the state of stress at the crack tip for elastomers is always mode I.

More likely, the difference between the two test methods may be caused by edge effects near the crack tip. For the peel test, the crack tip is very clean and wide, 19.1 mm. Edge effects are minimized. Conversely, the butt joint has a relatively narrow crack at 1.7 mm. A small fillet occurs at the edge of the sealant and the aluminum substrate on both sides of the running crack. This fillet has a 0.1 mm radius of curvature. Therefore, it contributes to the surface area of the crack and lowers the stress intensity, leading to lower crack speeds for the same energy release rate relative to the peel test.

Alternatively, the deviation between the two test methods may be due to experimental error. However, it is difficult to estimate the confidence limits for such a small sample of data.

8.4 Summary

The equilibrium stress vs. displacement for a glass-silicone-glass butt joint pulled in uniaxial tension was measured and the temperature dependence determined. The resulting data was used to calculate the strain energy release rate as a function of temperature and displacement for an aluminum-silicone-aluminum butt joint.

The crack growth rate was measured for the aluminum-silicone-aluminum butt joint under constant uniaxial displacement, temperature and relative humidity. The crack growth

rate was constant for each set of conditions. The logarithm the strain energy release rate was plotted against the logarithm of the crack growth rate yielding a linear response.

The aluminum butt joint data was compared to the 45° peel test data from Chapter VII. Reasonably good correlation was obtained. However, the butt joint data indicated slower crack growth than that indicated by the peel test. The deviation may be caused by reduction of the stress intensity at the crack tip of the butt joint caused by edge effects,

8.5 References

¹ A. N. Gent and A. J. Kinloch, *Journal of Polymer Science: Part A*, **9**, 659 (1971).

IX. Results and Discussion:

Crack Growth Predictions Based on Master Curves and Climate Data

In Chapter VII, the crack speed was related to the strain energy release rate, the relative humidity and the temperature during the test by equation 7.3. In Chapter VIII, the crack speed for a butt joint in tension was related to the temperature of the joint and the displacement of the joint. Data for the butt joint was in reasonably good agreement with data from the peel test. With this data and some judiciously applied assumptions, the crack length will be calculated for a butt joint after one year exposure at two different climates. The daily weather conditions for a desert climate, Wittman Arizona, and a hot humid climate, Miami Florida, obtained for the year 1994 will be used to simulate the two different climates.

9.1 Simulated Joint Conditions

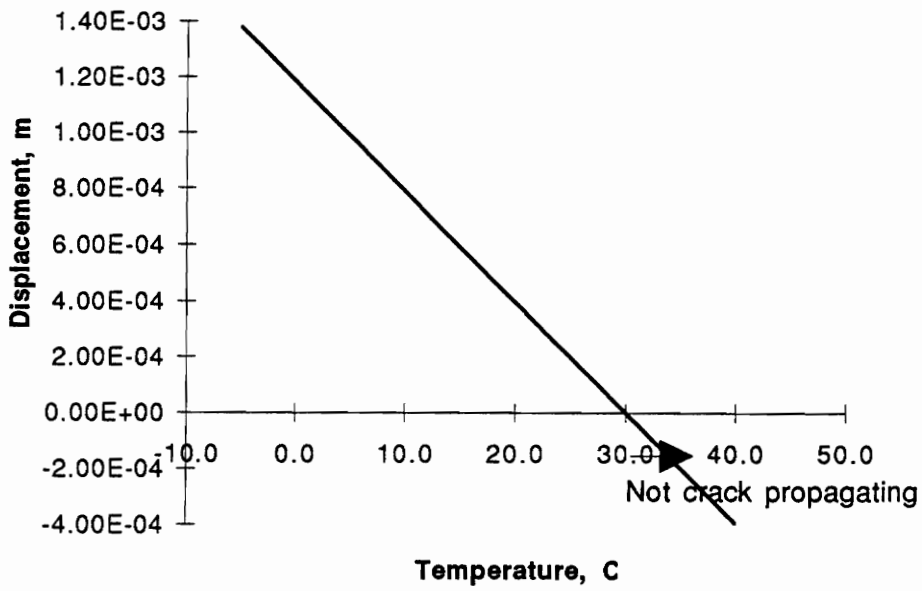
A 2 m long by 12.7 mm wide by 1.6 mm thick sealant joint to aluminum was assumed. The joint was vertical on an exterior wall sheltered from direct sun light or rain. On each side of the joint, the aluminum panel was 1.7 m wide.

The aforementioned joint conditions were chosen to minimize the affects of standing water, ultraviolet radiation and acid rain. Although standing water, ultra violet radiation and acid rain all play an important role in most joint applications, as well as many other conditions, only relative humidity and temperature were included in the relationships from the previous two chapters.

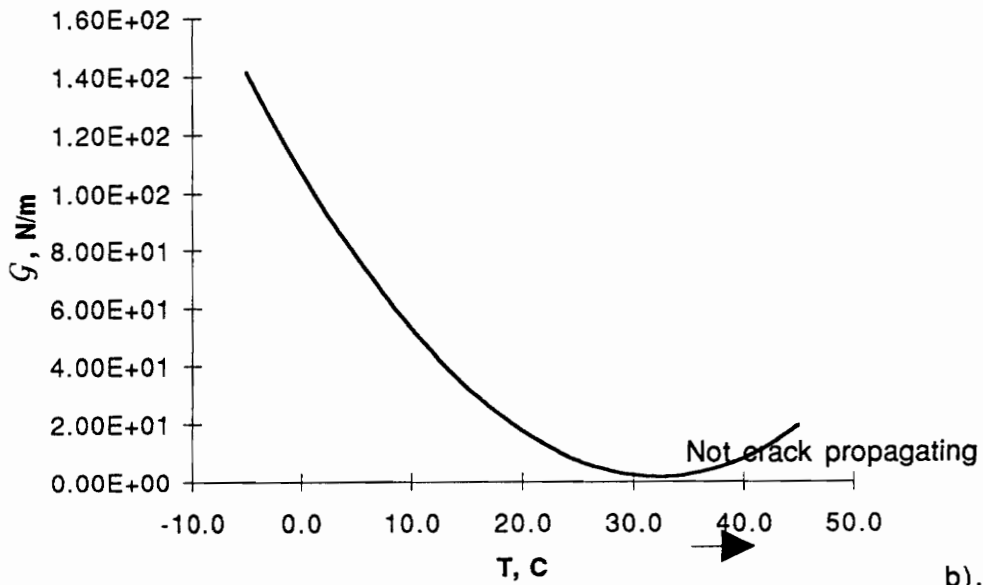
The thermally induced joint movement was calculated for the previously defined joint dimensions by the following equation:

$$x = 1.7\alpha\Delta T \quad (9.1)$$

where the coefficient of thermal expansion, α , is 23.2×10^{-6} for the aluminum. A plot of the joint movement vs. temperature for the simulated joint is shown in Figure 9.1a. The



a).



b).

Figure 9.1. a) Joint movement for 12.7 mm joint with reference temperature 30 °C. b) strain energy release rate for the same joint with silicone sealant 249-3.

sealant cure temperature was 30° C. From this movement data, the strain energy release rate, G , was calculated using equations 8.2- 8.4 from Chapter VIII. The strain energy release rate vs. temperature can be seen in Figure 9.1b. Strain energy calculations for the joint when in compression are not valid. The 1.7 mm thin sealant does not support compressive loads because it can bend when it is compressed. Therefore, no crack growth occurred for the compressive displacements. The sensitivity of the strain energy release rate to low temperatures is easily observed in Figure 9.1b and will play an important role in the crack growth rate calculations.

9.2 Crack Growth Calculations

The crack growth vs. time was calculated by combining equations 7.3, 8.2- 8.4 to obtain the crack speed as a function of temperature and relative humidity. The equations are summarized below:

$$\dot{a} = \left(\frac{G}{k}\right)^{1/n} \frac{1}{a_T a_{rh}} \quad (7.3)$$

$$G = \int_{x_0}^x (mx+b)dx \quad (8.2)$$

$$m = 236040T + 1.07 \times 10^8 \quad (8.3)$$

$$b = -437T + 24827 \quad (8.4)$$

$$a_T = 10^{-20.81+6841T} \quad (\text{Figure 7.8})$$

$$a_{rh} = 10^{9.253-0.266rh+0.0016rh^2} \quad (\text{Figure 7.7})$$

$$x = 1.7\alpha\Delta T \quad (9.1)$$

$$k = 1161.7 \quad (\text{Table 7.5})$$

$$n = 0.184 \quad (\text{Table 7.5})$$

Fatigue was not included in the above equations. For this model, the strain rate was very slow with a strain cycle occurring only once per day. For a joint which experiences vibrations or intermittent wind load, fatigue effects could be significant.

The temperature, T , and the relative humidity, rh , were obtained from the climate data. The climate data contained the daily high and low temperature and relative humidity. Since the crack speed has a nonlinear dependence on temperature and relative humidity, the average daily values could not be used. Instead, the daily highs and lows were used to construct functions for temperature and relative humidity. The function for daily temperature was assumed to be saw tooth shaped with the daily high temperature at 2 PM and the daily low temperature at 4 am. The function for relative humidity was also assumed to be saw tooth shaped but with the high humidity occurring at 4 AM and the low occurring at 2 PM. The crack growth for each day was calculated by applying the temperature and relative humidity functions to the above equations calculated at one hour intervals.

9.2.1 Miami, Florida, 1994

The daily climate data for Miami Florida for the year 1994 was obtained from the South Florida Test Service.¹ Figure 9.2 and 9.3 contain the daily climate data for temperature and relative humidity respectively. A cure temperature of 30 °C was assumed for this study. The average daily change in temperature was 9.6 °C. The annual change in average daily temperature was 16 °C. The average relative humidity was 80% with the daily high above 90% for nearly all the year. The daily low relative humidity fell below 35 only once during the entire year. In Chapter VII, it was shown that the failure mode for the silicone aluminum bond changes from near the interphase to cohesive in the sealant when the relative humidity is less than 35%. Since the strain energy release rate is always

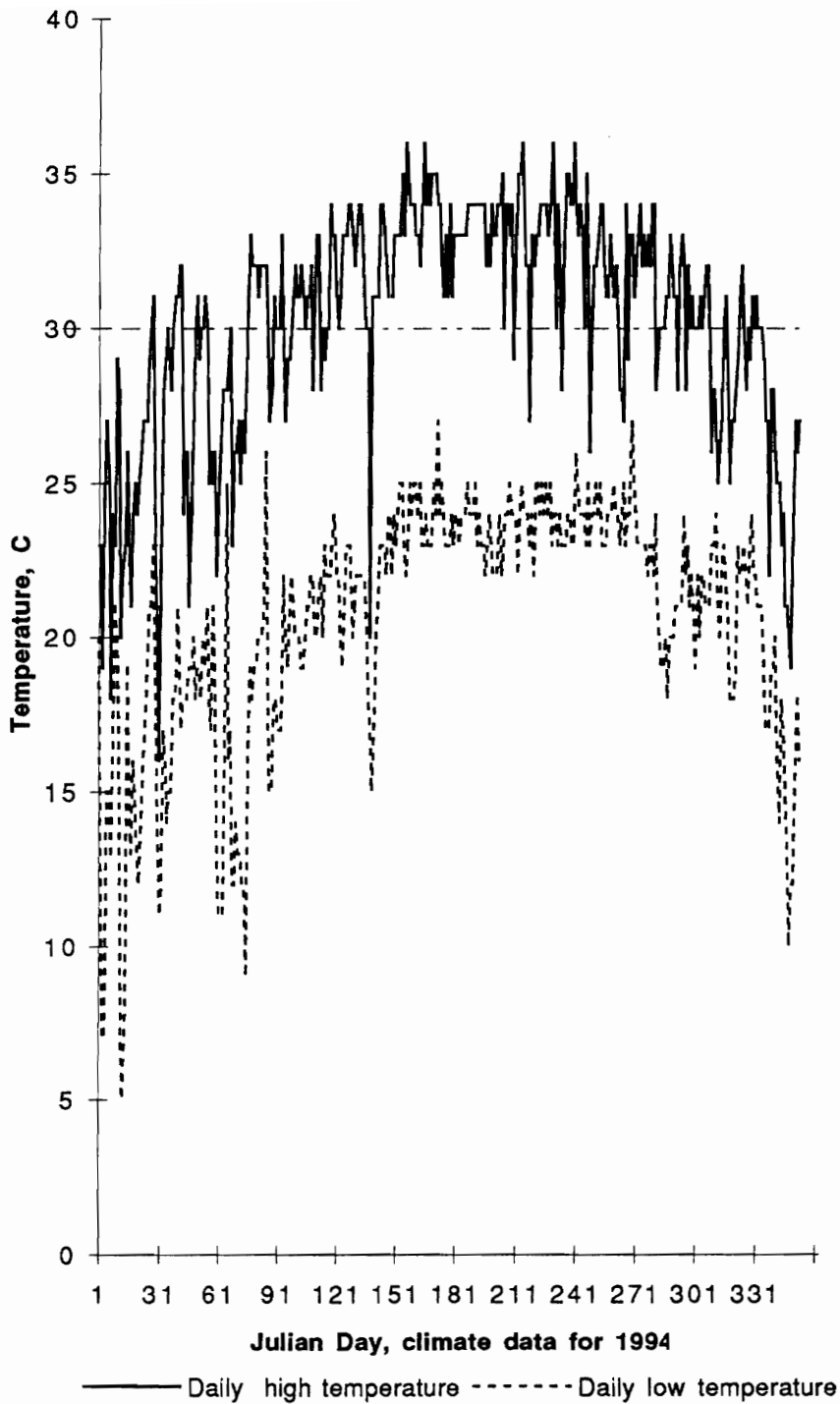


Figure 9.2 Daily high and low temperature for Miami Florida during 1994. Dashed horizontal line is sealant application temperature.

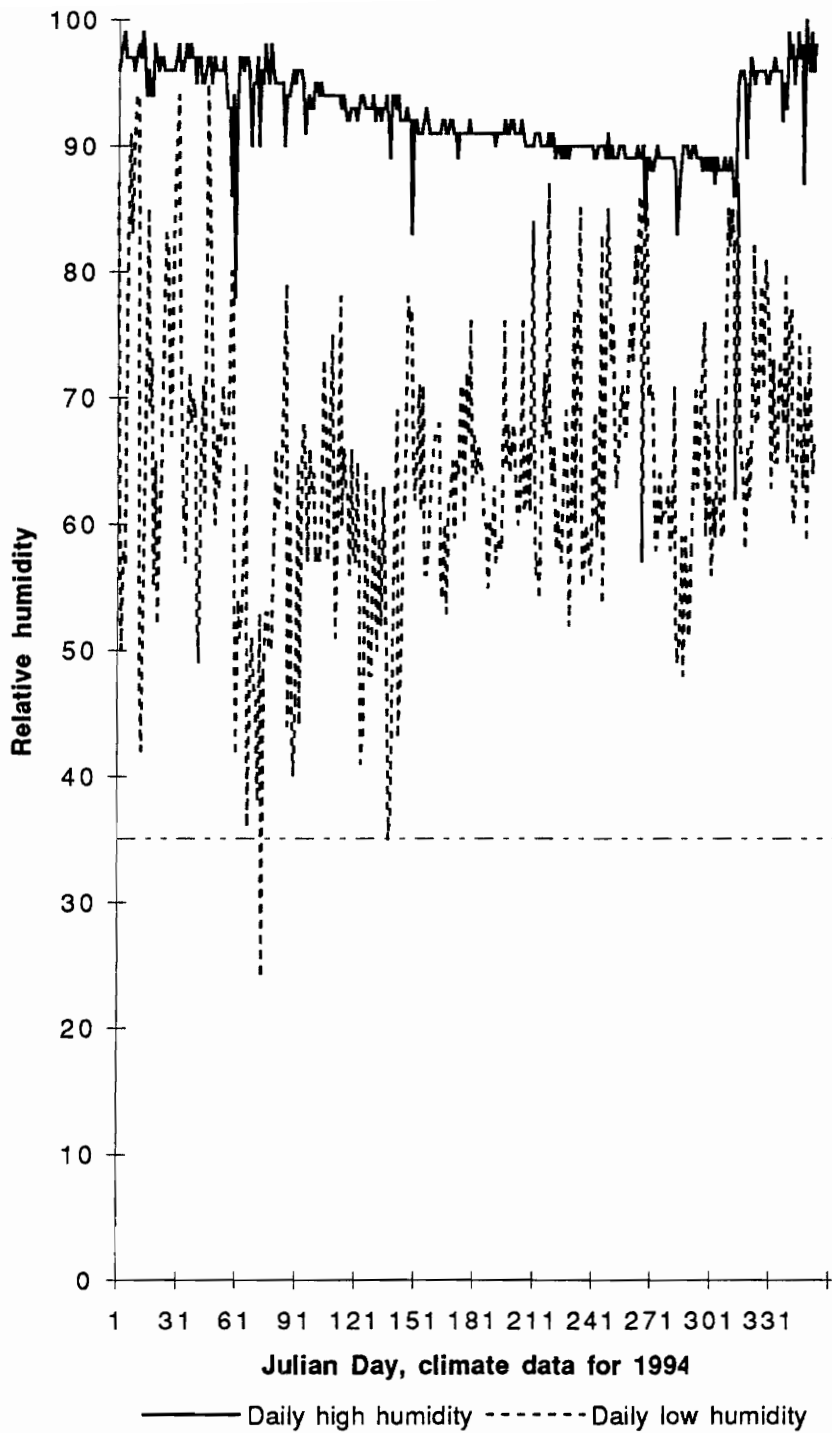


Figure 9.3 Daily high and low relative humidity for Miami Florida during 1994. Dashed horizontal line is point where failure mode changes from interphase to cohesive in sealant.

less than the threshold fracture energy for the sealant, at least 200 N/m from Chapter VI, the crack arrests whenever the relative humidity is less than 35%. This trend was very important for the Arizona data presented in the next section.

Figure 9.4 contains a plot of the crack length over the course of the year. The annual crack growth was 0.0007 meters. During the summer months, virtually no crack growth occurs. However, significant crack growth can be detected during the winter months. Nearly all the crack growth occurs during the 135 days of the year when the temperature is significantly less than the sealant application temperature of 30 °C. The temperature dependency of equation 8.2 accounts for the trends observed for this climate.

9.2.2 Wittman, Arizona, 1994

The climate data for Wittman, Arizona is contained in Figures 9.5 and 9.6. This desert climate undergoes much larger changes in temperature and relative humidity compared to the Miami climate. The average daily change in temperature was 15 °C. The annual change in average daily temperature was 35 °C. The average relative humidity was less than 35%. During these conditions, the crack did not grow as discussed in the previous section. However, the relative humidity rises well above 35% whenever rainfall occurs.

Figure 9.7 contains the plot of crack length over the course of the year for both climate. The annual growth for Wittman was 0.0037 meters, nearly five times the annual crack growth in Miami. Again during the summer months, the crack growth was negligible. Nearly all the crack growth occurred when the temperature was well below 30 °C and when the relative humidity was above 35%. Essentially, all the crack growth occurred on rainy days during the winter months.

The basic shapes of the curves in Fig. 9.7 are the same for both climates.

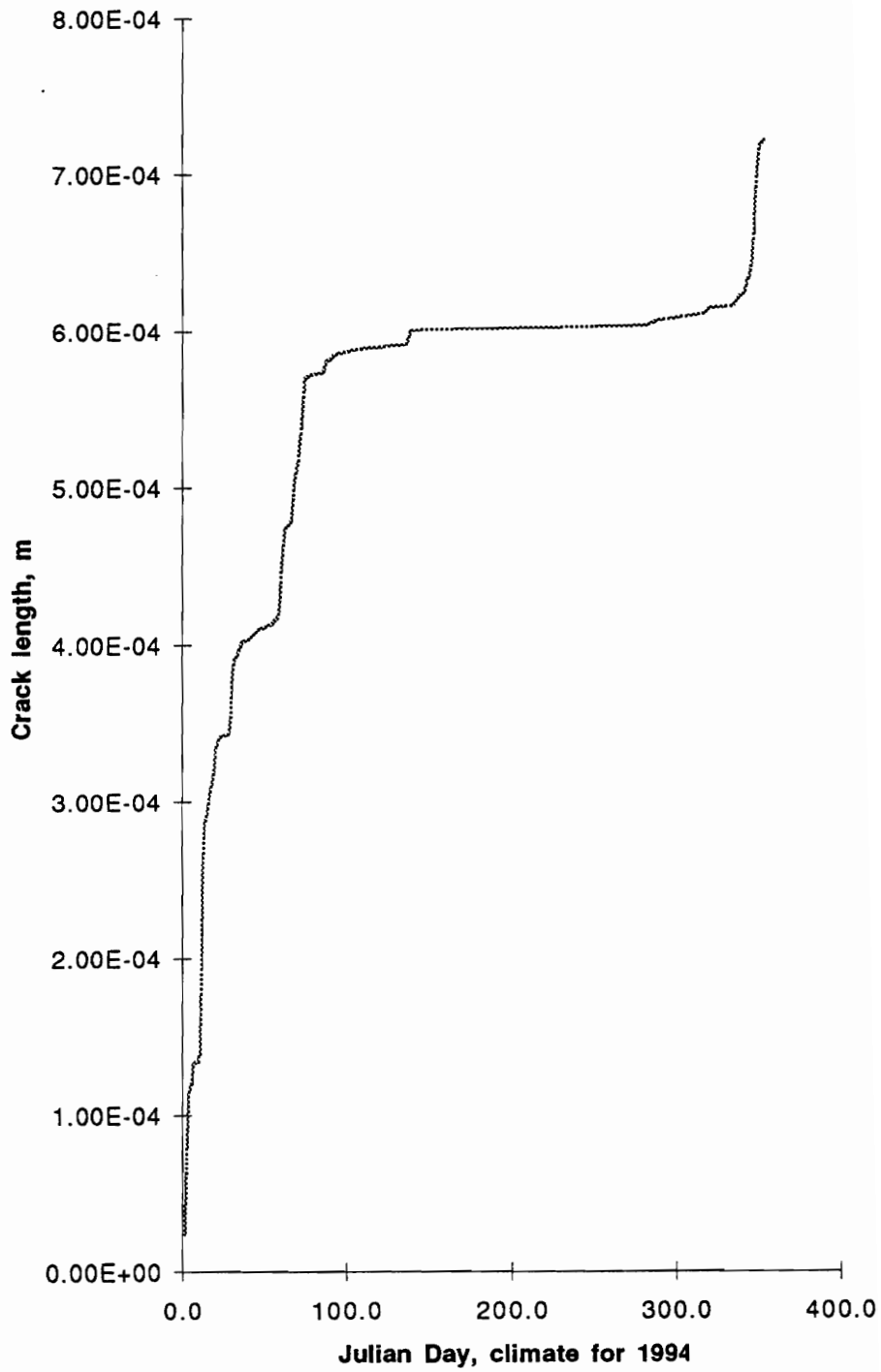


Figure 9.4 Daily crack growth in an aluminum joint for Miami climate.

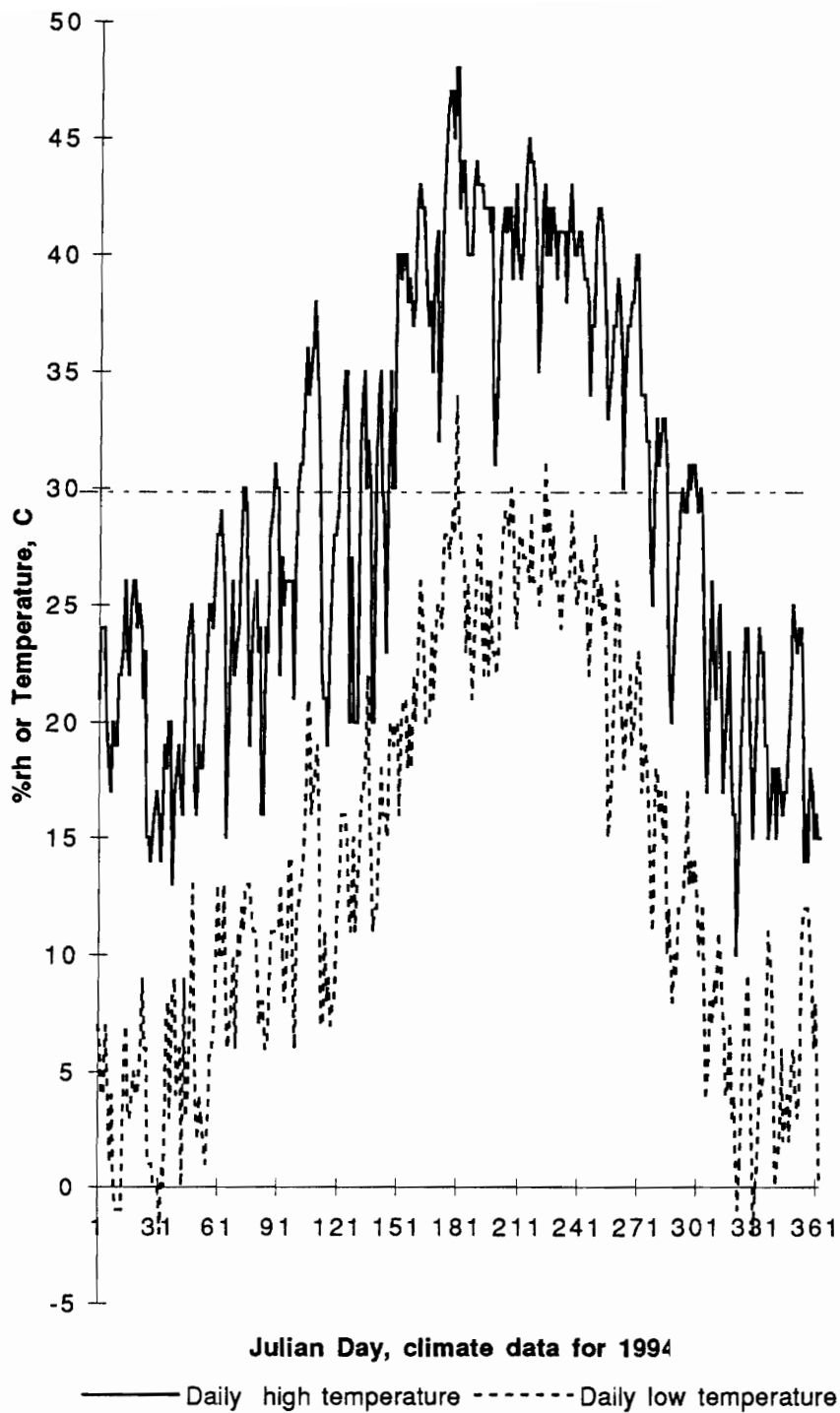


Figure 9.5 Daily high and low temperature for Wittman Arizona during 1994. Dashed horizontal line is sealant application temperature.

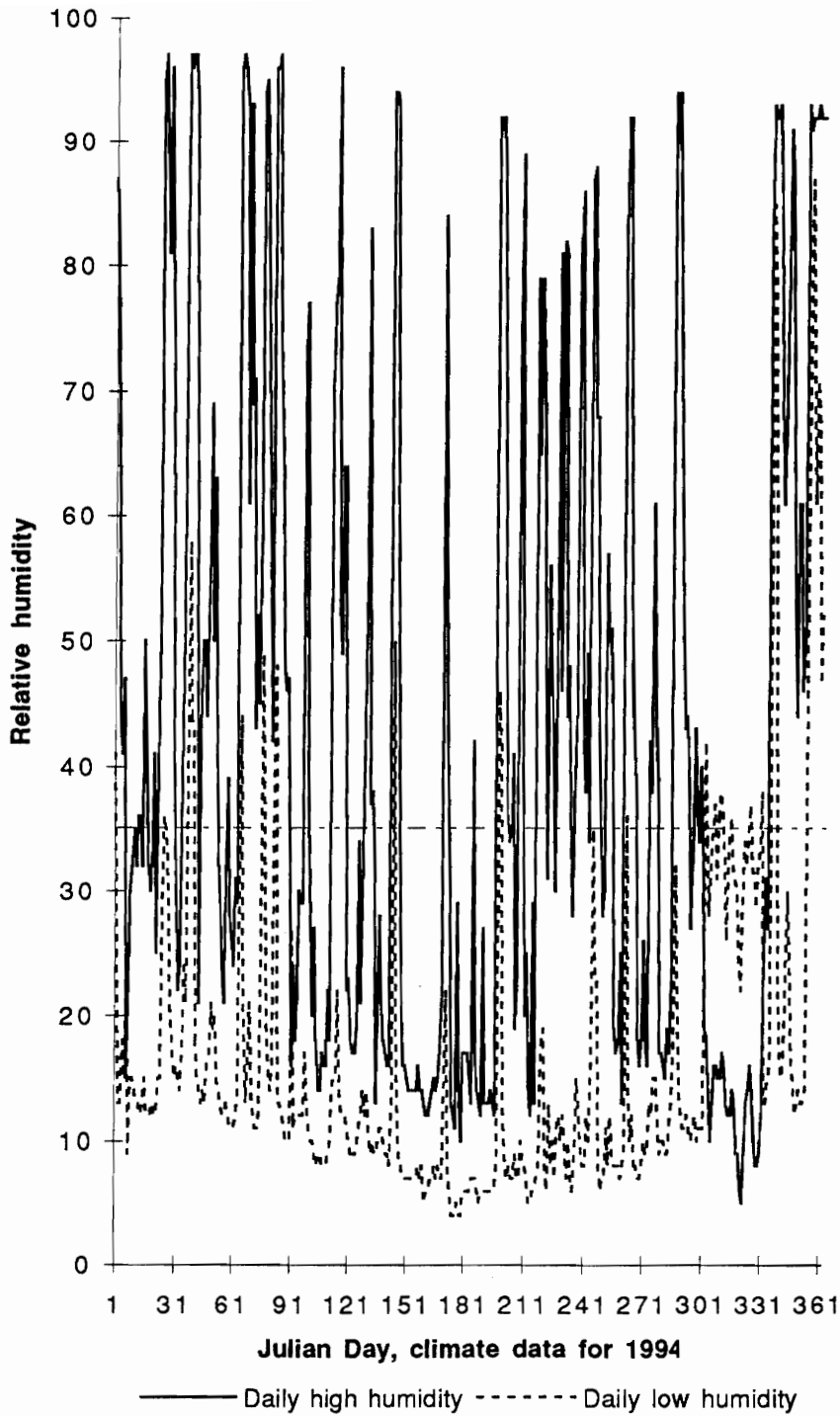


Figure 9.6 Daily high and low relative humidity for Wittman Arizona during 1994. Dashed horizontal line is point where failure mode changes from interphase to cohesive in sealant.

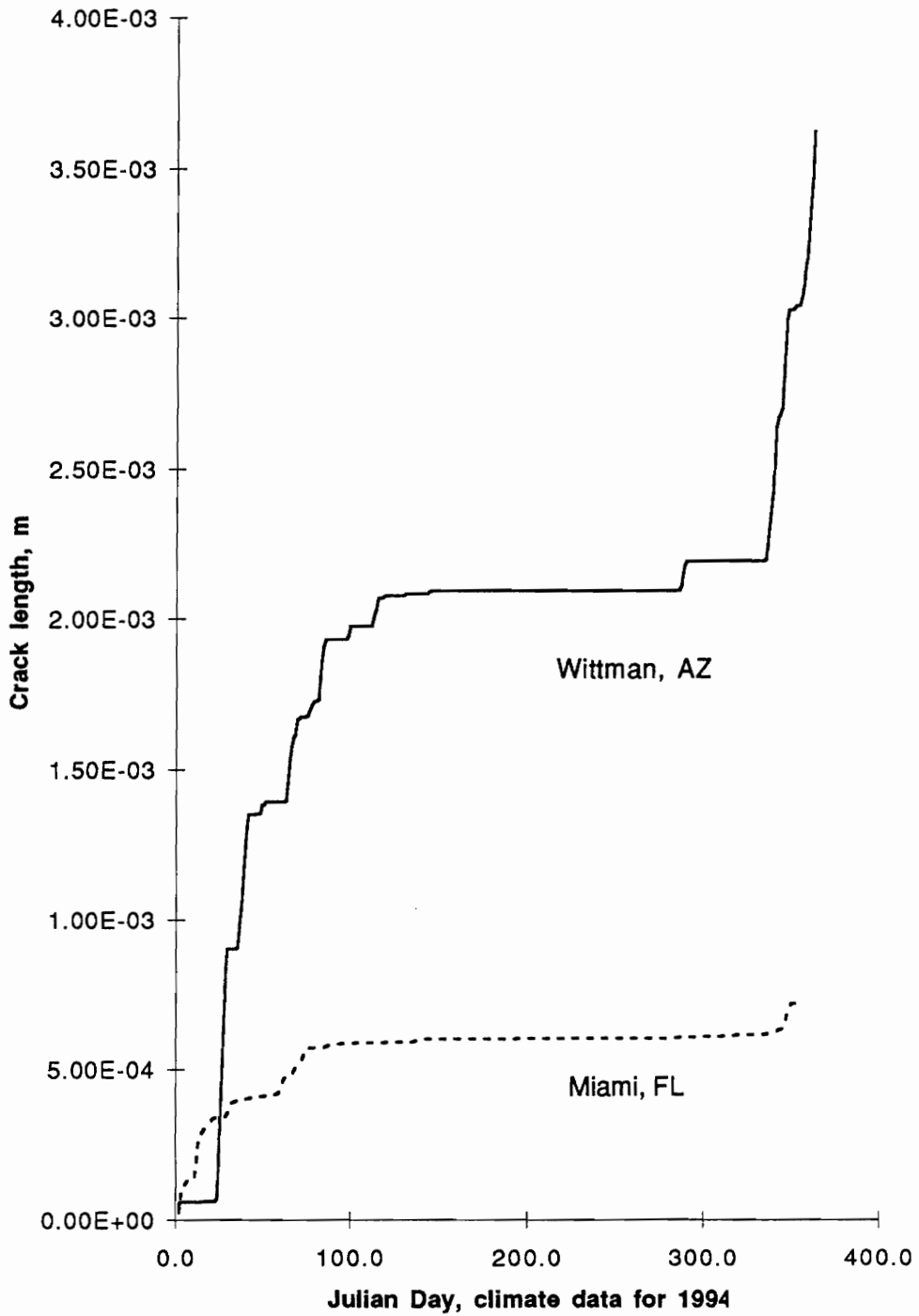


Figure 9.7 Daily crack growth in an aluminum joint for two different climates.

However, the Arizona curve is less smooth. The crack growth only occurs intermittently when both the temperature and relative humidity are favorable. The temperature was frequently low enough to promote crack growth. However, the relative humidity was usually too low for crack growth except during intermittent rain storms. In spite of this, the Arizona climate was clearly more damaging to the joint than the Miami climate as indicated by an annual crack growth 5 times larger than the Miami climate.

9.3 Summary

The annual crack growth was predicted for an aluminum sided butt joint for two different climates.

For the Miami Florida climate, crack growth occurred during the cold months. The annual crack growth was 0.0007 meters. Relative humidity was not a significant factor because the relative humidity was nearly always above 35%. The change in crack speed due to changes in relative humidity between 35% and 100% was not significant compared to the changes in crack speed with respect to the temperature of the joint.

For the Wittman Arizona climate, crack growth also occurred mainly during the winter months. The annual crack growth was 0.0037 meters which is greater than 5 times the annual growth for the Miami climate. The wide variations in annual temperature account for the significant increase in crack growth. However, the average relative humidity was less than 35% most of the time. During periods when the relative humidity was less than 35%, the crack growth was arrested. The relative humidity was only greater than 35% during and immediately after rain storms. Therefore, crack growth only occurred on rainy days during the winter months.

The speed of the crack greatly increases when the temperature drops below the sealant application temperature and the relative humidity stays above 35%. Therefore, climates which have wide annual changes in temperature and maintain moderate levels of humidity during the cold months will have the largest crack growth.

9.4 References

¹ The weather data was graciously supplied by Leslie Crewdson at South Florida Test Service, 17301 Okeechobee Rd, Miami, Florida, 33015.

X Overall Summary

As stated in the introduction, the objective of this work was to conduct experiments which would test the validity of the following thesis statement:

Sealant material properties measured as a function of rate, temperature and relative humidity for a specific sealant and substrate can be used to predict the long term performance of sealant joints independent of the joint geometry so long as the same materials are used to construct the joint.

One goal of this work was to predict the annual crack growth of an expansion joint composed of a silicone sealant and a polished aluminum substrate. Since the strain rate of an expansion joint is relatively slow, the material properties in question needed to be studied at very slow strain rates. Therefore, the modulus of the sealant was measured under quasi-equilibrium conditions. Next, a 45° peel test was used to obtain fracture energy vs. crack growth data over a wide range of temperature, relative humidity and crack speed. A doubly shifted master curve was constructed with the above variables. From this curve, the relationship between crack speed, fracture energy, temperature and relative humidity was obtained.

$$\dot{a} = \left(\frac{G}{k}\right)^{1/n} \frac{1}{a_T a_{rh}} \quad (7.3)$$

$$a_T = 10^{-20.81+6841T} \quad (\text{Figure 7.8})$$

$$a_{rh} = 10^{9.253-0.266rh+0.0016rh^2} \quad (\text{Figure 7.7})$$

$$k = 1161.7 \quad (\text{Table 7.5})$$

$$n = 0.184 \quad (\text{Table 7.5})$$

Equation 7.3 is valid for $278.2 \text{ }^\circ\text{K} < T < 363.2 \text{ }^\circ\text{K}$ and $37\% < rh < 85\%$, $0 \text{ N/m} < G < 600 \text{ N/m}$.

The fracture energy vs. crack speed data for the 45° peel specimens was compared to the fracture energy vs. crack speed data obtained for a butt joint, after the necessary calculations accounting for the material properties of the sealant were applied to the data. The fracture energy for the butt joint was slightly higher but was reasonably close to the fracture energy measured by the 45° peel test., Thus confirming one half of the thesis statement. Namely that material properties from one test configuration can be re-cast to describe the crack growth for a different test configuration.

Unfortunately, the rest of the thesis statement, the predictive portion, is much harder to test. As a first attempt, equation 7.3 was applied to a simulated expansion joint constructed from the same materials as previously mentioned. Crack growth data was calculated for the weather conditions in Miami, Florida and Wittman, Arizona using the climate data obtained for the year 1994. For both climates, the nearly all the crack growth occurred during the winter months. The predicted annual crack growth data for Miami was 0.7 mm and the predicted annual crack growth for Wittman was 3.7 mm. The Wittman crack growth was five times faster than the Miami crack growth because of the colder temperatures occurring during the winter months. To confirm this prediction, sealant joints have been prepared and will be aged at the two sites.

While testing the above thesis statement, several unique observations have been documented and are described in the paragraphs below.

The failure mode for a silicone sealant on aluminum changes from near the aluminum oxide layer to cohesive in the sealant when the relative humidity is less than 35%. This phenomenon is independent of the test temperature. For the failure near the

aluminum oxide, a doubly shifted master curve has been constructed for the PDMS aluminum joint using temperature and relative humidity as the shifting variables. The shift factor plots formed smooth monotonic functions indicating no change in mechanism for crack advancement. The temperature shift factor was not related to the WLF theory but worked well with an Arrhenius theory. The calculated activation energy for the fracture process was 31.2 kcal/mol.

The effect of peel rate, modulus and sealant bond thickness was quantified for the 180° peel test on glass and aluminum. As expected, the sealant had better adhesion to glass than to aluminum. The failure mode was cohesive in the sealant for all the test conditions on glass except one. The fracture energy vs. peel rate was fit to a power law function. The effect of sealant bond thickness was accounted for by replacing the peel rate with the strain rate. The high modulus sealant had a higher fracture energy than the low modulus sealant when the strain rate was low. When the strain rate was high, the low modulus sealant had the highest fracture energy. This same rate dependence was observed for the stress strain data. The viscoelastic nature of the sealant is the cause for the reversal of the trends as a function of rate. This is an excellent example of the need to study the rate effect on material properties. In addition, the dependence of the failure mode on rate, bond thickness and sealant modulus was determined for the aluminum substrate. Cohesive failure occurs more frequently when the sealant modulus is decreased, the peeling rate is increased, or the peeling thickness is increased.

The 45° peel test was used to investigate the fracture energy of a high and a low modulus sealant, on glass or aluminum, under wet or dry conditions and over several decades of rate. The rate dependence was fit to a power law model. Both the high modulus sealant and the low modulus sealant failed cohesively when peeled from dry glass. When pulled from glass under wet conditions at speeds less than 10^{-7} m/s, both

sealants failed near the interphase. At rates above 10^{-7} m/s, both sealants failed cohesively. The high modulus sealant failed near the interphase for all test conditions on aluminum. The low modulus sealant failed cohesively on aluminum except when peeled at rates less than 10^{-7} m/s under wet conditions. ESCA analysis of the fracture surfaces when the failure was near the interphase detected silicone. A layer of silicone less than 4 nm thick was detected by ESCA analysis. This silicone could not be removed by washing in hexane.

ESCA and AFM have been combined to identify the topography and elemental composition of the fracture surface of silicone sealant on stainless steel. The interfacial failure surface for PDMS on stainless steel is within 10 nm of the surface. When the fracture occurs in this interphase, the fracture energy is proportional to the amount of PDMS left on the surface. The size of the plastic zone is nearly equivalent to the distance between two cross links. Carbonaceous contamination is not displaced by the sealant from the stainless steel substrate. Contamination inhibits primary bonding (ionic or covalent) and results in a lower fracture energy. Roughness increases the fracture energy; and this effect is more pronounced when the surfaces are cleaner. Water lowers the fracture energy especially for the dirtier surfaces. Roughness reduces the effect of the water damage but doesn't eliminate it.

VITA

Nick E. Shephard was born in Bay City, Michigan on February 26, 1965, the son of Norman and Janet Shephard. He graduated from Akron-Fairgrove High School in Akron, Michigan in June 1983. During 1984, he was awarded a Residential Life Scholarship at the Saginaw Valley State University. In December 1987, he obtained a Bachelor of Science degree in Chemistry from Saginaw Valley State University in Saginaw, Michigan. As an undergraduate, he wrote software to control the output of an electron spin resonance instrument under the direction of Dr. G. Eastland.

While obtaining his undergraduate degree, he was employed at Dow Corning Corporation in Midland, Michigan where he evaluated experimental sealant formulations. In January of 1987, he moved to Elizabethtown, Kentucky, where he worked on sealant pilot plant production processes for the Dow Corning Corporation. For his efforts, he received a Manufacturing Achievement Award. In January of 1988, he moved back to Midland, Michigan to continue product development of silicone sealants, developing two new products and generating several patents. He joined the research group of Dr. J. P. Wightman in January 1992 after receiving a research fellowship from the Dow Corning Corporation.

The author has participated in the Center for Adhesive and Sealant Science and the Adhesive and Sealants Council. He is a member of the Adhesion Society, the American Chemical Society and Sigma Xi. Before returning to an industrial occupation, Nick has chosen a six month Post Doctoral position at Virginia Polytechnic Institute and State University.

A handwritten signature in black ink that reads "Nick E. Shephard". The signature is written in a cursive, flowing style.